

DESIGN AND ANALYSIS OF A  
HYBRID TRAILING EDGE CONTROL SURFACE OF A  
FULLY MORPHING UNMANNED AERIAL VEHICLE WING

A THESIS SUBMITTED TO  
THE GRADUATE SCHOOL OF NATURAL AND APPLIED SCIENCES  
OF  
MIDDLE EAST TECHNICAL UNIVERSITY

BY

İLHAN OZAN TUNÇÖZ

IN PARTIAL FULFILLMENT OF THE REQUIREMENTS  
FOR  
THE DEGREE OF MASTER OF SCIENCE  
IN  
AEROSPACE ENGINEERING

FEBRUARY 2015



Approval of the thesis:

**DESIGN AND ANALYSIS OF A  
HYBRID TRAILING EDGE CONTROL SURFACE OF A  
FULLY MORPHING UNMANNED AERIAL VEHICLE WING**

submitted by **İLHAN OZAN TUNÇÖZ** in partial fulfillment of the requirements for  
the degree of **Master of Science in Aerospace Engineering Department, Middle  
East Technical University** by,

Prof. Dr. Gülbin Dural Ünver

Director, Graduate School of **Natural and Applied Sciences**

Prof. Dr. Ozan Tekinalp

Head of Department, **Aerospace Engineering**

Prof. Dr. Yavuz Yaman

Supervisor, **Aerospace Engineering Dept., METU**

**Examining Committee Members:**

Prof. Dr. Serkan Özgen

Aerospace Engineering Dept., METU

Prof. Dr. Yavuz Yaman

Aerospace Engineering Dept., METU

Assoc. Prof. Dr. Ender Cigeroğlu

Mechanical Engineering Dept., METU

Assoc. Prof. Dr. Melin Şahin

Aerospace Engineering Dept., METU

Assist. Prof. Dr. Ercan Gürses

Aerospace Engineering Dept., METU

**Date:** 06.02.2015

**I hereby declare that all the information in this document has been obtained and presented in accordance with academic rules and ethical conduct. I also declare that, as required by these rules and conduct, I have fully cited and referenced all material and results that are not original to this work.**

Name, Last Name:

Signature:

## **ABSTRACT**

### **DESIGN AND ANALYSIS OF A HYBRID TRAILING EDGE CONTROL SURFACE OF A FULLY MORPHING UNMANNED AERIAL VEHICLE WING**

Tunçöz, İlhan Ozan

M.S., Department of Aerospace Engineering

Supervisor : Prof. Dr. Yavuz Yaman

February 2015, 151 pages

In this thesis, the design and analysis of a hybrid trailing edge control surface of a fully morphing unmanned aerial vehicle wing having the ability to perform both camber and decamber morphings were conducted.

The design of the control surface was done by CATIA V5-6R2012 package program. Two distinct designs, so-called open cell and closed cell designs were initially analyzed via Finite Element Method by using the commercial software ANSYS Workbench v14.0 in in-vacuo condition. Several trade-off studies including material, geometry and servo actuator feature variations were considered in order to decrease the weight of the control surface while still assuring the structural safety.

The designed control surface was also considered as being under the aerodynamic load obtained from the planned flight mission profile of the unmanned aerial vehicle. During the Computational Fluid Dynamics analyses, Pointwise® V17.2R2 package program was used to generate the aerodynamic mesh, and Stanford University Unstructured (SU2) V3.2.1 open-source software was used as a solver. It

was shown that the designed control surface is capable of performing both camber and decamber morphings both in in-vacuo condition and under the aerodynamic loading.

Keywords: Morphing Control Surfaces, Structural Design and Analysis, Finite Element Method, Aerodynamic Analysis, Computational Fluid Dynamics

## ÖZ

### BÜYÜK ORANDA ŞEKİL DEĞİŞTİREBİLEN BİR İNSANSIZ HAVA ARACI KANADININ HİBRİT FİRAR KENARI KONTROL YÜZEYİNİN TASARIM VE ANALİZİ

Tunçöz, İlhan Ozan

Yüksek Lisans, Havacılık ve Uzay Mühendisliği Bölümü

Tez Yöneticisi : Prof. Dr. Yavuz Yaman

Şubat 2015, 151 sayfa

Bu çalışmada, kanat kamburunu değiştirebilen büyük oranda şekil değiştirebilen bir insansız hava aracı kanadının, hibrit firar kenarı kontrol yüzeyinin, tasarım ve analizi gerçekleştirilmiştir.

Kontrol yüzeyinin tasarımı CATIA V5-6R2012 paket programı ile yapılmıştır. Açık hücre ve kapalı hücre adlı iki farklı tasarım, ticari bir yazılım olan ANSYS Workbench v14.0 ile Sonlu Elemanlar Yöntemi kullanılarak, öncelikle vakum koşullarında yapısal olarak incelenmiştir. Kontrol yüzeyinin ağırlığını azaltmak fakat aynı zamanda yapısal güvenlikten de ödün vermeden, malzeme, geometri ve servo motor değişim özellikleri incelenmiştir.

İnsansız hava aracının planlanan uçuş profile göre aerodinamik yükler hesaplanmış olup, kontrol yüzeyi bu yükler altında da incelenmiştir. Hesaplamalı Akışkanlar Dinamiği analizlerinde aerodinamik çözüm ağı oluşturmak için Pointwise® V17.2R2 paket programı, çözücü içinse Stanford University Unstructured (SU2) V3.2.1 açık kaynak kodlu yazılım kullanılmıştır. Tasarlanan kontrol yüzeyinin hem

vakum durumunda hem de aerodinamik yükler altında kanat kamburunu başarıyla değiştirdiği gösterilmiş.

Anahtar Kelimeler: Şekil Değiştirebilen Kontrol Yüzeyleri, Yapısal Tasarım ve Analiz, Sonlu Elemanlar Yöntemi, Aerodinamik Analiz, Hesaplamalı Akışkanlar Dinamiği



*To three women that I love most:*

*My mother, Sema*

*My sister, Sena Rüya*

*My love, Fatma*

## ACKNOWLEDGEMENTS

I would like to express my greatest gratitude to my supervisor Prof. Dr. Yavuz Yaman, for giving me an opportunity to work with him, allowing me to benefit from his invaluable comments and experiences and his endless patience throughout my study.

I am also indebted to my superiors within the CHANGE project, Assist. Prof. Dr. Ercan Gürses, Assoc. Prof. Dr. Melin Şahin and Prof. Dr. Serkan Özgen for their supports during the studies. I additionally thank to Dr. Gürses for helping me to get scholarship of TÜBİTAK.

I am also grateful to Assist. Prof. Dr. Levent Ünlüsoy for providing me the thesis template.

I must also express my gratitude to my colleagues Pınar Arslan, Uğur Kalkan, Harun Tıraş and Yosheph Yang. Without their help and patience, this study would not finished. Additionally, I must also thank to my co-workers in the laboratory Nima Pedramasl and Onur Akın for their supports.

I also appreciate the support of my invaluable friends Emre Yılmaz, Tahir Volkan Sanlı, Mustafa Batuhan Akıncı, Caner Durak, Özgün Dülger and Kaan Tosun for always promoting me and believing in me.

I would like to thank to my father Orhan, my mother Sema, my little sister Sena Rüya and my grandmother Semra Çataloğlu for their endless supports, their endless prays. I also would like to express my thanks to Fatma Genç, my love, for loving me and supporting me all the time.

I also thank to The Scientific and Technological Research Council of Turkey (TÜBİTAK) “2211 Yurt İçi Lisansüstü Burs Programı” for supporting me financially during my graduate level education.

The work presented herein has been partially funded by the European Community's Seventh Framework Programme (FP7) under the Grant Agreement 314139. The CHANGE project ("Combined morphing assessment software using

flight envelope data and mission based morphing prototype wing development") is a L1 project funded under the topic AAT.2012.1.1-2 involving nine partners. The project started in August, 1, 2012. The author gratefully acknowledges the support given.

## TABLE OF CONTENTS

ABSTRACT .....	v
ÖZ.....	vii
ACKNOWLEDGEMENTS .....	x
TABLE OF CONTENTS .....	xii
LIST OF TABLES .....	xv
LIST OF FIGURES.....	xvii
LIST OF SYMBOLS .....	xxviii
LIST OF ABBREVIATIONS .....	xxix
CHAPTERS	
1. INTRODUCTION.....	1
1.1 Motivation of the Thesis .....	1
1.2 Layout of the Thesis.....	2
1.3 Limitations of the Thesis.....	3
2. LITERATURE REVIEW.....	5
2.1 Introduction .....	5
2.2 Definition of Morphing .....	6
2.3 Benefits of Morphing .....	7
2.4 Drawbacks of Morphing.....	8
2.5 Origins of Morphing Aerial Vehicles.....	9
2.6 Contribution of CHANGE Project Partners to Morphing Concepts .....	12
3. DESIGN OF THE HYBRID TRAILING EDGE CONTROL SURFACE.....	17
3.1 Introduction .....	17
3.2 Design of the C Part .....	20
3.3 Design of the Compliant Part .....	20
3.4 Design of the Rigid Part .....	22
3.4.1 Design of the Open Cell.....	22
3.4.2 Design of the Closed Cell .....	24

3.5 Utilization of Servo Actuators .....	25
3.5.1 Selection of Servo Actuators.....	25
3.5.2 Connection of Servo Actuators to C Part.....	29
3.5.3 Location of the Servo Actuators .....	31
3.6 Discussion and Conclusion .....	32
4. FINITE ELEMENT ANALYSIS OF THE HYBRID TRAILING EDGE CONTROL SURFACE IN IN-VACUO CONDITION.....	33
4.1 Introduction .....	33
4.2 Finite Element Analysis of Open Cell Design in in-Vacuo Condition .....	33
4.2.1 Finite Element Modelling of Open Cell Design .....	35
4.2.2 Analysis of Camber and Decamber Variations of Open Cell Design.....	41
4.2.2.1 Camber Variations of Open Cell Design – Linear Case .....	42
4.2.2.2 Camber Variations of Open Cell Design – Non-linear Case with Only Geometric Non-linearities .....	44
4.2.2.3 Camber Variations of Open Cell Design – Non-linear Case with Geometric and Material Non-linearities.....	46
4.2.2.4 Decamber Variations of Open Cell Design – Linear Case .....	49
4.2.2.5 Decamber Variations of Open Cell Design – Non-linear Case with Only Geometric Non-linearities .....	53
4.2.2.6 Decamber Variations of Open Cell Design – Non-linear Case with Geometric and Material Non-linearities.....	57
4.2.2.7 Discussion and Conclusion .....	62
4.2.3 Analysis of Material Variations of Open Cell Design .....	64
4.2.4 Analysis of Geometric Variations of Open Cell Design.....	71
4.2.5 Analysis of Servo Actuator Variations of Open Cell Design .....	78
4.2.5.1 Case 1 .....	79
4.2.5.2 Case 2.....	85
4.2.6 Analysis of Twist of Open Cell Design .....	92
4.3 Finite Element Analysis of Closed Cell Design in in-Vacuo Condition.....	95
4.3.1 Finite Element Modelling of Closed Cell Design .....	95

4.3.2 Analysis of Camber and Decamber Variations of Closed Cell Design.....	98
4.3.2.1 Camber Variations of Closed Cell Design .....	98
4.3.2.2 Decamber Variations of Closed Cell Design .....	100
4.4 Discussion and Conclusion .....	104
5. FINITE ELEMENT ANALYSIS OF THE HYBRID TRAILING EDGE CONTROL SURFACE UNDER AERODYNAMIC LOADING .....	115
5.1 Introduction .....	115
5.2 Aerodynamic Analyses .....	115
5.2.1 Aerodynamic Mesh .....	116
5.2.2 Computational Fluid Dynamics Analyses.....	118
5.3 Finite Element Analysis of Open Cell Design Under Aerodynamic Loading	119
5.3.1 Finite Element Modelling of Open Cell Design .....	119
5.3.2 Analysis of Camber and Decamber Variations of Open Cell Design .....	120
5.4 Finite Element Analysis of Closed Cell Design Under Aerodynamic Loading .....	132
5.4.1 Finite Element Modelling of Closed Cell Design .....	132
5.4.2 Analysis of Camber and Decamber Variations of Closed Cell Design...	133
5.5 Discussion and Conclusion .....	139
6. CONCLUSION .....	145
6.1 General Conclusions .....	145
6.2 Recommendations for Further Studies .....	146
REFERENCES.....	147

## LIST OF TABLES

### TABLES

Table 1: Material Properties of Aluminium [29] .....	20
Table 2: Material Properties of Glass-Fibre Prepreg EHG250-68-37 Composite [31] .....	23
Table 3: Material Properties of Rohacell® 51 RIMA Foam [32] .....	25
Table 4: The Specifications of Volz DA 13-05-60 Servo Actuator [33] .....	26
Table 5: Linearized Material Properties of Neoprene Rubber using Isotropic Linear Elasticity Model .....	42
Table 6: Comparison of Maximum von-Mises Strains between Linear and Non-linear Cases .....	62
Table 7: Comparison of Maximum Combined Beam Stresses between Linear and Non-linear Cases .....	63
Table 8: Comparison of Required Servo Actuator Torques for Servos to Actuate the Upper Portion of the Transmission Parts between Linear and Non-linear Cases .....	63
Table 9: Comparison of Required Servo Actuator Torques for Servos to Actuate the Lower Portion of the Transmission Parts between Linear and Non-linear Cases .....	64
Table 10: Weight Comparison of Analyzed Designs in in-Vacuo Condition.....	106
Table 11: Maximum von-Mises Strains in Analyzed Designs in in-Vacuo Condition .....	107
Table 12: Maximum Combined Beam Stresses in Analyzed Designs in in-Vacuo Condition.....	108
Table 13: Reaction Moments of Servo Actuators to Actuate the Upper Portion of the Transmission Parts in Analyzed Designs in in-Vacuo Condition.....	109
Table 14: Reaction Moments of Servo Actuators to Actuate the Lower Portion of the Transmission Parts in Analyzed Designs in in-Vacuo Condition.....	110

Table 15: Comparison of Averaged Reaction Moments of Servo Actuators to Actuate the Upper Portion of the Transmission Parts in Designs of Servo Actuator Variations .....	111
Table 16: Comparison of Averaged Reaction Moments of Servo Actuators to Actuate the Lower Portion of the Transmission Parts in Designs of Servo Actuator Variations .....	112
Table 17: The Flight Parameters used in Aerodynamic Analyses .....	118
Table 18: Weight Comparison of Analyzed Designs under Aerodynamic Loading	141
Table 19: Maximum von-Mises Strains in Analyzed Designs under Aerodynamic Loading.....	142
Table 20: Maximum Combined Beam Stresses in Analyzed Designs under Aerodynamic Loading.....	142
Table 21: Reaction Moments of Servo Actuators to Actuate the Lower Portion of the Transmission Parts in Analyzed Designs under Aerodynamic Loading.....	143
Table 22: Reaction Moments of Servo Actuators to Actuate the Upper Portion of the Transmission Parts in Analyzed Designs under Aerodynamic Loading.....	143



## LIST OF FIGURES

### FIGURES

Figure 1: Airbus’s Inspiration of Winglets from Eagle’s Wings [1] .....	5
Figure 2: Substantial Changes in Birds’ Wings [6] .....	6
Figure 3: Substantial Changes in Wing Planform Areas; HSM stands for “High Speed Maneuver” [7] .....	7
Figure 4: Clement Ader’s Eole [17].....	9
Figure 5: 1903-2010 Chronology of Fixed Wing Morphing Aerial Vehicles [18]....	10
Figure 6: Chord Extension Mechanism Concept Developed by Gamboa et al. [13] – Retracted View (Upper), Extended View (Lower) .....	12
Figure 7: Span Extension Mechanism Concept Developed by Gamboa et al. [13] – Retracted View (Upper), Extended View (Lower) .....	13
Figure 8: Patent of the Dornier Company, which is used by DLR in Smart Leading Edge Device [11] .....	14
Figure 9: Warping Mechanism used Near the Trailing Edge to Actively Control Wing Warping [22] .....	14
Figure 10: Isometric View of Retracted AdAR Wing [23].....	15
Figure 11: Top View of Extended AdAR Wing; EMC stands for Elastomeric Matrix Composite [23].....	15
Figure 12: METU's Indigenously Designed UAV within7 the scope of TÜBİTAK Project 107M103 [24] .....	16
Figure 13: The Baseline Wing and Trailing Edge Control Surface Profiles.....	17
Figure 14: Isometric View of the Baseline Wing and the Trailing Edge Control Surface .....	18
Figure 15: The Flight Profile of the Unmanned Aerial Vehicle .....	18
Figure 16: Side View of a Typical Hybrid Trailing Edge Control Surface Design ...	19
Figure 17: The Experimental Test Data of Neoprene Rubber [29].....	21
Figure 18: Open Cell Design of the Hybrid Trailing Edge Control Surface .....	23

Figure 19: Closed Cell Design of the Hybrid Trailing Edge Control Surface .....	24
Figure 20: Closed Cell Design of the Hybrid Trailing Edge Control Surface with Foam Included.....	25
Figure 21: CAD Model of Volz DA 13-05-60 Servo Actuator [33].....	26
Figure 22: The Built-in Moment Arm of Volz DA 13-05-60 Servo Actuator [33] ...	27
Figure 23: The Modified Moment Arm of Volz DA 13-05-60 Servo Actuator .....	27
Figure 24: Actuation Rods Designed for Volz DA 13-05-60 Servo Actuator .....	28
Figure 25: The Assembly of Volz DA 13-05-60 Servo Actuator .....	28
Figure 26: L-Shaped Connection Designed for the Servo Actuators .....	29
Figure 27: Typical Full Assembly of Volz DA 13-05-60 Servo Actuator with Fastener .....	30
Figure 28: Female Guide on the C Part to Eliminate Misalignment of Bonding of L- Shaped Fasteners .....	30
Figure 29: Top View of Servo Actuators in Open Cell Design .....	31
Figure 30: Top View of Servo Actuators in Open Cell Design – Zoomed View .....	31
Figure 31: Side View of Open Cell Design along with Servo Actuators and Fasteners .....	32
Figure 32: Side View of Open Cell Design with Dimensions .....	34
Figure 33: Side View of C Bar with Dimensions.....	34
Figure 34: The Generated Geometry of Open Cell Design for Finite Element Model .....	35
Figure 35: Mesh Convergence Analysis for Compliant Part Element Size [35] .....	36
Figure 36: Mesh Convergence Analysis for Rigid Part Element Size [35] .....	36
Figure 37: Isometric View of Generated Mesh for Open Cell Design.....	37
Figure 38: Side View of the Generated Mesh for Open Cell Design.....	37
Figure 39: Meshed View of Moment Arms and Actuation Rods with Assigned Cross- Section Properties.....	38
Figure 40: Coinciding Edges of Compliant Part, Rigid Part and Skin Parts of C Part .....	39

Figure 41: Connection of Actuation Rods to Transmission Parts in Open Cell Design .....	39
Figure 42: Coinciding Nodes of Moment Arms and Actuation Rods.....	40
Figure 43: Boundary Condition Applied to the Leading Edge of the C Bar.....	41
Figure 44: Transverse Displacement Contours for 15.2 [mm] Camber of Open Cell Design – Linear Case – Maximum 15.044 [mm].....	43
Figure 45: von-Mises Strain Distribution Contours for 15.2 [mm] Camber of Open Cell Design – Linear Case – Maximum 0.226 [mm/mm].....	43
Figure 46: The Combined Beam Stresses for 15.2 [mm] Camber of Open Cell Design – Linear Case – Maximum 77.238 [MPa].....	44
Figure 47: Transverse Displacement Contours for 15.2 [mm] Camber of Open Cell Design – Non-linear Case with Only Geometric Non-linearities – Maximum 15.354 [mm].....	45
Figure 48: von-Mises Strain Distribution Contours for 15.2 [mm] Camber of Open Cell Design – Non-linear Case with Only Geometric Non-linearities – Maximum 0.208 [mm/mm].....	45
Figure 49: The Combined Beam Stresses for 15.2 [mm] Camber of Open Cell Design – Non-linear Case with Only Geometric Non-linearities – Maximum 67.516 [MPa] .....	46
Figure 50: Transverse Displacement Contours for 15.2 [mm] Camber of Open Cell Design – Non-linear Case with Geometric and Material Non-linearities – Maximum 15.318 [mm] .....	47
Figure 51: von-Mises Strain Distribution Contours for 15.2 [mm] Camber of Open Cell Design – Non-linear Case with Geometric and Material Non-linearities – Maximum 0.209 [mm/mm].....	47
Figure 52: The Combined Beam Stresses for 15.2 [mm] Camber of Open Cell Design – Non-linear Case with Geometric and Material Non-linearities – Maximum 65.905 [MPa] .....	48
Figure 53: Transverse Displacement Contours for 15.2 [mm] Decamber of Open Cell Design – Linear Case – Maximum 15.164 [mm].....	49

Figure 54: von-Mises Strain Distribution Contours for 15.2 [mm] Decamber of Open Cell Design – Linear Case – Maximum 0.222 [mm/mm].....	50
Figure 55: The Combined Beam Stresses for 15.2 [mm] Decamber of Open Cell Design – Linear Case – Maximum 146.040 [MPa] .....	50
Figure 56: Transverse Displacement Contours for 20.2 [mm] Decamber of Open Cell Design – Linear Case – Maximum 20.659 [mm].....	51
Figure 57: von-Mises Strain Distribution Contours for 20.2 [mm] Decamber of Open Cell Design – Linear Case – Maximum 0.310 [mm/mm].....	52
Figure 58: The Combined Beam Stresses for 20.2 [mm] Decamber of Open Cell Design – Linear Case – Maximum 149.120 [MPa] .....	52
Figure 59: Transverse Displacement Contours for 15.2 [mm] Decamber of Open Cell Design – Non-linear Case with Only Geometric Non-linearities – Maximum 15.336 [mm].....	54
Figure 60: von-Mises Strain Distribution Contours for 15.2 [mm] Decamber of Open Cell Design – Non-linear Case with Only Geometric Non-linearities – Maximum 0.209 [mm/mm] .....	54
Figure 61: The Combined Beam Stresses for 15.2 [mm] Decamber of Open Cell Design – Non-linear Case with Only Geometric Non-linearities – Maximum 112.010 [MPa].....	55
Figure 62: Transverse Displacement Contours for 20.2 [mm] Decamber of Open Cell Design – Non-linear Case with Only Geometric Non-linearities – Maximum 20.483 [mm].....	56
Figure 63: von-Mises Strain Distribution Contours for 20.2 [mm] Decamber of Open Cell Design – Non-linear Case with Only Geometric Non-linearities – Maximum 0.280 [mm/mm] .....	56
Figure 64: The Combined Beam Stresses for 20.2 [mm] Decamber of Open Cell Design – Non-linear Case with Only Geometric Non-linearities – Maximum 93.857 [MPa].....	57

Figure 65: Transverse Displacement Contours for 15.2 [mm] Decamber of Open Cell Design – Non-linear Case with Geometric and Material Non-linearities – Maximum 15.313 [mm] .....	58
Figure 66: von-Mises Strain Distribution Contours for 15.2 [mm] Decamber of Open Cell Design – Non-linear Case with Geometric and Material Non-linearities – Maximum 0.210 [mm/mm] .....	59
Figure 67: The Combined Beam Stresses for 15.2 [mm] Decamber of Open Cell Design – Non-linear Case with Geometric and Material Non-linearities – Maximum 112.650 [MPa] .....	59
Figure 68: Transverse Displacement Contours for 20.2 [mm] Decamber of Open Cell Design – Non-linear Case with Geometric and Material Non-linearities – Maximum 20.452 [mm] .....	60
Figure 69: von-Mises Strain Distribution Contours for 20.2 [mm] Decamber of Open Cell Design – Non-linear Case with Geometric and Material Non-linearities – Maximum 0.281 [mm/mm] .....	61
Figure 70: The Combined Beam Stresses for 20.2 [mm] Decamber of Open Cell Design – Non-linear Case with Geometric and Material Non-linearities – Maximum 94.691 [MPa] .....	61
Figure 71: Transverse Displacement Contours for 15.2 [mm] Camber of Open Cell Design – The Rigid Part is Composite – Maximum 15.014 [mm] .....	66
Figure 72: von-Mises Strain Distribution Contours for 15.2 [mm] Camber of Open Cell Design – The Rigid Part is Composite – Maximum 0.205 [mm/mm] .....	66
Figure 73: The Combined Beam Stresses for 15.2 [mm] Camber of Open Cell Design – The Rigid Part is Composite – Maximum 46.357 [MPa] .....	67
Figure 74: Transverse Displacement Contours for 15.2 [mm] Decamber of Open Cell Design – The Rigid Part is Composite – Maximum 15.273 [mm] .....	68
Figure 75: von-Mises Strain Distribution Contours for 15.2 [mm] Decamber of Open Cell Design – The Rigid Part is Composite – Maximum 0.212 [mm/mm] .....	68
Figure 76: The Combined Beam Stresses for 15.2 [mm] Decamber of Open Cell Design – The Rigid Part is Composite – Maximum 97.868 [MPa] .....	69

Figure 77: Transverse Displacement Contours for 20.2 [mm] Decamber of Open Cell Design – The Rigid Part is Composite – Maximum 20.110 [mm] .....	70
Figure 78: von-Mises Strain Distribution Contours for 20.2 [mm] Decamber of Open Cell Design – The Rigid Part is Composite – Maximum 0.282 [mm/mm] .....	70
Figure 79: The Combined Beam Stresses for 20.2 [mm] Decamber of Open Cell Design – The Rigid Part is Composite – Maximum 95.739 [MPa] .....	71
Figure 80: Transverse Displacement Contours for 15.2 [mm] Camber of Open Cell Design – The Skin Thicknesses are 1 [mm] – Maximum 15.373 [mm] .....	72
Figure 81: von-Mises Strain Distribution Contours for 15.2 [mm] Camber Increase of Open Cell Design – The Skin Thicknesses are 1 [mm] – Maximum 0.201 [mm/mm].....	73
Figure 82: The Combined Beam Stresses for 15.2 [mm] Camber Increase of Open Cell Design – The Skin Thicknesses are 1 [mm] – Maximum 34.329 [MPa] ...	73
Figure 83: Transverse Displacement Contours for 15.2 [mm] Decamber of Open Cell Design – The Skin Thicknesses are 1 [mm] – Maximum 15.419 [mm] .....	74
Figure 84: von-Mises Strain Distribution Contours for 15.2 [mm] Decamber of Open Cell Design – The Skin Thicknesses are 1 [mm] – Maximum 0.208 [mm/mm]	75
Figure 85: The Combined Beam Stresses for 15.2 [mm] Decamber of Open Cell Design – The Skin Thicknesses are 1 [mm] – Maximum 67.123 [MPa].....	75
Figure 86: Transverse Displacement Contours for 20.2 [mm] of Open Cell Design – The Skin Thicknesses are 1 [mm] – Maximum 20.597 [mm] .....	76
Figure 87: von-Mises Strain Distribution Contours for 20.2 [mm] Decamber of Open Cell Design – The Skin Thicknesses are 1 [mm] – Maximum 0.268 [mm/mm]	77
Figure 88: The Combined Beam Stresses for 20.2 [mm] Decamber of Open Cell Design – The Skin Thicknesses are 1 [mm] – Maximum 69.961 [MPa].....	77
Figure 89: Top View of Servo Actuators in Open Cell Design with Dimensions – Case 1 .....	78
Figure 90: Top View of Servo Actuators in Open Cell Design with Dimensions – Case 2 .....	79

Figure 91: Transverse Displacement Contours for 15.2 [mm] Camber of Open Cell Design – Servo Actuators Variation Case 1 – Maximum 15.221 [mm] .....	80
Figure 92: von-Mises Strain Distribution Contours for 15.2 [mm] Camber of Open Cell Design – Servo Actuators Variation Case 1 – Maximum 0.198 [mm/mm]80	
Figure 93: The Combined Beam Stresses for 15.2 [mm] Camber of Open Cell Design – Servo Actuators Variation Case 1 – Maximum 27.197 [MPa] .....	81
Figure 94: Transverse Displacement Contours for 15.2 [mm] Decamber of Open Cell Design – Servo Actuators Variation Case 1 – Maximum 15.402 [mm] .....	82
Figure 95: von-Mises Strain Distribution Contours for 15.2 [mm] Decamber of Open Cell Design – Servo Actuators Variation Case 1 – Maximum 0.207 [mm/mm]82	
Figure 96: The Combined Beam Stresses for 15.2 [mm] Decamber of Open Cell Design – Servo Actuators Variation Case 1 – Maximum 52.356 [MPa].....	83
Figure 97: Transverse Displacement Contours for 20.2 [mm] Decamber of Open Cell Design – Servo Actuators Variation Case 1 – Maximum 20.566 [mm] .....	84
Figure 98: von-Mises Strain Distribution Contours for 20.2 [mm] Decamber of Open Cell Design – Servo Actuators Variation Case 1 – Maximum 0.262 [mm/mm]84	
Figure 99: The Combined Beam Stresses for 20.2 [mm] Decamber of Open Cell Design – Servo Actuators Variation Case 1 – Maximum 55.134 [MPa].....	85
Figure 100: Transverse Displacement Contours for 15.2 [mm] Camber of Open Cell Design – Servo Actuators Variation Case 2 – Maximum 15.442 [MPa].....	86
Figure 101: von-Mises Strain Distribution Contours for 15.2 [mm] Camber of Open Cell Design – Servo Actuators Variation Case 2 – Maximum 0.203 [mm/mm]87	
Figure 102: The Combined Beam Stresses for 15.2 [mm] Camber of Open Cell Design – Servo Actuators Variation Case 2 – Maximum 33.000 [MPa].....	87
Figure 103: Transverse Displacement Contours for 15.2 [mm] Decamber of Open Cell Design – Servo Actuators Variation Case 2 – Maximum 15.237 [mm] ....	88
Figure 104: von-Mises Strain Distribution Contours for 15.2 [mm] Decamber of Open Cell Design – Servo Actuators Variation Case 2 – Maximum 0.207 [mm/mm] .....	89

Figure 105: The Combined Beam Stresses for 15.2 [mm] Decamber of Open Cell Design – Servo Actuators Variation Case 2 – Maximum 64.317 [MPa] .....	89
Figure 106: Transverse Displacement Contours for 20.2 [mm] Decamber of Open Cell Design – Servo Actuators Variation Case 2 – Maximum 20.553 [mm].....	90
Figure 107: von-Mises Strain Distribution Contours for 20.2 [mm] Decamber of Open Cell Design – Servo Actuators Variation Case 2 – 0.255 [mm/mm] .....	91
Figure 108: The Combined Beam Stresses for 20.2 [mm] Decamber of Open Cell Design – Servo Actuators Variation Case 2 – Maximum 67.876 [MPa] .....	91
Figure 109: Transverse Displacement Contours for Twist of Open Cell Design – Maximum 13.462 [mm] .....	93
Figure 110: von-Mises Strain Distribution Contours for Twist of Open Cell Design – Maximum 0.207 [mm/mm] .....	94
Figure 111: The Combined Beam Stresses for Twist of Open Cell Design – Maximum 66.803 [MPa] .....	94
Figure 112: The Generated Geometry of Open Cell Design for Finite Element Model .....	96
Figure 113: Isometric View of Generated Mesh for Closed Cell Design .....	97
Figure 114: Side View of Generated Mesh for Closed Cell Design .....	97
Figure 115: Transverse Displacement Contours for 15.2 [mm] Camber of Closed Cell Design – Maximum 15.310 [mm] .....	99
Figure 116: von-Mises Strain Distribution Contours for 15.2 [mm] Camber of Closed Cell Design – Maximum 0.207 [mm/mm] .....	99
Figure 117: The Combined Beam Stresses for 15.2 [mm] Camber of Closed Cell Design – Maximum 74.307 [MPa] .....	100
Figure 118: Transverse Displacement Contours for 15.2 [mm] Decamber of Closed Cell Design – Maximum 15.113 [mm] .....	101
Figure 119: von-Mises Strain Distribution Contours for 15.2 [mm] Decamber of Closed Cell Design – Maximum 0.194 [mm/mm] .....	101
Figure 120: The Combined Beam Stresses for 15.2 [mm] Decamber of Closed Cell Design – Maximum 81.350 [MPa] .....	102



Figure 121: Transverse Displacement Contours for 20.2 [mm] Decamber of Closed Cell Design – Maximum 20.056 [mm] .....	103
Figure 122: von-Mises Strain Distribution Contours for 20.2 [mm] Decamber of Closed Cell Design – Maximum 0.260 [mm/mm].....	103
Figure 123: The Combined Beam Stresses for 20.2 [mm] Decamber of Closed Cell Design – Maximum 149.380 [MPa] .....	104
Figure 124: Generated Aerodynamic Mesh over the Wing .....	116
Figure 125: Generated Boundary Layer Mesh over the Wing Surface.....	117
Figure 126: Generated Hemisphere Outer Domain Mesh.....	117
Figure 127: Applied Boundary Conditions to Open Cell Design under Aerodynamic Loading .....	120
Figure 128: Pressure Contours of Applied Aerodynamic Loading for 15.2 [mm] Camber – Upper Surface .....	121
Figure 129: Pressure Contours of Applied Aerodynamic Loading for 15.2 [mm] Camber – Lower Surface .....	121
Figure 130: Transverse Displacement Contours for 15.2 [mm] Camber of Open Cell Design Under Aerodynamic Loading – Maximum 15.233 [mm].....	122
Figure 131: Pressure Contours of Applied Aerodynamic Loading for 15.2 [mm] Decamber – Upper Surface .....	123
Figure 132: Pressure Contours of Applied Aerodynamic Loading for 15.2 [mm] Decamber – Lower Surface.....	123
Figure 133: Transverse Displacement Contours for 15.2 [mm] Decamber of Open Cell Design Under Aerodynamic Loading – Maximum 15.618 [mm] .....	124
Figure 134: Pressure Contours of Applied Aerodynamic Loading for 20.2 [mm] Decamber – Upper Surface .....	125
Figure 135: Pressure Contours of Applied Aerodynamic Loading for 20.2 [mm] Decamber – Lower Surface.....	125
Figure 136: Transverse Displacement Contours for 15.2 [mm] Camber of Open Cell Design Under Aerodynamic Loading – Skin Thicknesses are 1.5 [mm] – Maximum 15.468 [mm] .....	127

Figure 137: von-Mises Strain Distribution Contours for 15.2 [mm] Camber of Open Cell Design Under Aerodynamic Loading – Skin Thicknesses are 1.5 [mm] – Maximum 0.200 [mm/mm] .....	127
Figure 138: The Combined Beam Stresses for 15.2 [mm] Camber of Open Cell Design Under Aerodynamic Loading – Skin Thicknesses are 1.5 [mm] – Maximum 28.225 [MPa] .....	128
Figure 139: Transverse Displacement Contours for 15.2 [mm] Decamber of Open Cell Design Under Aerodynamic Loading – Skin Thicknesses are 1.5 [mm] – Maximum 15.652 [mm] .....	129
Figure 140: von-Mises Strain Distribution Contours for 15.2 [mm] Decamber of Open Cell Design Under Aerodynamic Loading – Skin Thicknesses are 1.5 [mm] – Maximum 0.227 [mm/mm] .....	129
Figure 141: The Combined Beam Stresses for 15.2 [mm] Decamber of Open Cell Design Under Aerodynamic Loading – Skin Thicknesses are 1.5 [mm] – Maximum 42.591 [MPa] .....	130
Figure 142: Transverse Displacement Contours for 20.2 [mm] Decamber of Open Cell Design Under Aerodynamic Loading – Skin Thicknesses are 1.5 [mm] – Maximum 20.455 [mm] .....	131
Figure 143: von-Mises Strain Distribution Contours for 20.2 [mm] Decamber of Open Cell Design Under Aerodynamic Loading – Skin Thicknesses are 1.5 [mm] – Maximum 0.273 [mm/mm] .....	131
Figure 144: The Combined Beam Stresses for 20.2 [mm] Decamber of Open Cell Design Under Aerodynamic Loading – Skin Thicknesses are 1.5 [mm] – Maximum 39.186 [MPa] .....	132
Figure 145: Applied Boundary Conditions to Closed Cell Design under Aerodynamic Loading.....	133
Figure 146: Transverse Displacement Contours for 15.2 [mm] Camber of Closed Cell Design Under Aerodynamic Loading – Maximum 15.575 [mm] .....	134
Figure 147: von-Mises Strain Distribution Contours for 15.2 [mm] Camber of Closed Cell Design Under Aerodynamic Loading – Maximum 0.207 [mm/mm] .....	134

Figure 148: The Combined Beam Stresses for 15.2 [mm] Camber of Closed Cell Design Under Aerodynamic Loading – Maximum 79.632 [MPa] .....	135
Figure 149: Transverse Displacement Contours for 15.2 [mm] Decamber of Closed Cell Design Under Aerodynamic Loading – Maximum 15.295 [mm] .....	136
Figure 150: von-Mises Strain Distribution Contours for 15.2 [mm] Decamber of Closed Cell Design Under Aerodynamic Loading – Maximum 0.212 [mm/mm] .....	136
Figure 151: The Combined Beam Stresses for 15.2 [mm] Decamber of Closed Cell Design Under Aerodynamic Loading – Maximum 87.234 [MPa] .....	137
Figure 152: Transverse Displacement Contours for 20.2 [mm] Decamber of Closed Cell Design Under Aerodynamic Loading – Maximum 20.299 [mm] .....	138
Figure 153: von-Mises Strain Distribution Contours for 20.2 [mm] Decamber of Closed Cell Design Under Aerodynamic Loading – Maximum 0.278 [mm/mm] .....	138
Figure 154: The Combined Beam Stresses for 20.2 [mm] Decamber of Closed Cell Design Under Aerodynamic Loading – Maximum 162.250 [MPa] .....	139

## LIST OF SYMBOLS

$\rho$	Density
$E$	Young's Modulus
$\nu$	Poisson's Ratio
$G$	Shear Modulus

## **LIST OF ABBREVIATIONS**

CHANGE	Combined morphing assessment software using flight envelope data and mission based morphing wing prototype development
DARPA	The Defense Advanced Research Projects Agency
NOVEMOR	Novel Air Vehicle Configurations: From Fluttering Wings to Morphing Wings
SADE	Smart High Lift Devices for Next Generation Wings
DLR	The German Aerospace Center
AdAR	Adaptive Aspect Ratio
METU	Middle East Technical University
TÜBİTAK	The Scientific and Technological Research Council of Turkey
TAI	Turkish Aerospace Industries
UAV	Unmanned Aerial Vehicle
CAD	Computer-aided Design
CFD	Computational Fluid Dynamics
SU2	Stanford University Unstructured
RANS	Reynolds Averaged Navier-Stokes



# CHAPTER 1

## INTRODUCTION

### 1.1 Motivation of the Thesis

Aerial vehicles are designed and optimized for a specific flight condition in which the aerial vehicle spends most of its mission time. Therefore, aerial vehicles are performing best in the intended flight condition. In off-design conditions, the overall performance of the aerial vehicle usually reduces and that requires additional mechanisms for improved performance. Advances in actuation mechanisms, smart materials and manufacturing techniques have enabled research to focus on morphing concepts. By the help of morphing, it is becoming possible to optimize the aerial vehicle in off-design conditions as well. Hence, a new research field has been emerged named as Morphing Aerial Vehicles.

This thesis is devoted to the structural design and analysis of a novel hybrid trailing edge control surface that can perform both camber and decamber morphings. The designed control surface is hingeless and seamless, which eliminates the existing gaps between the flaps and the wing, allowing a smooth transition of airflow over the control surface.

The study was conducted within the scope of the CHANGE Project (Combined morphing Assessment software using flight Envelope data and mission based morphing prototype wing development) which is a project of 7th Framework Programme of European Commission.

## **1.2 Layout of the Thesis**

Chapter 2 is devoted to the literature review of morphing aerial vehicles. Initially, definition of morphing is given and then followed by its advantages and disadvantages. Origins of the morphing aerial vehicles are also addressed. Finally, the outline of the contribution of the CHANGE Project partners to the morphing concepts are given.

In Chapter 3, the design of the hybrid trailing edge control surface is presented. The parts of the control surface and their designs are mentioned and illustrated. Two distinct control surface designs, so-called "open cell design" and "closed cell design" are presented. The properties, connections and locations of the utilized servo actuators to actuate the control surface are also addressed.

Chapter 4 is dedicated to the finite element analysis of the hybrid trailing edge control surface in in-vacuo condition. Initially, the capabilities of the designed control surface in terms of the cambering and decambering for open cell design is shown. Then, trade-off studies including material, geometric and servo actuators variations for open cell design are presented. The twist of open cell design is also analyzed. Finally, the camber and decamber variations of closed cell design are shown.

In Chapter 5, the finite element analysis of the hybrid trailing edge control surface under aerodynamic loading is presented. Camber and decamber variations of both open cell and closed cell designs are assessed under aerodynamic loading and presented.

Chapter 6 gives the general conclusions. Additionally, the recommendations for the future work are also addressed.



### **1.3 Limitations of the Thesis**

In this thesis, the study is limited to design and analysis of hybrid trailing edge control surface. The installation of the control surface to the wing is not considered in the study. Therefore, intermediate connections between the control surface and the wing are not included in the thesis.

The applied aerodynamic loading cases are limited to 1g aerodynamic loading. Hence, the behavior of the control surface under higher load cases are not considered in the thesis.

During the design of the control surface, the necessary electrical equipment of servo actuators such as cabling, battery selection and placement of these equipment are also not considered.



## CHAPTER 2

### LITERATURE REVIEW

In this chapter, literature review is presented. After a brief introduction, definition of the term "morphing" is presented and followed by its benefits and drawbacks. Then, origins of morphing aerial vehicles are mentioned. Finally, recent contributions to morphing aerial vehicles are addressed.

#### 2.1 Introduction

Starting from the early ages, humans were observing the nature to overcome it. Great irony is that, the mankind does this by imitating the nature itself. Over centuries, people tried to build apparatus to take advantage over the nature. Examples of such are weapons, cars, ships, aerial vehicles and other devices that are being used in daily life.

Even in ancient eras, mankind wanted to fly like birds to cover the great distances in such short time and to be free from the surface of the earth. As mentioned above, humans started to observe the birds in nature to be able to fly. Even today, engineers and scientists inspired by the nature. For instance, Airbus, which is one of the greatest airplane producers, implements the results of inspiration from the wings of eagles in the wingtips of their aerial vehicles such as Airbus A350 and A380 which can be seen in Figure 1 [1].



Figure 1: Airbus's Inspiration of Winglets from Eagle's Wings [1]

Thanks to the advances in science and technology, Wright Brothers made the dream of all mankind real in 1903 by successfully flying first heavier-than-air vehicle. However, after the first flight had taken place, it was revealed that although science and technology developed enough to create a machine to fly, there was still room for improvement to make aerial vehicles to adapt different flight conditions as birds. Birds are natural flyers who are able to adapt different flight conditions as they need [2, 3]. Likewise, designers are now trying to improve the capability of aerial vehicles to adapt themselves to different flight conditions by using the results of extensive research conducted in this field. At this point, morphing comes into play as a method to add adaptability to different flight environments for the aerial vehicles.

## 2.2 Definition of Morphing

The dictionary meaning of morph is defined as "to change gradually and completely from one thing into another thing usually in a way that is surprising or seems magical" [4].

Özgen et al. defines the morphing aerial vehicle as an aerial vehicle which has the ability to change its wing planform shape substantially during the flight [5]. Such substantial changes are given in Figure 2 and Figure 3.



Figure 2: Substantial Changes in Birds' Wings [6]

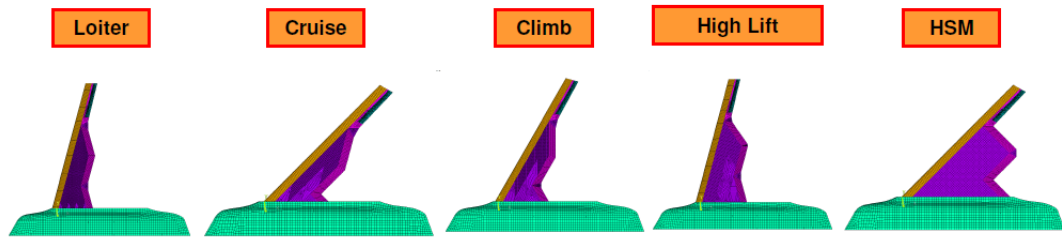


Figure 3: Substantial Changes in Wing Planform Areas; HSM stands for “High Speed Maneuver” [7]

In his Ph.D. thesis, Seigler gives the three phases morphing definition of The Defense Advanced Research Projects Agency (DARPA) as [8]:

- Aerial vehicle can substantially change its state to adapt changing mission environments,
- Aerial vehicle can provide superior system capability which is not possible by reconfiguration,
- Aerial vehicle can achieve the state change by using a design that integrates innovative combinations of advanced materials, actuators, flow controllers and mechanisms.

### 2.3 Benefits of Morphing

Although, theoretically there exists a unique shape for maximizing aerodynamic performance at a certain flight regime; the conventional aerial vehicles' performances are usually optimized only for a single mission phase and will have deficiencies in other mission phase [9]. By the help of morphing, it becomes possible to get an optimum performance in all the intended flight phases of a unique aerial vehicle [5].

Changing the overall planform shape of the wings and/ or control surfaces will lead to an increase in the aerodynamic performance at each phase of the flight and extend the flight envelope of the aerial vehicle so that it can perform multi-role missions. With the help of increase in aerodynamic performance, fuel consumption of

the morphing aerial vehicle will certainly be less compared to the conventional aerial vehicles. For an airline operation, it is stated that 50% of operating expense of airline is due to fuel costs; and moreover, only small amount of fuel consumption can yield substantial savings [10]. Additionally, the harmful gas emission will be reduced due to less fuel consumption and the environmental impact will be drastically reduced. Also, by utilizing the morphing aerial vehicle concepts, it is possible to eliminate the existing gaps between the wing and the conventional control surfaces. These gaps are the major source of the aerodynamic noise [11]. Therefore, morphing aerial vehicles promises the reduction in aerodynamic noise as well.

## **2.4 Drawbacks of Morphing**

Although morphing promises serious benefits in terms of aerodynamic performance and fuel consumption, it has also several disadvantages that should be accounted for. One of the drawbacks of morphing is the increase in the empty weight due to structural complexity. In order to perform morphing, complex internal mechanisms are designed. Eventually, this results in weight increase of the morphing aerial vehicle. In addition, the complex internal mechanisms increase the installation and maintenance cost as well [3].

The estimation of the weight of the wing and the sizing of the morphing aerial vehicle is another drawback since the available weight and sizing data are based on fixed-wings. Therefore, additions due to morphing mechanisms should be carried out carefully. Skillen and Crossley conducted a study on developing morphing wing weight equations and approach to size the morphing aerial vehicles. They showed that the developed method yielded significant changes in results compared with currently available historical data and concluded that calculating the weight of the morphing wings accurately must be an essential part to obtain a credible aircraft sizing results [12].

Another drawback is the high actuation forces required to deform the structure to perform morphing [13]. However, the recent developments promises candidate

materials such as smart materials to be used in morphing vehicles [14], which can reduce the actuation forces and make morphing mechanisms practical. In addition, it is estimated that the weight penalty can also be eliminated by the advances in smart materials [15].

During morphing, configuration change of wings result in change in the aerodynamic center, thus, the aerodynamic loading. Therefore, the control of morphing aircraft becomes complex that needs an additional attention [16].

## 2.5 Origins of Morphing Aerial Vehicles

First morphing aerial vehicle concept had been proposed by Clement Ader, French inventor and engineer, as early as 1890 even before the first successful manned flight. His proposal was an aerial vehicle, named Eole, having the ability to morph its wings which is shown in Figure 4. In his short monograph, which was published in 1909, Clement Ader describes his opinions about the wings of aerial vehicles such that with the advances in aircraft design and construction technologies wings will be adjustable [17].



Figure 4: Clement Ader's Eole [17]

First successfully flown aerial vehicle, The Wright Flyer, actually was a morphing aerial vehicle. Wright Brothers designed the aerial vehicle such that it could roll by warping its wings by the attached cables to the wing which was controlled by the pilot [18]. All these examples reveal that morphing aerial vehicle concept is far

from new. After the first successful manned flight, advances in aviation skyrocketed and different types of aerial vehicles with different purposes were designed and flown. Barbarino et al. presented the chronology of fixed wing aerial vehicles that use morphing technology from 1903 to 2010, which is given in Figure 5 [18].































1903	1931	1931	1932	1937	1947	1951
						
Wright Flyer <i>Twist</i>	Pterodactyl IV <i>Sweep</i>	MAK-10 <i>Span</i>	IS-1 <i>BI-to monoplane</i>	LIG-7 <i>Chord</i>	MAK-123 <i>Span</i>	X 5 <i>Sweep</i>
1952	1964	1964	1966	1967	1967	1969
						
XF10F <i>Sweep</i>	F 111 <i>Sweep</i>	XB 70 <i>Span bending</i>	Su 17 IG <i>Sweep</i>	MIG 23 <i>Sweep</i>	SU 24 <i>Sweep</i>	Tu 22 M <i>Sweep</i>
1970	1972	1974	1974	1979	1981	1985
						
F 14 <i>Sweep</i>	FS 29 <i>Span</i>	B 1 <i>Sweep</i>	Tornado <i>Sweep</i>	AD 1 <i>Obliquing</i>	Tu 160 <i>Sweep</i>	AFTI/F 111 <i>M.A.W.</i>
1993	1994	2001	2002	2003	2004	2005
						
FLYRT <i>Span</i>	MOTHRA <i>Camber</i>	AAL <i>Pitch</i>	F/A 18 <i>A.A.W.</i>	Virginia Tech <i>Span</i>	Univ. of Florida <i>Twist</i>	Univ. of Florida <i>Gull</i>
2006	2006	2007	2007	2007	2008	2010
						
MFX 1 <i>Sweep &amp; Span</i>	Univ. of Florida <i>Sweep</i>	Virginia Tech <i>Camber</i>	Univ. of Florida <i>Folding</i>	MFX 2 <i>Sweep &amp; span</i>	Delft Univ. <i>Sweep</i>	Virignia tech <i>Camber</i>

Figure 5: 1903-2010 Chronology of Fixed Wing Morphing Aerial Vehicles [18]



Figure 5 depicts that chronology of fixed wing morphing aerial vehicles starts with Wright Flyer, which is considered to be first morphing aerial vehicle as mentioned above. Up to late 80's, it is seen that morphing technology was applied to generally military aerial vehicles, especially fighters, and mostly in the form of sweep change because of the fact that wing sweep reduces the compressibility drag [19]. Starting from 2000 with the advances in material science and reduction in the size of actuators, it is seen that the morphing technology has raised the interest of the researchers and various universities implemented morphing approaches to their developed unmanned aerial vehicles to change certain characteristics of the wing such as span, twist and camber.

Nowadays, more universities and institutions are getting involved in the morphing technology and producing aerial vehicles having the ability to morph their wings to improve the aerodynamic performance of the vehicles.

One of the researchs in morphing concept is the NOVEMOR Project (**NO**vel **Air V**ehicle Configurations: From Fluttering Wings to **MOR**phing Flight) which is also a project of 7th Framework Programme of European Comission. The main aim of the project is to investigate novel air vehicle configurations with new lifting concepts and morphing wing solutions to enable cost-effective air transportation [20].

Another research in morphing technology is the CHANGE Project (**C**ombined **morpHing** **A**ssessment software **usiNG** flight **E**nvelope data and mission based morphing prototype wing development) which is an project of 7th Framework Programme of European Comission. The main aim of the project is to design and manufacture an UAV wing that integrates up to four different morphing mechanisms into a single wing and demonstrate the ability of this wing to fly [21].

In the following section, contribution of CHANGE Project partners to the morphing concepts are presented.

## 2.6 Contribution of CHANGE Project Partners to Morphing Concepts

Gamboa et al. developed a morphing wing concept having the ability to extend its chord and span, which are shown in Figure 6 and Figure 7. After performing aerodynamic optimization, they revealed that by using the developed morphing wing concept, more than 30% reduction in drag is possible, which improves the performance in off-design conditions [13].

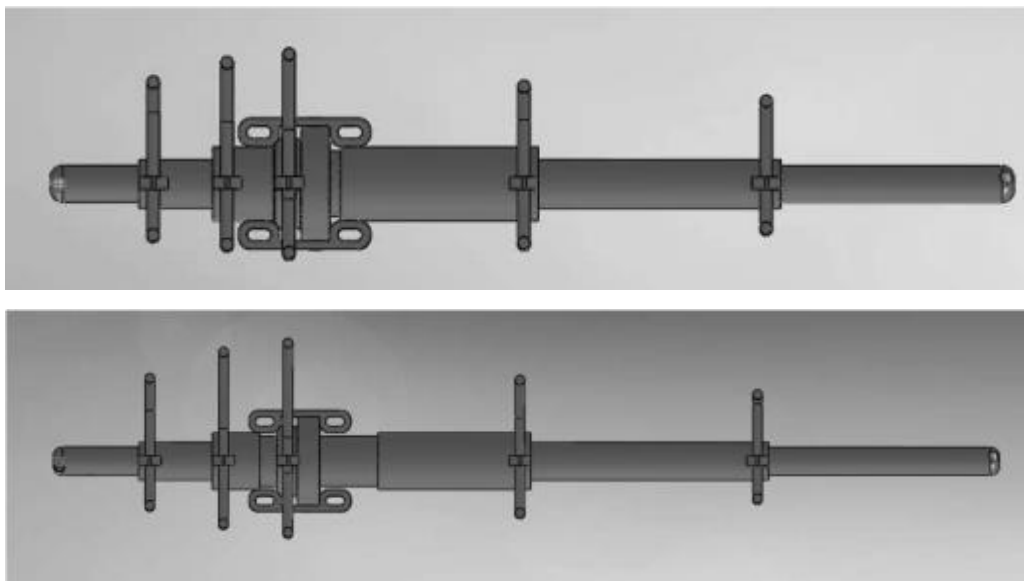


Figure 6: Chord Extension Mechanism Concept Developed by Gamboa et al. [13] – Retracted View (Upper), Extended View (Lower)

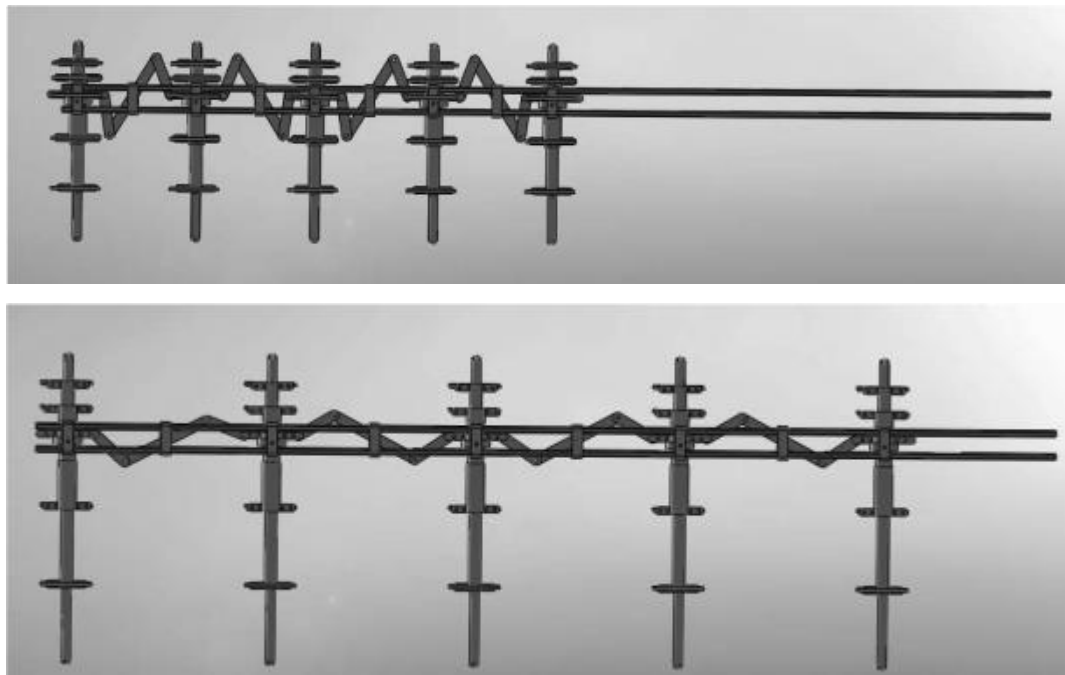


Figure 7: Span Extension Mechanism Concept Developed by Gamboa et al. [13] – Retracted View (Upper), Extended View (Lower)

Within the scope of Smart High Lift Devices for Next Generation Wings (SADE) project, DLR (The German Aerospace Center) has developed a smart leading edge device which is based on the patent of the Dornier Company which is shown in Figure 8. Developed device allows downward deformation of the leading edge by using kinematical mechanism and comprises a flexible skin without gaps and steps [11].

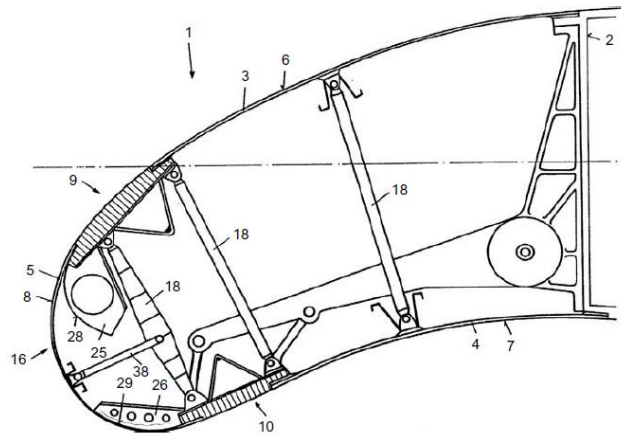


Figure 8: Patent of the Dornier Company, which is used by DLR in Smart Leading Edge Device [11]

Vos et al. developed a novel mechanism for active wing warping. By using open cross section in the developed wing, a threaded rod was placed near the trailing edge, and warping of the wing is actively controlled, which is shown in Figure 9. Developed concept is also tested in wind tunnel which revealed that warping could change the lift coefficient of the wing as much as 0.7 [22].

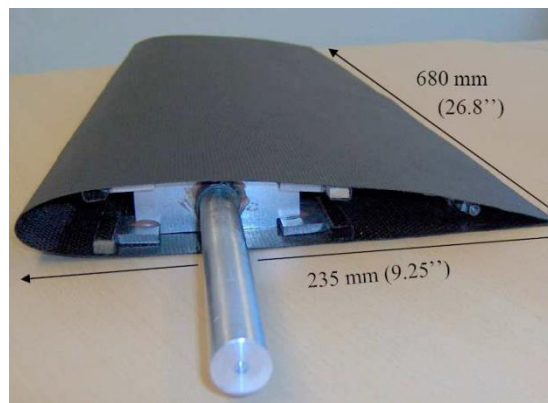


Figure 9: Warping Mechanism used Near the Trailing Edge to Actively Control Wing Warping [22]

Swansea University has introduced a new span morphing concept known as the Adaptive Aspect Ratio (AdAR) wing. The concept couples a continuous and smooth

compliant skin material to an internal structure mechanism to provide significant changes in both span and aspect ratio [23]. Retracted and extended views of the AdAR wing are depicted in Figure 10 and Figure 11.

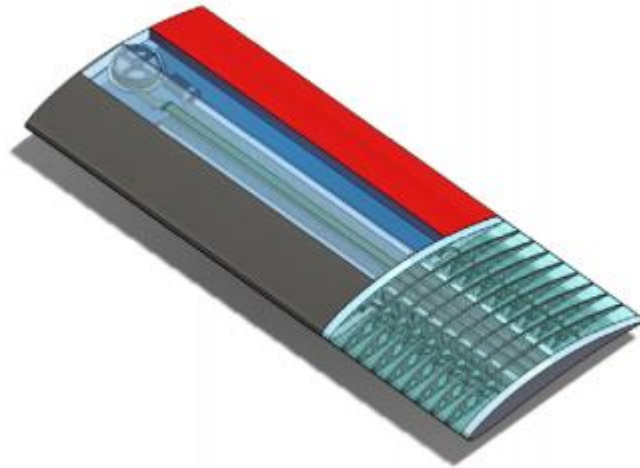


Figure 10: Isometric View of Retracted AdAR Wing [23]

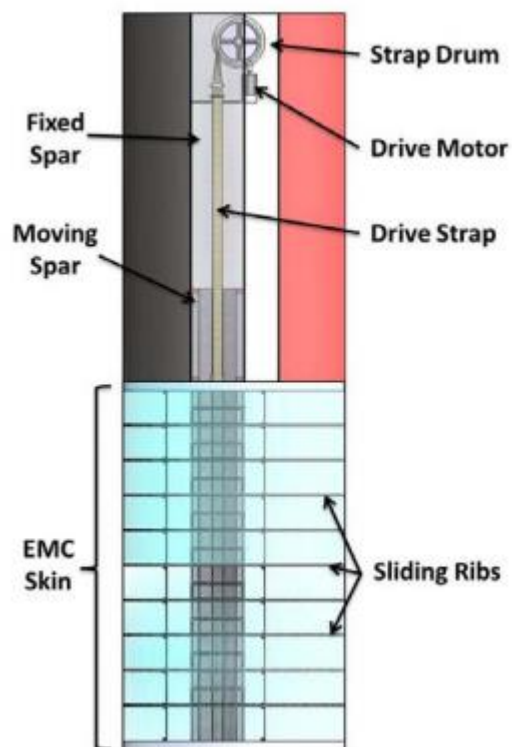


Figure 11: Top View of Extended AdAR Wing; EMC stands for Elastomeric Matrix Composite [23]

In Middle East Technical University (METU) within the scope of TÜBİTAK (The Scientific and Technological Research Council of Turkey) Project 107M103, an unmanned aerial vehicle, having the ability to change camber and twist in the trailing edge control surface, was developed [24]. The concept was inspired from the rotating rib concept [25, 26]. The designed indigenous unmanned aerial vehicle having the unconventional wing shown in Figure 12 was manufactured by Turkish Aerospace Industries (TAI) and various successful flight tests were conducted [24].



Figure 12: METU's Indigenously Designed UAV within the scope of TÜBİTAK Project 107M103 [24]

In his Ph. D. thesis, Ünlüsoy conducted a series of a series of aeroelastic analyses to identify the structural problems due to existing morphing capabilities of the aerial vehicle in structural design process. He showed that the aeroelastic tailoring should be an essential part, otherwise substantial variation in flutter speeds at different morphing configurations is an inevitable result [27]. Additionally, Körpe conducted aerodynamic optimization of morphing wings with performance and geometric constraints in his Ph.D. thesis. During optimization process, he considered the wing optimization for three different cases, namely, only airfoil change, only planform change and combined airfoil and planform change. His results yielded that significant drag reductions can be achieved by morphing wings [28].

## CHAPTER 3

### DESIGN OF THE HYBRID TRAILING EDGE CONTROL SURFACE

#### 3.1 Introduction

In this chapter, design of the hybrid trailing edge control surface is presented. The hybrid trailing edge control surface is a part of an unmanned aerial vehicle (UAV) wing which has NACA6510 airfoil profile. During the studies a chordwise length of 600 [mm] was assigned. The control surface does not have any pre-twist along its span.

The trailing edge control surface to be designed was decided to have a chord length of 180 [mm] and a span of 900 [mm] with a closed profile, that is, there is no discontinuity at the trailing edge. The control surface and baseline wing profiles are shown in Figure 13, and the isometric view of the baseline wing and the control surface is illustrated in Figure 14.

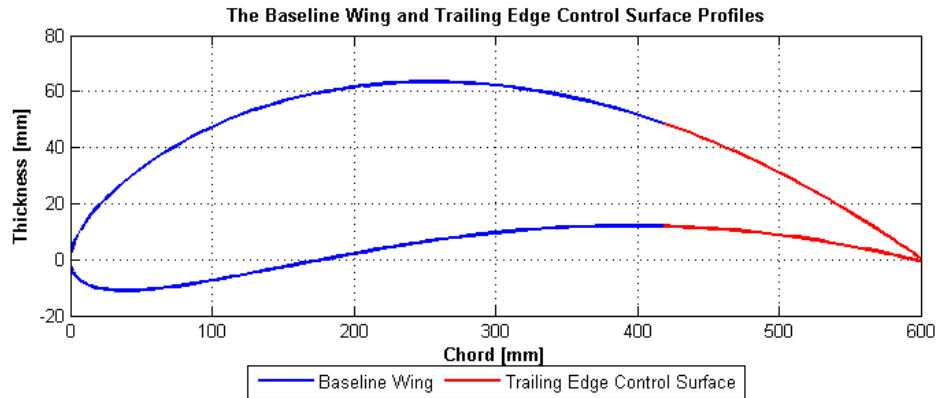


Figure 13: The Baseline Wing and Trailing Edge Control Surface Profiles

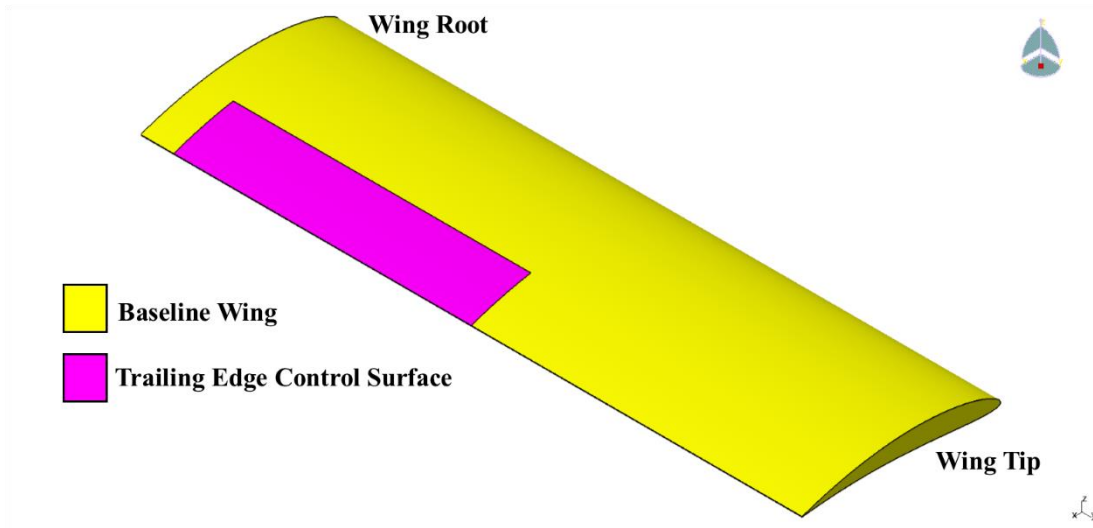


Figure 14: Isometric View of the Baseline Wing and the Trailing Edge Control Surface

The unmanned aerial vehicle, considered in this thesis, has certain flight regimes, namely, take-off, cruise or high-speed dash, loiter, return cruise and landing. The flight profile of the unmanned aerial vehicle is given in Figure 15.

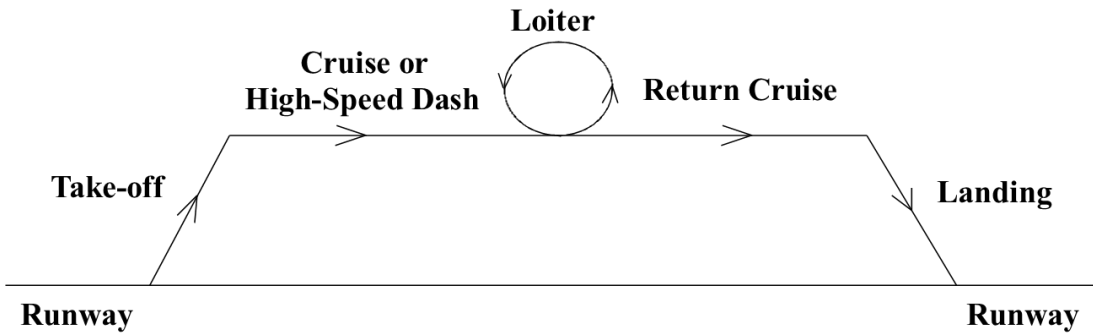


Figure 15: The Flight Profile of the Unmanned Aerial Vehicle

In this context, several target shapes were tried to be achieved during the different phases of the flight to increase the aerodynamic efficiency. During, take-off, profile should have 15.2 [mm] decamber; during cruise or high speed dash, profile should have 20.2 [mm] decamber; during loiter, baseline profile should be maintained since the most of the mission time will be spend on this phase and during landing,



profile should have 15.2 [mm] camber. Therefore, the trailing edge control surface is expected to perform both camber and decamber morphing requirements.

The control surface was designed as an unconventional control surface, which is hingeless and seamless such that the existing gaps between the wing and the conventional control surfaces are eliminated and smooth transition of airflow is achieved over the control surface. The trailing edge control surface was designed as hybrid control surface consisting of both stiff behaving almost rigid and compliant parts to perform its cambering and decambering tasks. The side view of a typical design created in CATIA V5-6R2012 package software, is shown in Figure 16.

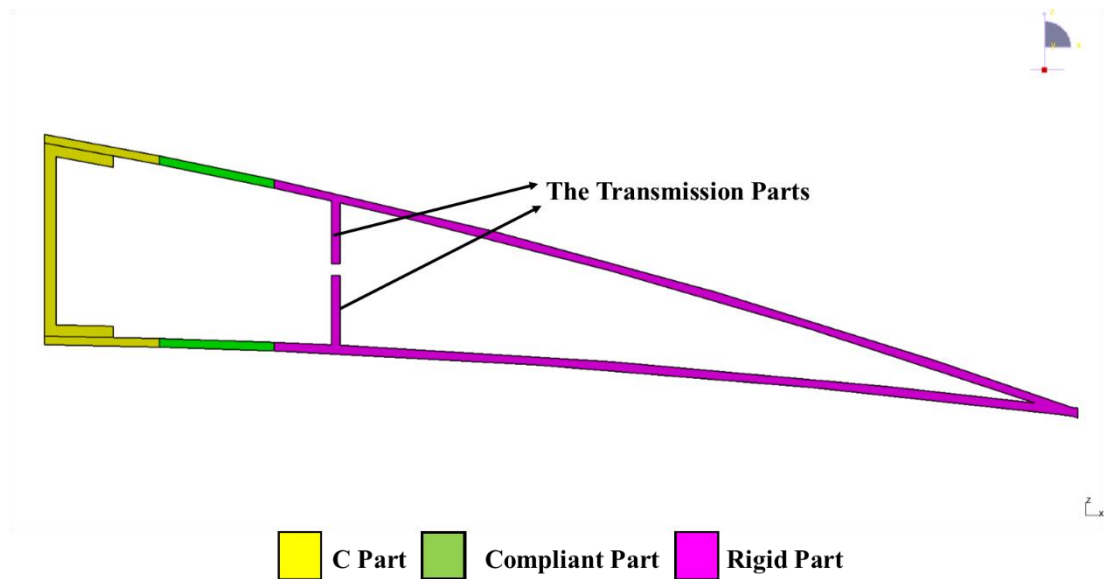


Figure 16: Side View of a Typical Hybrid Trailing Edge Control Surface Design

The external geometry of the trailing edge control surface mainly consists of three parts, namely, a C part, a compliant part and a rigid part. Although, the C part and the rigid part are made of stiff materials, as will be explained in following sections, the C part is named after its shape and the latter part is simply called as the rigid part.

The servo actuators to be utilized for the design transmit their actuation forces to the control surface by the transmission parts. In the following sections, these parts are elaborated further.

### 3.2 Design of the C Part

The primary purpose of the part, which is the so-called “C part” is to provide a means of connection between the control surface and the wing. The control surface is planned to be attached to the wing by using of the C part.

The C part consists of three sub parts, namely, C-bar part and two skin parts, that is, an upper and a lower skin parts. The skin parts can be attached/detached by connection means like studs to/from C-bar to gain access to the control surface internal volume.

Aluminium was used as material of the C part, and the material are shown in Table 1.

Table 1: Material Properties of Aluminium [29]

Density, $\rho$ :	2770 [kg/m <sup>3</sup> ]
Young's Modulus, E:	71 [GPa]
Poisson's Ratio, $\nu$ :	0.33
Tensile Yield Strength:	280 [MPa]
Tensile Ultimate Strength:	310 [MPa]

### 3.3 Design of the Compliant Part

The compliant part is made of a very flexible material so that it can undergo significant amounts of deformations and the control surface can therefore deflect.

The deflection of the control surface is achieved by means of the servo actuators. The servo actuators transmit their actuation forces to the control surface through the transmission parts. The main principle is to have tension in both upper and lower compliant parts during the actuation. This is necessary in order to avoid the

possible slack in the compliant part which could prevail in the case when the compliant part becomes subjected to compression. The motion can then be achieved by applying different actuations to upper and/or lower transmission parts according to the required cambering or decambering. The resulting differential actuation provides the required motion. In order to achieve the cambering the upper compliant part should be extended more than its lower counterpart, and vice versa for decambering.

A compliant material called “Neoprene Rubber” was used in the study. The necessary material properties of Neoprene Rubber was obtained from the material library of ANSYS Workbench v14.0 package software. The stress-strain curves of Neoprene Rubber including uniaxial, biaxial and shear test data are shown in Figure 17.

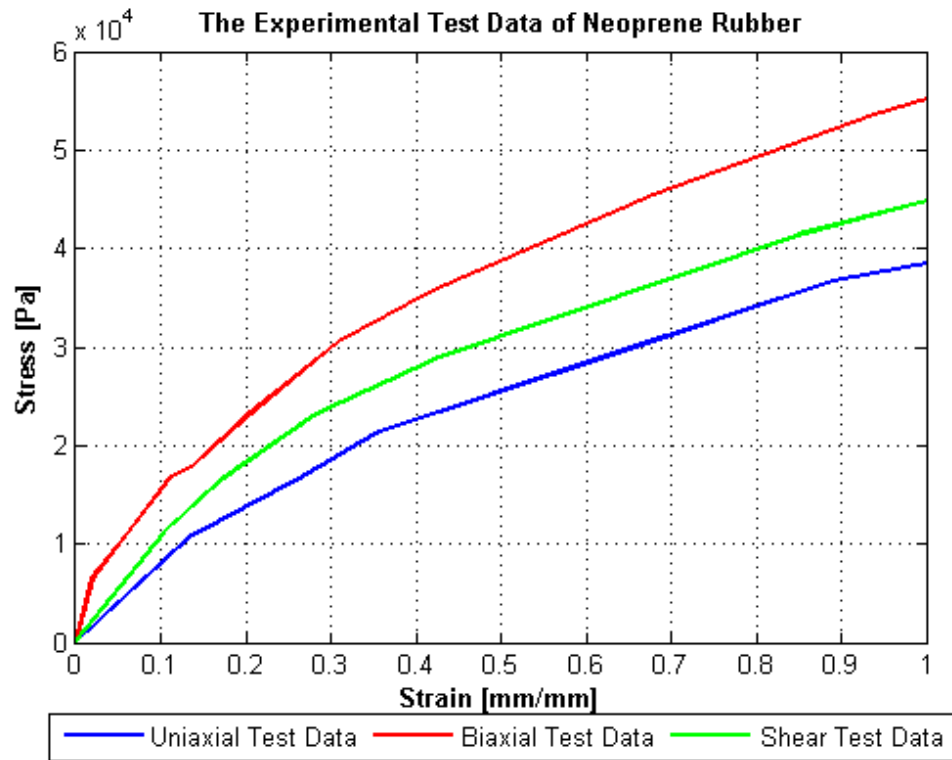


Figure 17: The Experimental Test Data of Neoprene Rubber [29]

It can be seen from Figure 17 that Neoprene Rubber is a non-linear material with very low stiffness. The density of Neoprene Rubber is not specified in ANSYS

Workbench v14.0 package software's material library, hence, its value was taken from the literature as 1250 [kg/m<sup>3</sup>] [30].

During the design it was assumed that the compliant part is connected to both C part and so called the “rigid part” by means of strong adhesives, which provide a rigid connection.

### **3.4 Design of the Rigid Part**

The so-called rigid part is made of materials which are significantly more rigid as compared to the compliant part. The materials which were studied are aluminum and composite, and they are much stiffer compared to the Neoprene Rubber. Hence when the Neoprene deflects the part, then the parts rotates as it was conducting a rigid body motion. The term “rigid part” stems from these facts.

The design of the rigid part was conducted for two different cases called; the open cell design and the closed cell design.

#### **3.4.1 Design of the Open Cell**

In open cell design, the rigid part of the control surface has an opening at the location of the transmission parts, which is shown in Figure 18.

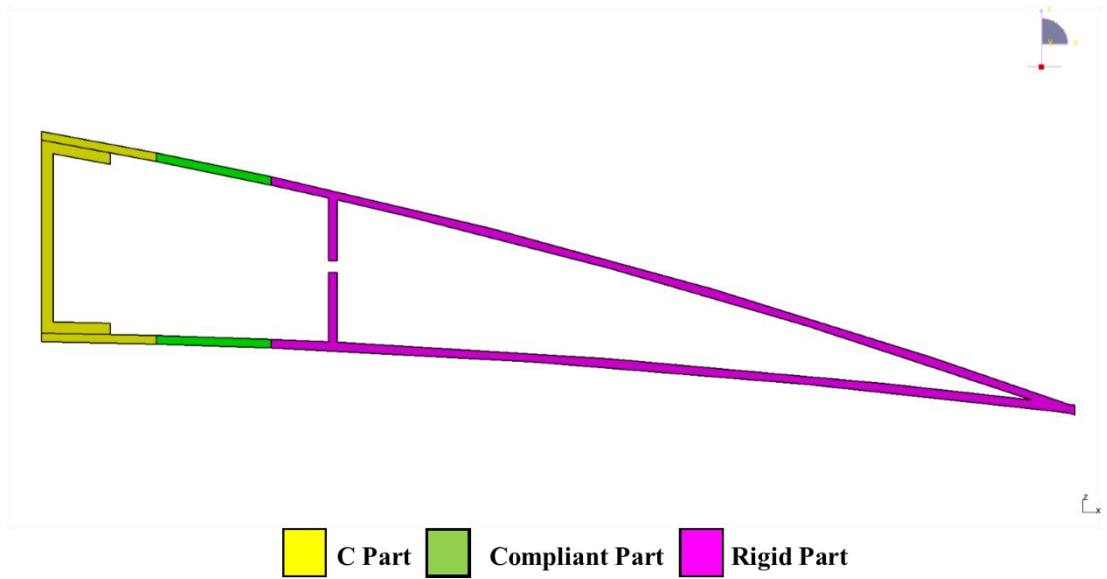


Figure 18: Open Cell Design of the Hybrid Trailing Edge Control Surface

During the design of the open cell both Aluminum and glass-fibre prepreg EHG250-68-37 composite [31] were considered as the materials for the rigid part. The properties of glass-fibre prepreg EHG250-68-37 composite are shown in Table 2.

Table 2: Material Properties of Glass-Fibre Prepreg EHG250-68-37 Composite [31]

Density, $\rho$ :	1900 [kg/m <sup>3</sup> ]
Young's Modulus, $E_{11}$ :	24.5 [GPa]
Young's Modulus, $E_{22}$ :	23.8 [GPa]
Poisson's Ratio, $\nu_{12}$ :	0.11
Shear Modulus, $G_{12}$ :	4.7 [GPa]
Shear Modulus, $G_{13}$ :	3.6 [GPa]
Shear Modulus, $G_{23}$ :	2.6 [GPa]
Ply Thickness:	0.25 [mm]

### 3.4.2 Design of the Closed Cell

In the closed cell design approach, the rigid part of the control surface has no opening at the location of the transmission parts. A typical closed cell design is shown in Figure 19.

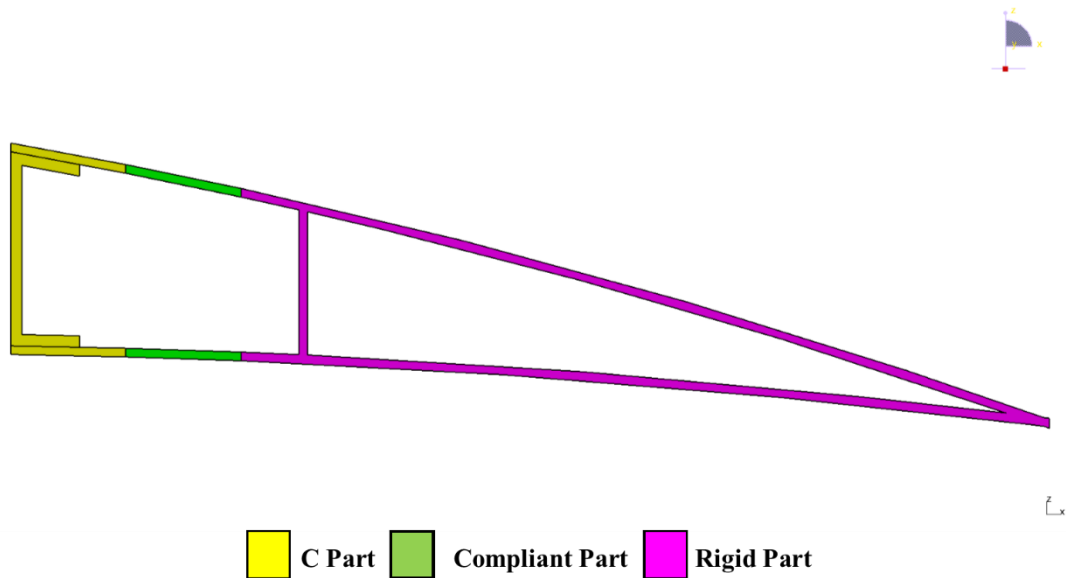


Figure 19: Closed Cell Design of the Hybrid Trailing Edge Control Surface

During the studies only the Glass-fibre prepreg EHG250-68-37 composite was considered for the rigid part. In order to increase the transverse stiffness of the designed control surface, the closed cell was filled with foam. This design is illustrated in Figure 20.

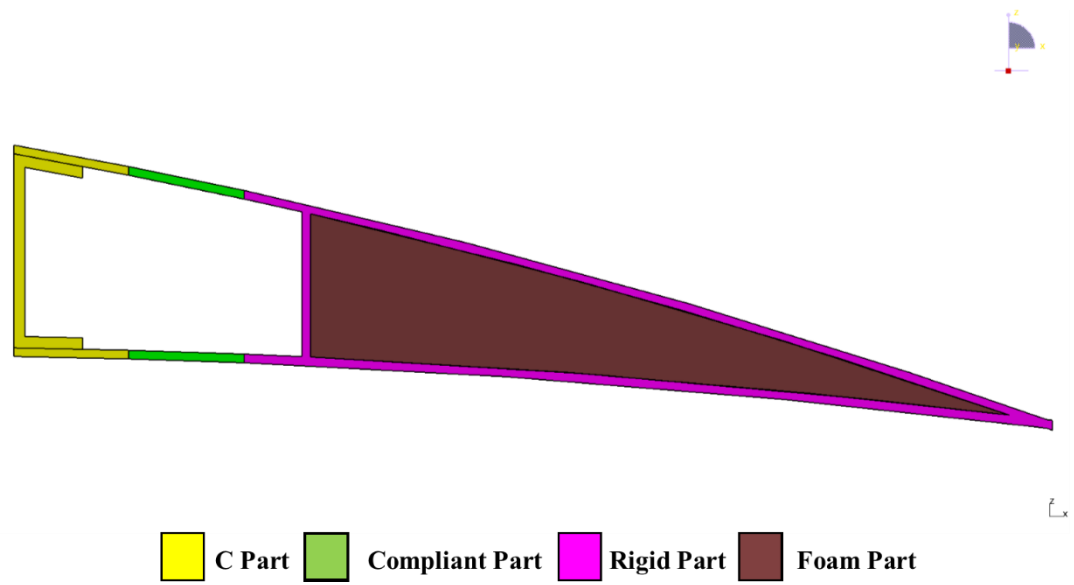


Figure 20: Closed Cell Design of the Hybrid Trailing Edge Control Surface with Foam Included

Rohacell® 51 RIMA [32] was used as the foam material and the properties are given in Table 3.

Table 3: Material Properties of Rohacell® 51 RIMA Foam [32]

Density, $\rho$ :	52 [kg/m <sup>3</sup> ]
Young's Modulus, E:	75 [MPa]
Shear Modulus, G:	24 [MPa]

### 3.5 Utilization of Servo Actuators

#### 3.5.1 Selection of Servo Actuators

The servo actuators which are used in the actuation of the control surface are attached to C part of the control surface. After conducting a research on off-the-shelf servo actuators, Volz DA 13-05-60 servo actuator whose CAD model shown in Figure

21, was found to be the smallest servo actuator which fits into the control surface volume while still providing the required actuation torques. The specifications of Volz DA-13-05-60 servo actuator are given in Table 4.

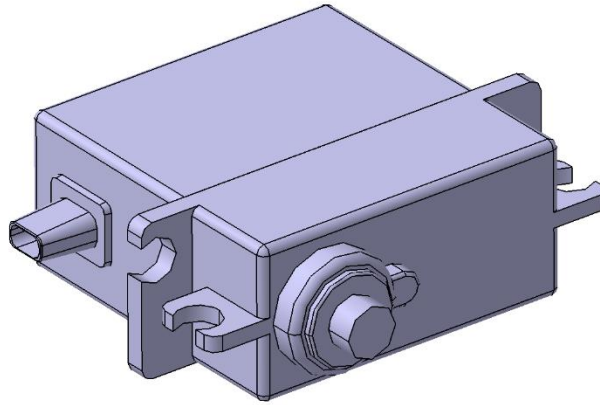


Figure 21: CAD Model of Volz DA 13-05-60 Servo Actuator [33]

Table 4: The Specifications of Volz DA 13-05-60 Servo Actuator [33]

Operating Voltage:	5 [V]
Peak Stall Torque:	600 [N-mm]
Weight:	19 [g]
Dimensions:	28.5 [mm] x 28.5 [mm] x 13 [mm]

When no rotation command is applied to the servo actuator it does not lock itself and the shaft is free to rotate. However, when the necessary rotation command is applied to the actuator, it will hold its position, that is locking itself at the commanded position, provided that the required torque values do not exceed the maximum torque limit of the servo actuator [33].

The servo actuators have built-in moment arms to transmit the generated torque. A typical arm is depicted in Figure 22.



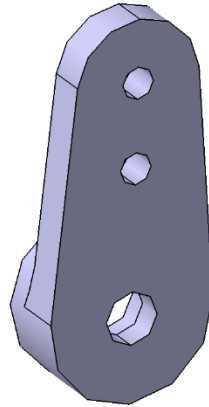


Figure 22: The Built-in Moment Arm of Volz DA 13-05-60 Servo Actuator [33]

In order to maximize the transmission of actuation forces, the lower hole of the built-in moment arm was used. In addition to that the remaining upper portion of the built-in moment arm was assumed to be machined in order to gain some more space. The modified moment arm is shown in Figure 23.

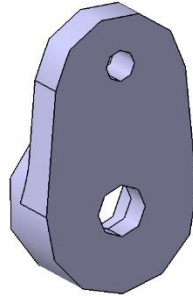


Figure 23: The Modified Moment Arm of Volz DA 13-05-60 Servo Actuator

In order to transmit the generated torque as a linear force to the control surface at the transmission parts; the actuation rods were designed and utilized. A typical actuation rod is shown in Figure 24.

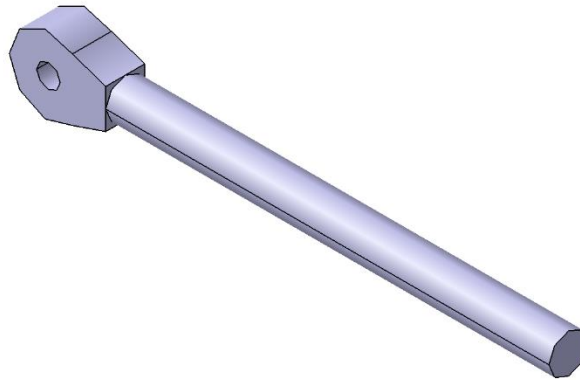


Figure 24: Actuation Rods Designed for Volz DA 13-05-60 Servo Actuator

The actuation rods have circular cross-section with a radius of 1.25 [mm]. The length of the actuation rods is 34.5 [mm], which was obtained from the available space between servo actuator and the transmission parts. The connection between the actuation rods and the modified moment arms are achieved by using pins. These pins transmit all the displacements, and rotations except for the rotation about the pin's axis. Figure 25 illustrates the servo actuator and the actuation rod assembly.

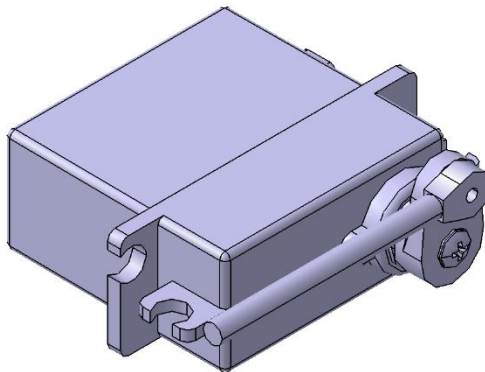


Figure 25: The Assembly of Volz DA 13-05-60 Servo Actuator

### 3.5.2 Connection of Servo Actuators to C Part

In order to connect the servo actuators to the C part of the control surface, an intermediate connection was required. For this purpose, L-shaped fasteners made of Aluminum were designed and used. Figure 26 indicates the L-shaped fastener.

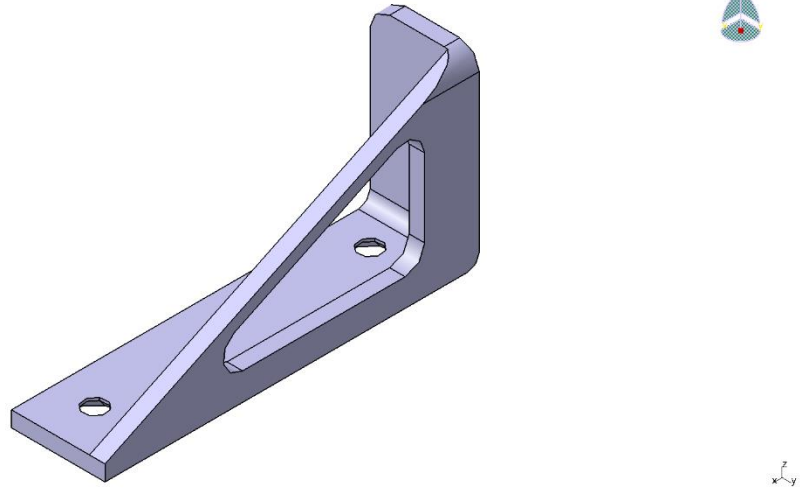


Figure 26: L-Shaped Connection Designed for the Servo Actuators

The fasteners have two M3 countersunk holes at the bottom portion. M3 bolts, nuts and washers were used to connect the servo actuator to the fastener. A typical assembly of the fastener, the servo actuator and the actuation rod is illustrated in Figure 27.

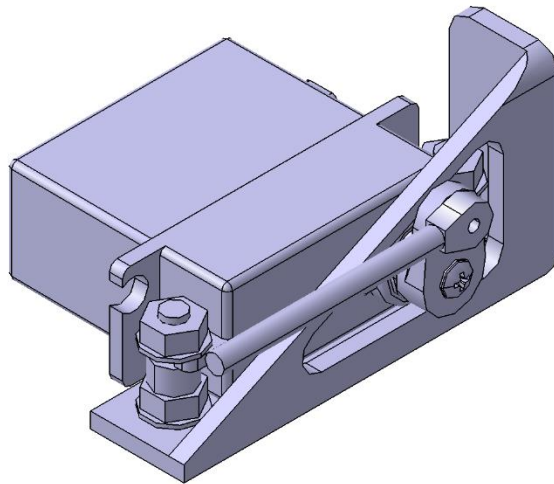


Figure 27: Typical Full Assembly of Volz DA 13-05-60 Servo Actuator with Fastener

L-shaped fasteners are connected to the C part by using super glue. Female guides are opened on the C part to eliminate any possible misalignment during the bonding operation. Figure 28 gives a CAD view of a female guide.

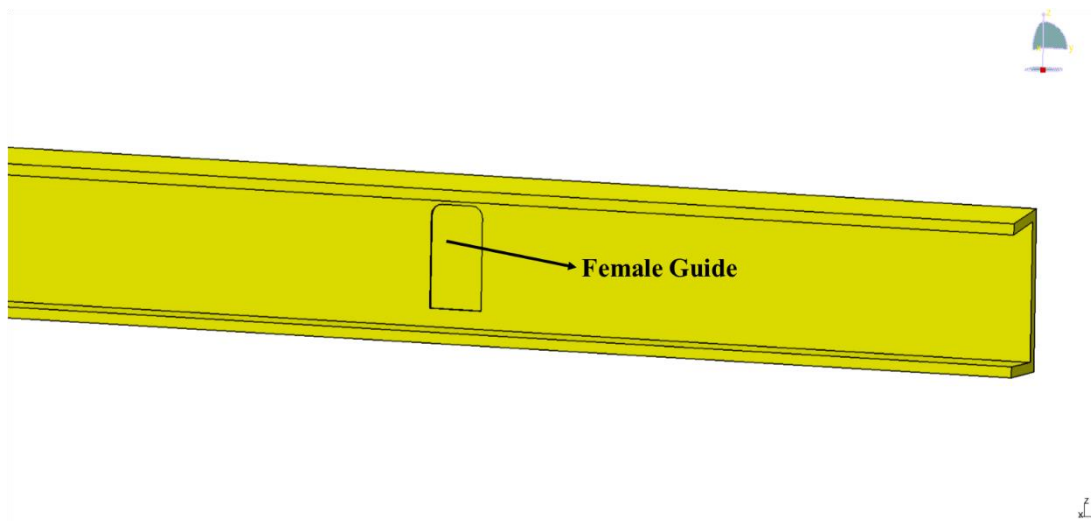


Figure 28: Female Guide on the C Part to Eliminate Misalignment of Bonding of L-Shaped Fasteners

### 3.5.3 Location of the Servo Actuators

In the design, four servo actuators were used to actuate the control surface to achieve camber and decamber. Two of the servo actuators used for actuating the upper portion of the transmission part and two servo actuators utilized for the actuation of the lower portion of the transmission part. The top view of the servo actuators for the open cell case is given in Figure 29. The zoomed view of servo actuators is depicted in Figure 30.

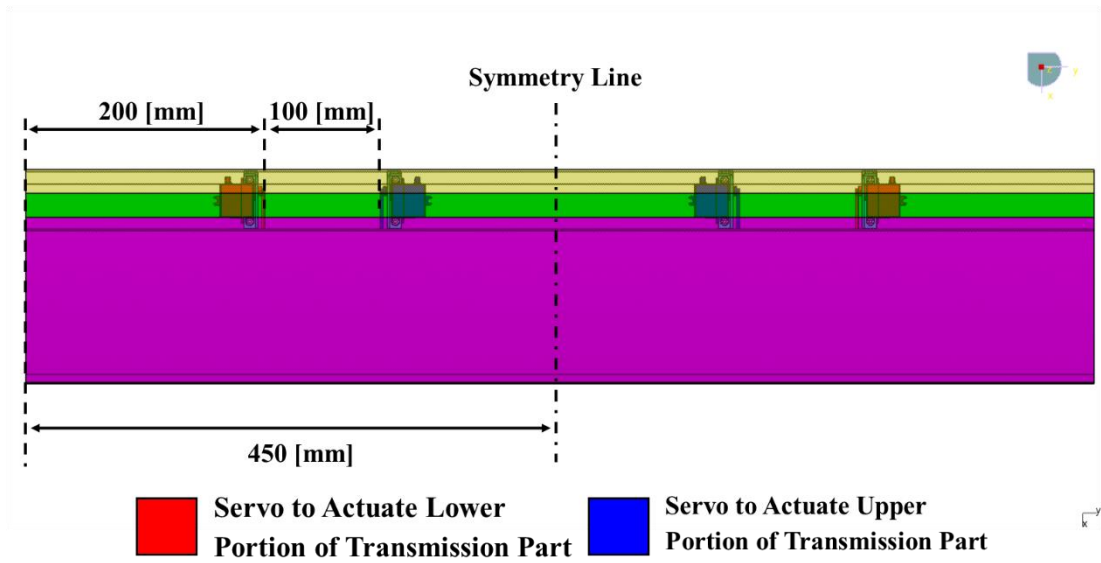


Figure 29: Top View of Servo Actuators in Open Cell Design

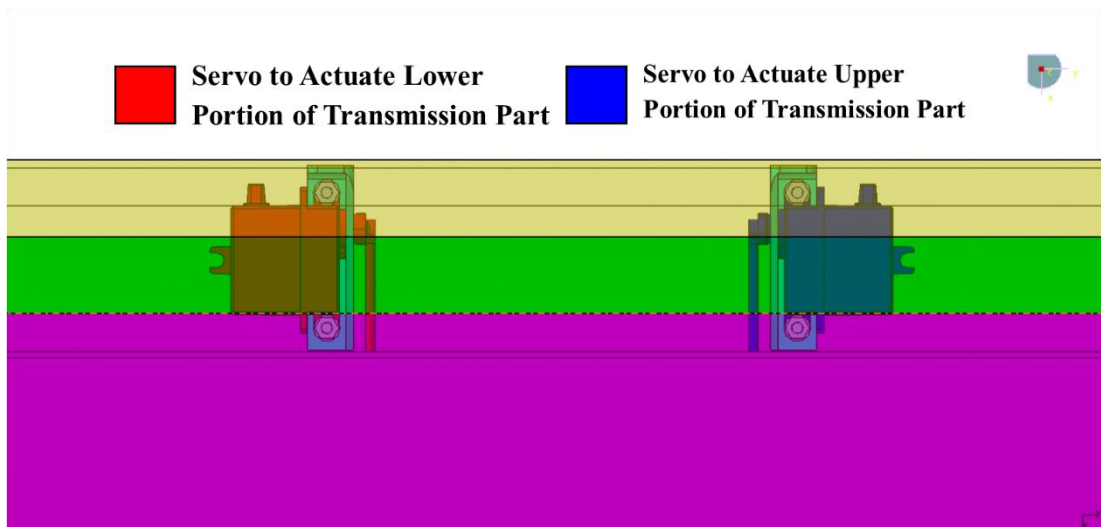


Figure 30: Top View of Servo Actuators in Open Cell Design – Zoomed View

The transverse locations of servo actuators are shown by side view in Figure 31. The location of servo actuators are also the same for the closed cell design.

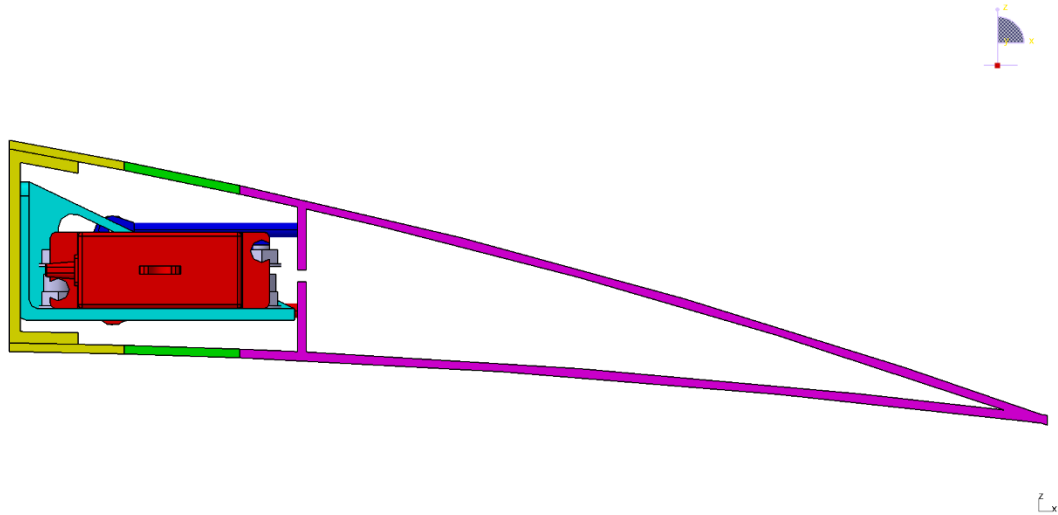


Figure 31: Side View of Open Cell Design along with Servo Actuators and Fasteners

### 3.6 Discussion and Conclusion

In this chapter the design of the hybrid trailing edge control surface is achieved. Various parts of the hybrid trailing edge control surface and designs are explained and illustrated. The deflection mechanisms of the control surface, the required servo actuators and their locations are indicated.

In the following chapters, the geometric properties of the control surface and spanwise location of servo actuators will be varied and studied in order to achieve an optimum design.

## **CHAPTER 4**

### **FINITE ELEMENT ANALYSIS OF THE HYBRID TRAILING EDGE CONTROL SURFACE IN IN-VACUO CONDITION**

#### **4.1 Introduction**

In this chapter, the hybrid trailing edge control surface is structurally analyzed in in-vacuo condition by Finite Element Method using Static Structural module of ANSYS Workbench v14.0 package software.

The first part of the chapter is dedicated to Finite Element Analysis of open cell design. Initially, camber and decamber variations are investigated. Then, material, geometric and servo actuator variations are taken into account. Finally, twist of the control surface is assessed.

The second part of the chapter consists of Finite Element Analysis of closed cell design. Camber and decamber variations are also studied.

Finally, some conclusions are drawn from the results of Finite Element Analyses.

#### **4.2 Finite Element Analysis of Open Cell Design in in-Vacuo Condition**

In this section, Finite Element Analysis of open cell design is presented. Initially, the solid model is illustrated with relevant dimensions. Then, the procedure of Finite Element Model is explained and results are presented.

The solid model of open cell design is presented in Chapter 3. Relevant dimensions of open cell design are depicted in Figure 32.

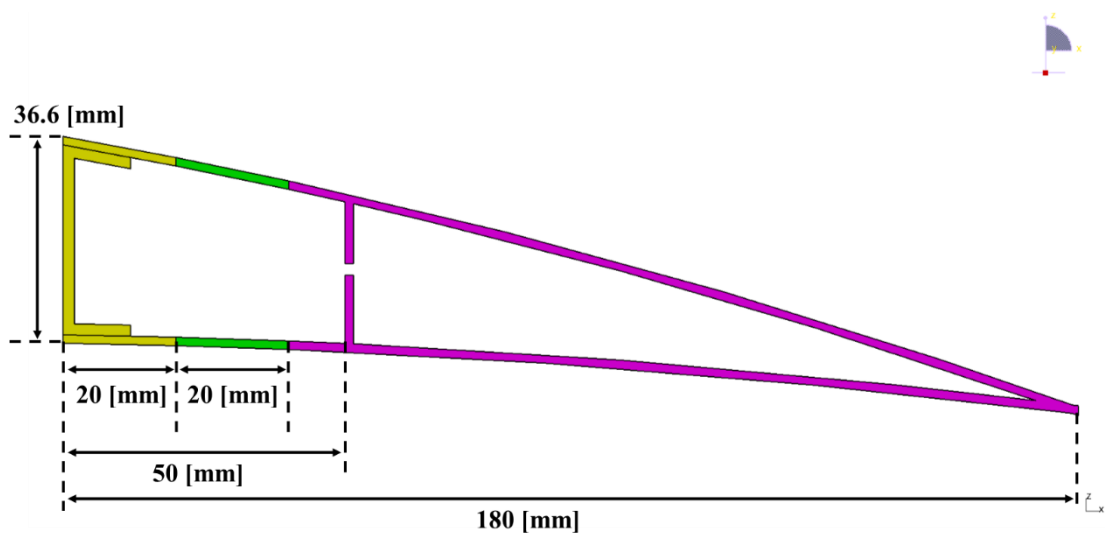


Figure 32: Side View of Open Cell Design with Dimensions

The rigid part, compliant part and the skin parts of the C part have a uniform thickness of 1.5 [mm]. The dimensions of the C bar are illustrated in Figure 33. The C bar has a uniform thickness of 2 [mm].

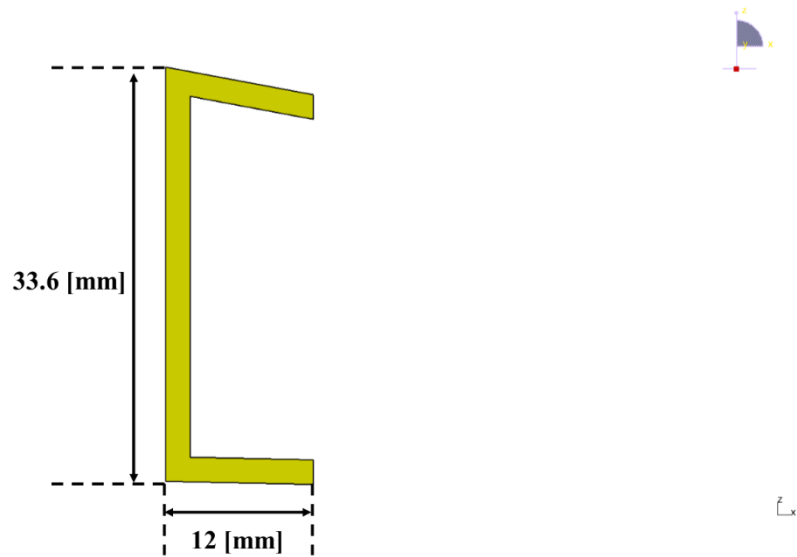


Figure 33: Side View of C Bar with Dimensions



#### 4.2.1 Finite Element Modelling of Open Cell Design

Finite Element Model of open cell design was generated by Static Structural Module of ANSYS Workbench v14.0 package software. The generated geometry for Finite Element Model is shown in Figure 34.

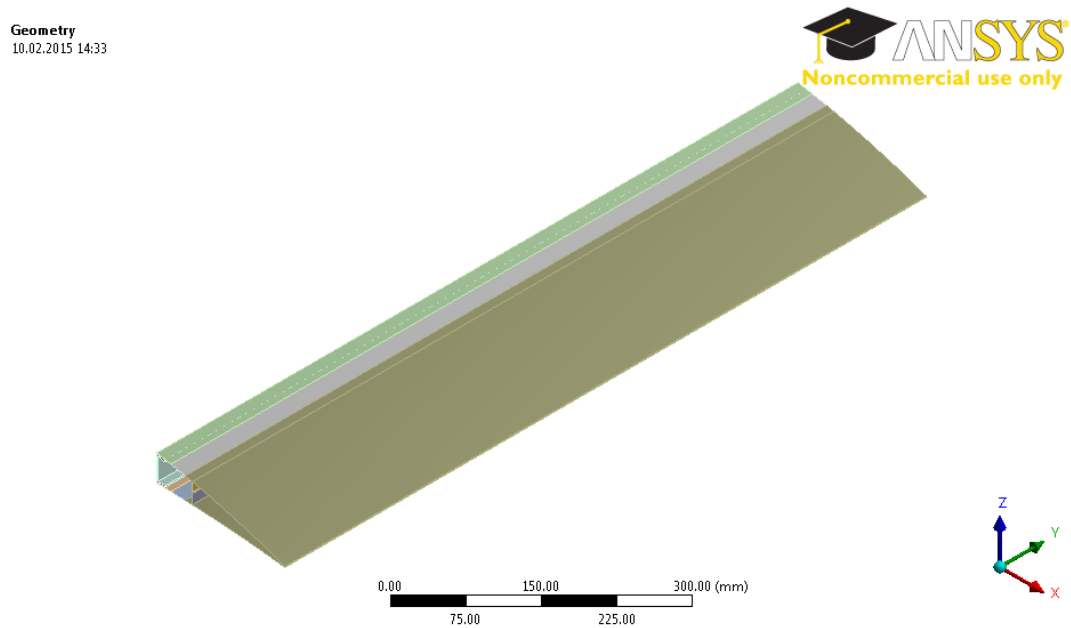


Figure 34: The Generated Geometry of Open Cell Design for Finite Element Model

The rigid part, the compliant part and the skin parts of the C part were modelled as surface bodies. Then, uniform quadrilateral SHELL181 elements [34], which are 4-noded first order shell elements, were assigned to these bodies with 1.5 [mm] thickness. The skin parts of the C part and the compliant part were modelled with 10 [mm] element size. The skin of the rigid part was modelled with 30 [mm] element size while transmission parts were modelled with 10 [mm] element size. The defined element sizes were based on a mesh convergence study and the results are depicted in Figure 35 and Figure 36.

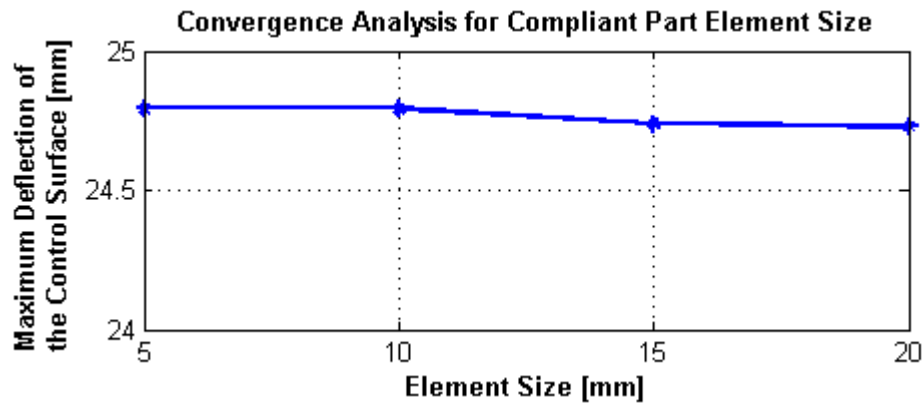


Figure 35: Mesh Convergence Analysis for Compliant Part Element Size [35]

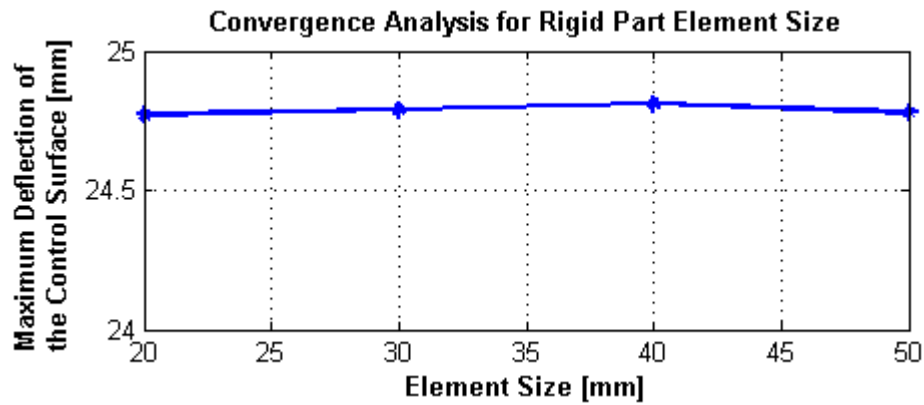


Figure 36: Mesh Convergence Analysis for Rigid Part Element Size [35]

The C bar part was modelled as a solid body. Therefore, 8-noded first order solid elements, SOLID185 [34], were assigned to the body. The element size was decided to be 5 [mm].

The moment arms and the actuation rods were modelled as line bodies. 2-noded first order BEAM188 elements [34] were assigned to these bodies. Rectangular cross section with dimensions of 7.4 [mm] x 1.9 [mm] was assigned to the moment arms. For the actuation rods, circular cross-section was assigned with a radius of 1.25 [mm].

In Finite Element Model, servo actuators and their fixations were not modelled. Two different views of the generated mesh are shown in Figure 37 and Figure 38.

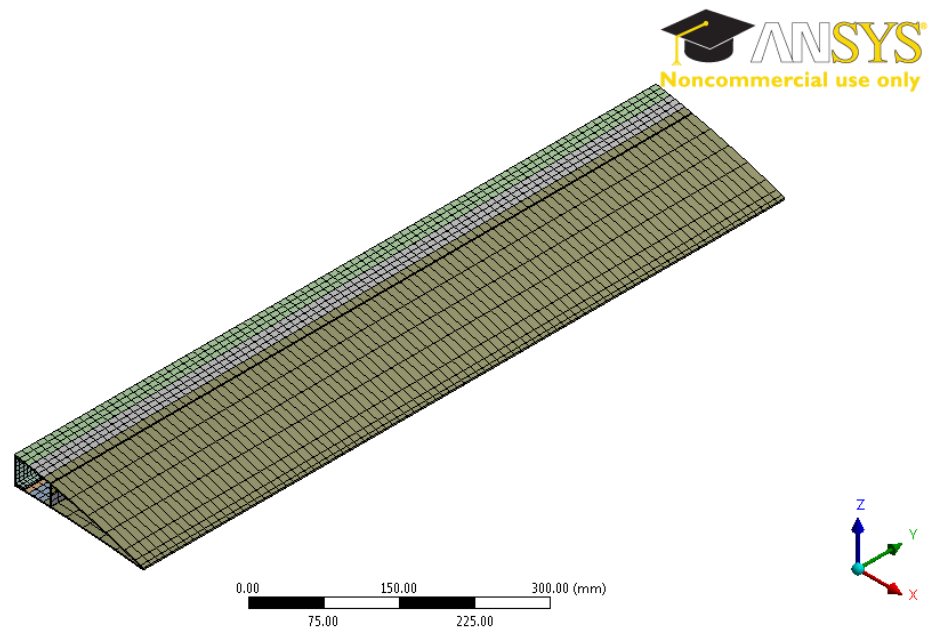


Figure 37: Isometric View of Generated Mesh for Open Cell Design

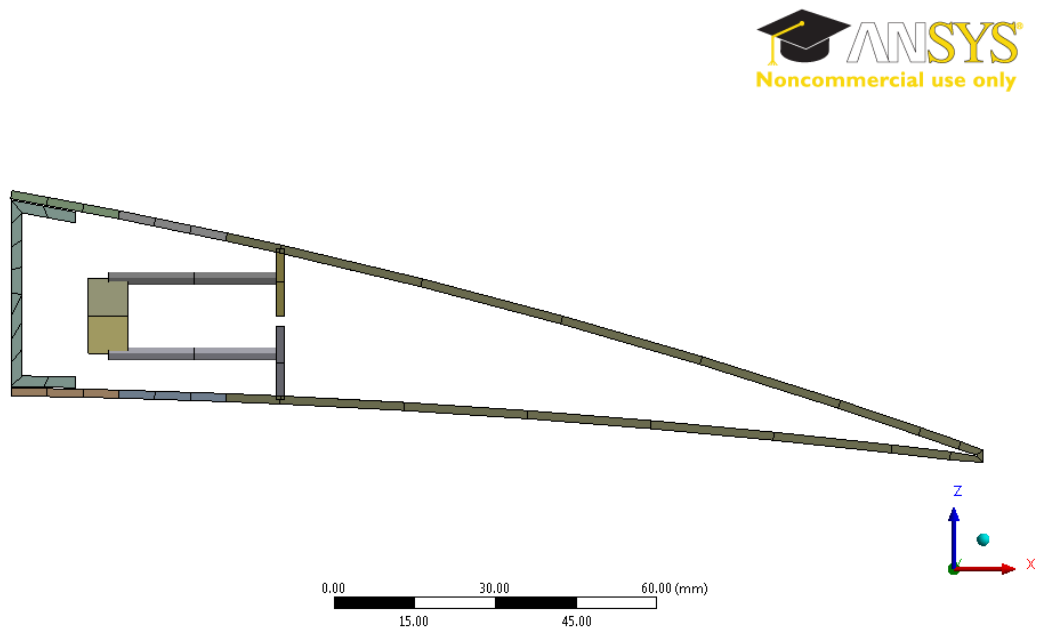


Figure 38: Side View of the Generated Mesh for Open Cell Design

Meshed view of moment arms and actuation rods with assigned cross-section properties are shown in Figure 39.

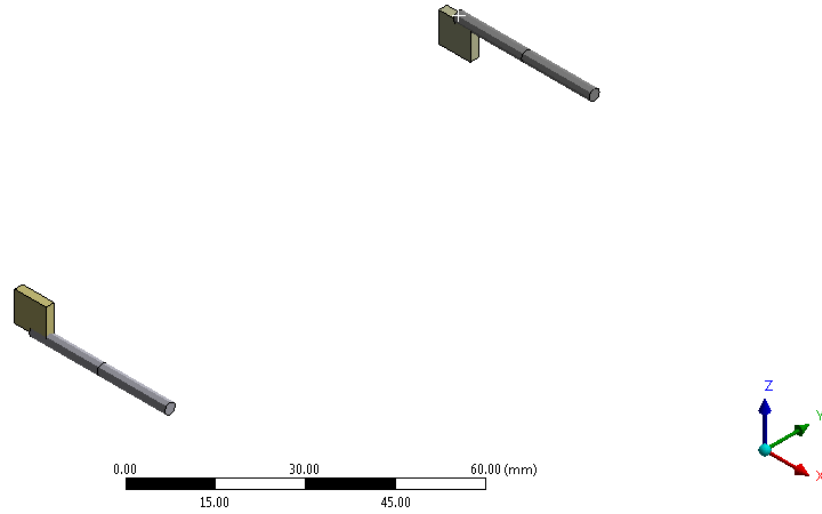


Figure 39: Meshed View of Moment Arms and Actuation Rods with Assigned Cross-Section Properties

In Chapter 3, it is mentioned that the compliant part is rigidly attached to the rigid part and the C part. In order to create such a connection, “Bonded Contact” was defined on the coinciding edges of compliant part, rigid part and skin parts of C part. These coinciding edges are shown in Figure 40.

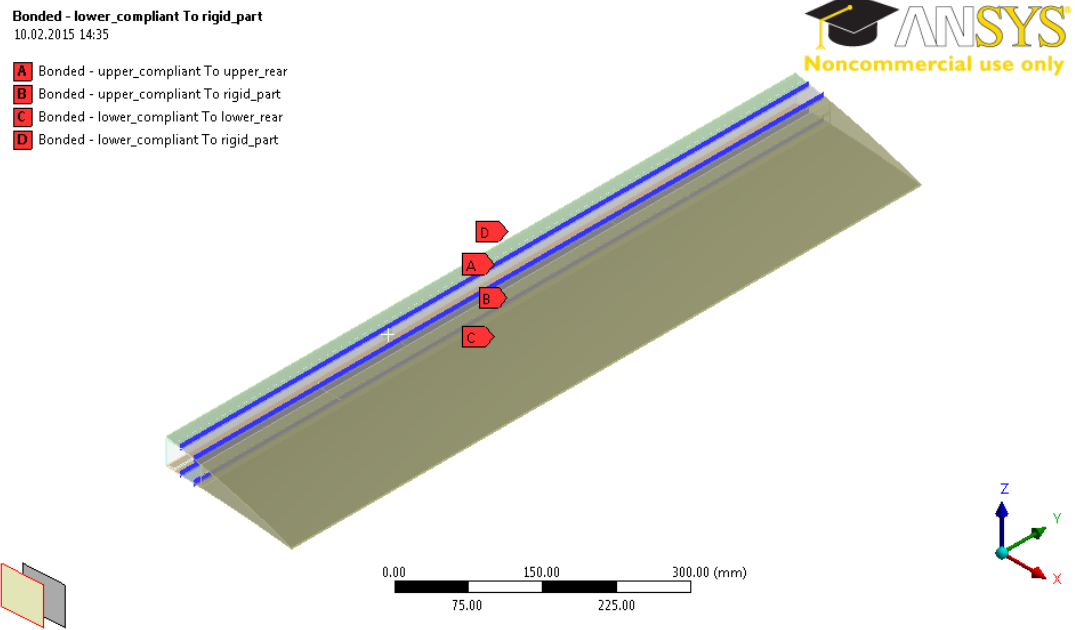


Figure 40: Coinciding Edges of Compliant Part, Rigid Part and Skin Parts of C Part

The actuation rods are also rigidly attached to the transmission parts. In order to model this, “Bonded Contact” was also defined between vertices of the actuation rods and the transmission parts. The generated connections are illustrated in Figure 41.

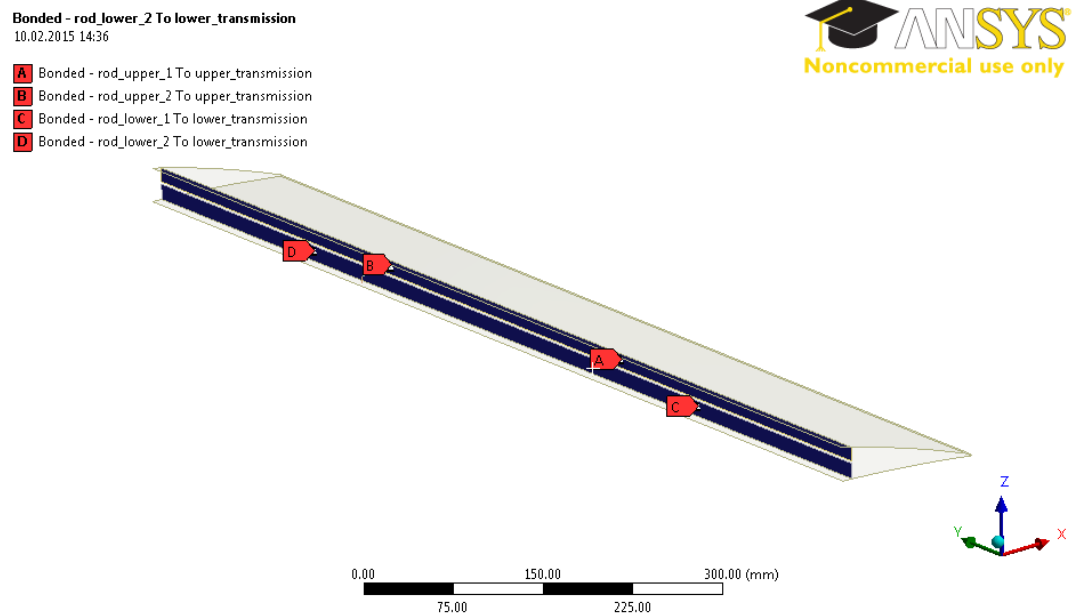


Figure 41: Connection of Actuation Rods to Transmission Parts in Open Cell Design

Finally, the connection between skin parts of the C part and the C bar was also generated by “Bonded Contact”.

The coinciding edges and faces of the different parts could have been connected by the glued elements. However, this process requires the application of similar mesh sizes between the parts. But, in the current model, the parts were meshed with different element sizes, which is the results of mesh convergence analysis. Since “Bonded Contact” property does not require parts to be connected to have similar mesh sizes, all the necessary connections in the model were done by “Bonded Contact”.

As mentioned in Chapter 3, moment arms and actuation rods are connected by pins. This pinned joint was modelled by coupling all displacements and rotations except for rotation about y axis at coinciding nodes of moment arms and actuation rods. The coinciding nodes are depicted in Figure 42.

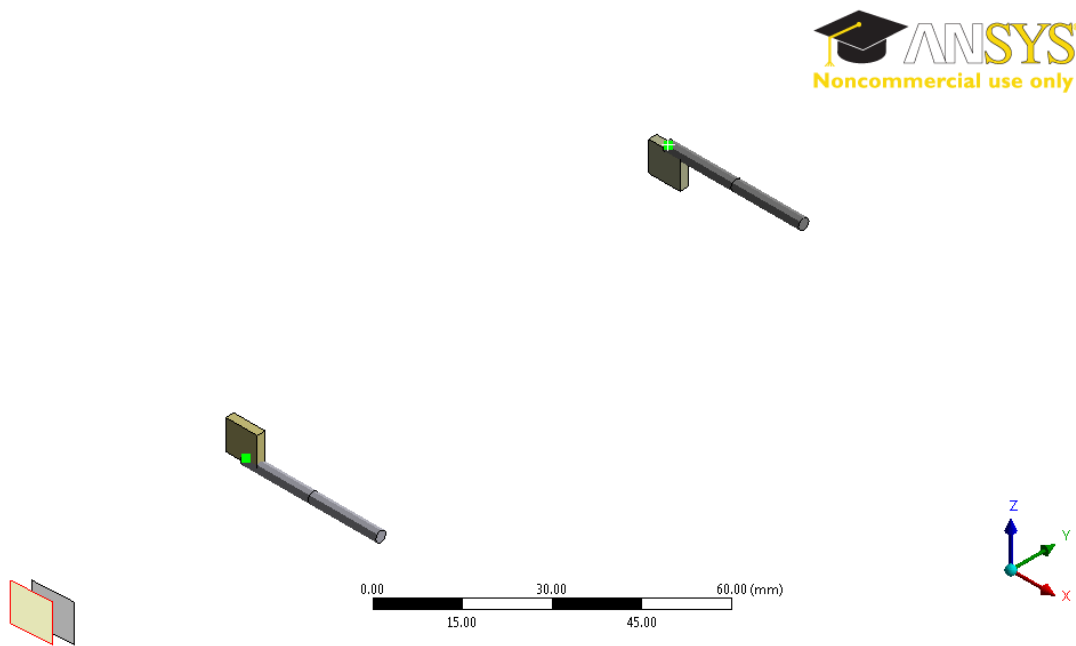


Figure 42: Coinciding Nodes of Moment Arms and Actuation Rods

The leading edge part of the C bar was fixed in all displacement and rotations to accommodate the rigid connection between C bar and the wing, and shown in Figure 43.

F: Aluminum - 2+2 - Open Cell - NACA9510  
Fixed Support  
Time: 1. s  
10.02.2015 14:36



Fixed Support

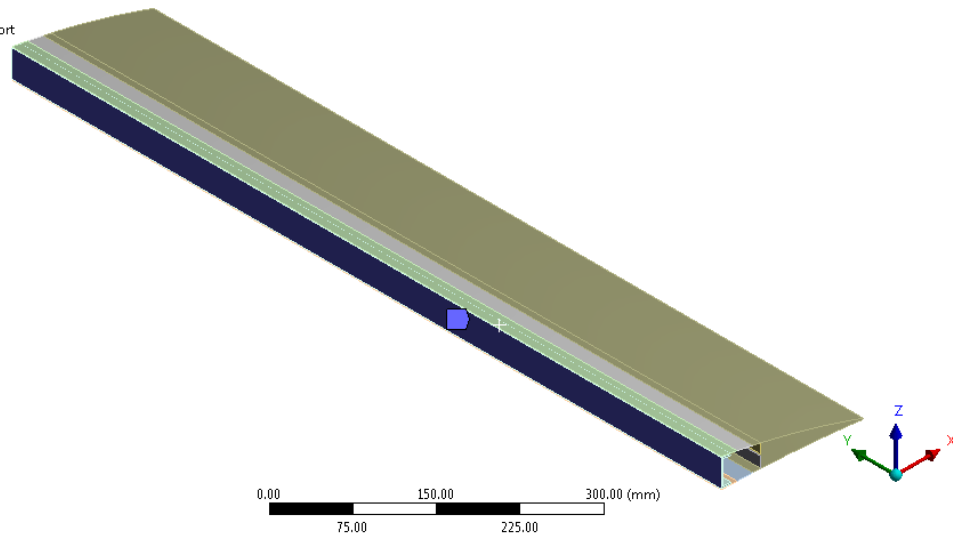


Figure 43: Boundary Condition Applied to the Leading Edge of the C Bar

The connection vertices of moment arms to servo actuators were fixed in all displacements and rotations except for the rotation about y axis. The rotations about y axis were prescribed to model the actuation generated by servos. These prescribed values are given in the following sections.

Finally, standard earth gravity was applied to the system to take into account of weight effects.

#### 4.2.2 Analysis of Camber and Decamber Variations of Open Cell Design

The camber and decamber variations are presented in this section. Aluminum was used as the material of the rigid part in these analyses.

Initially, a linear solution was performed, then a non-linear solution was used with only geometric non-linearities. Finally, a non-linear solution with both material and geometric non-linearities was conducted. The obtained differences between the three approaches are presented.

#### 4.2.2.1 Camber Variations of Open Cell Design – Linear Case

It was mentioned in Chapter 3 that the main working principle of compliant part is always to have tension. Therefore, by using Neoprene Rubber data given in Figure 17, the initial elastic modulus of the curve was determined and “Linear Isotropic Elasticity” material model was based on that value. Since the Neoprene Rubber is a compliant material a value of approximately 0.49 was assigned for the Poisson’s ratio in order not to encounter a mathematical instability during the calculations. The linearized Neoprene Rubber material parameters are provided in Table 5.

Table 5: Linearized Material Properties of Neoprene Rubber using Isotropic Linear Elasticity Model

Density, $\rho$ :	1250 [kg/m <sup>3</sup> ]
Young’s Modulus, $E$ :	80 [kPa]
Poisson’s Ratio, $\nu$ :	0.49

To increase the camber of the control surface, approximately 15.2 [mm] downward tip deflection was tried to be achieved. Therefore, 21.5 [deg] rotation about y axis was prescribed for moment arms of servo actuators to drive the upper portion of transmission parts, and -12 [deg] rotation about y axis was prescribed for moment arms of servo actuators to drive the lower portion of transmission parts as boundary conditions.

Transverse displacement contours are shown in Figure 44. von-Mises strain distribution contours are depicted in Figure 45. The combined beam stresses, which is a combination of axial and bending stresses in beam elements are shown in Figure 46.



**Directional Deformation**  
 Type: Directional Deformation(Z Axis)  
 Unit: mm  
 Global Coordinate System  
 Time: 1  
 11.02.2015 09:47

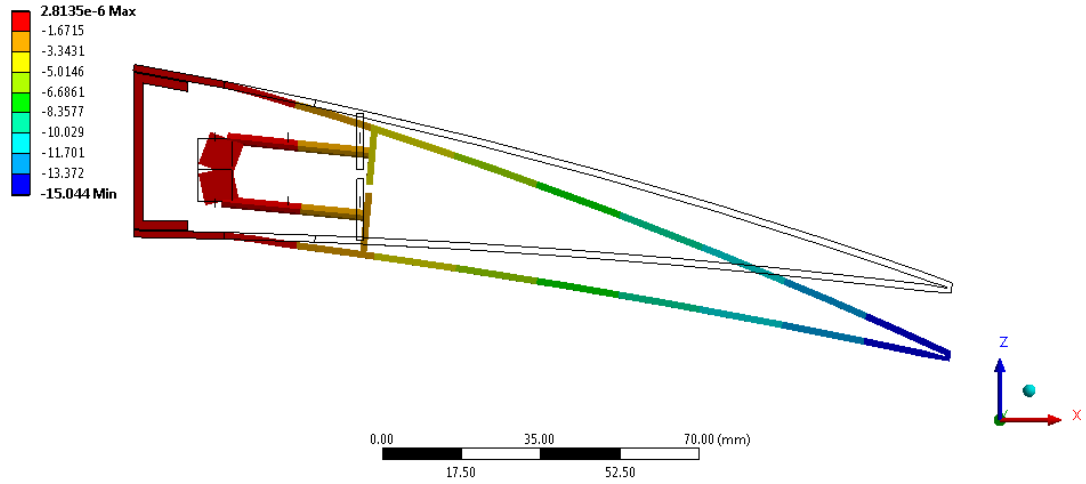


Figure 44: Transverse Displacement Contours for 15.2 [mm] Camber of Open Cell Design – Linear Case – Maximum 15.044 [mm]

**Equivalent Elastic Strain**  
 Type: Equivalent Elastic Strain - Top/Bottom - Layer 0  
 Unit: mm/mm  
 Time: 1  
 11.02.2015 09:47

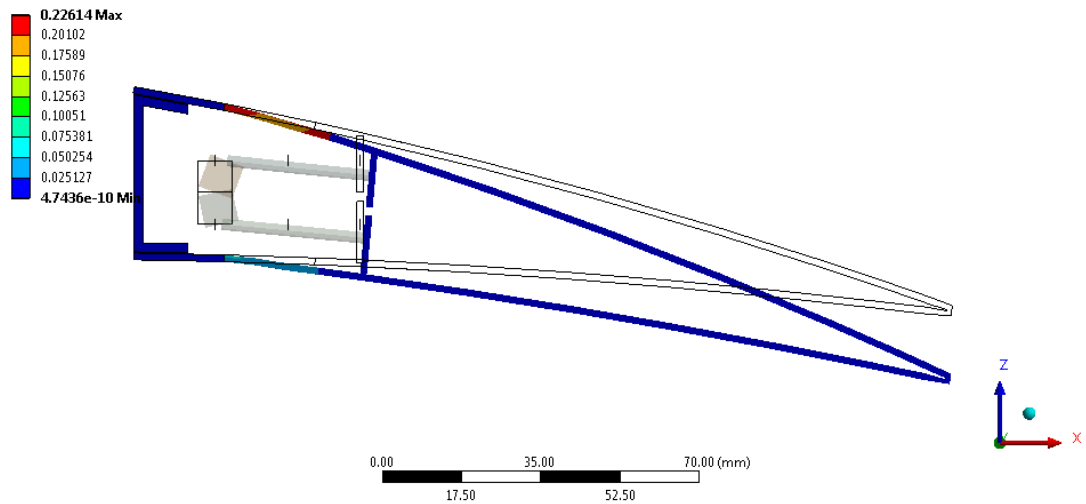


Figure 45: von-Mises Strain Distribution Contours for 15.2 [mm] Camber of Open Cell Design – Linear Case – Maximum 0.226 [mm/mm]

**Maximum Combined Stress**  
 Type: Maximum Combined Stress - Top/Bottom - Layer 0  
 Unit: MPa  
 Time: 1  
 11.02.2015 09:47

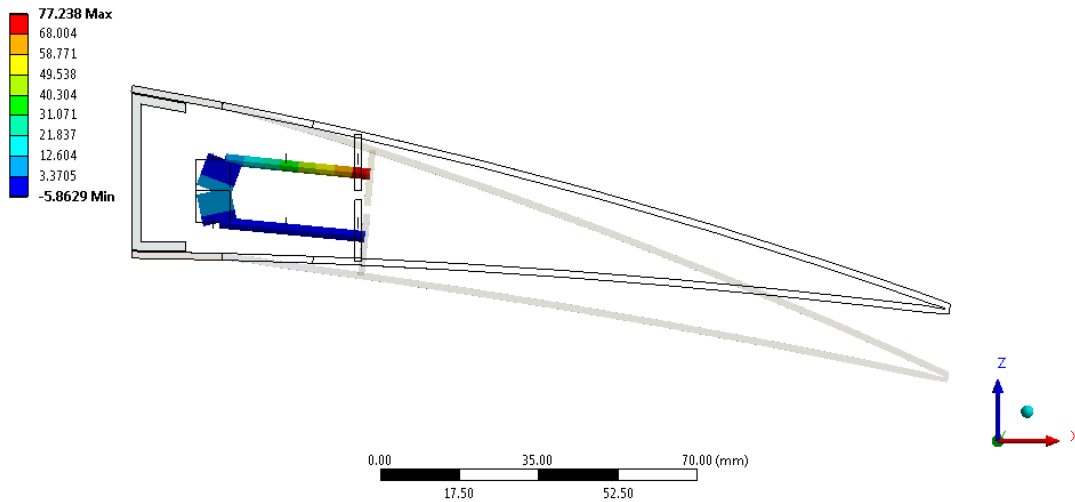


Figure 46: The Combined Beam Stresses for 15.2 [mm] Camber of Open Cell Design  
 – Linear Case – Maximum 77.238 [MPa]

The resulting reaction moments at moment arms are -96 [N-mm] per servo to actuate the upper portion of the transmission part, -203 [N-mm] per servo to actuate the lower portion of the transmission part. These values are below the maximum torque limit of selected servo actuator.

#### 4.2.2.2 Camber Variations of Open Cell Design – Non-linear Case with Only Geometric Non-linearities

To increase the camber of the control surface, approximately 15.2 [mm] downward tip deflection was tried to be achieved. Therefore, 21 [deg] rotation about y axis was prescribed for the moment arms of servo actuators to drive the upper portion of transmission parts, and -12 [deg] rotation about y axis was prescribed for moment arms of servo actuators to drive the lower portion of the transmission parts as boundary conditions. Transverse displacement contours are shown in Figure 47. von-Mises strain distribution contours are shown in Figure 48. The combined beam stresses are shown in Figure 49.

K: Aluminum - 2+2 - Open Cell - NACA9510 - Initial - NL  
 Directional Deformation  
 Type: Directional Deformation(Z Axis)  
 Unit: mm  
 Global Coordinate System  
 Time: 1  
 16.02.2015 19:51

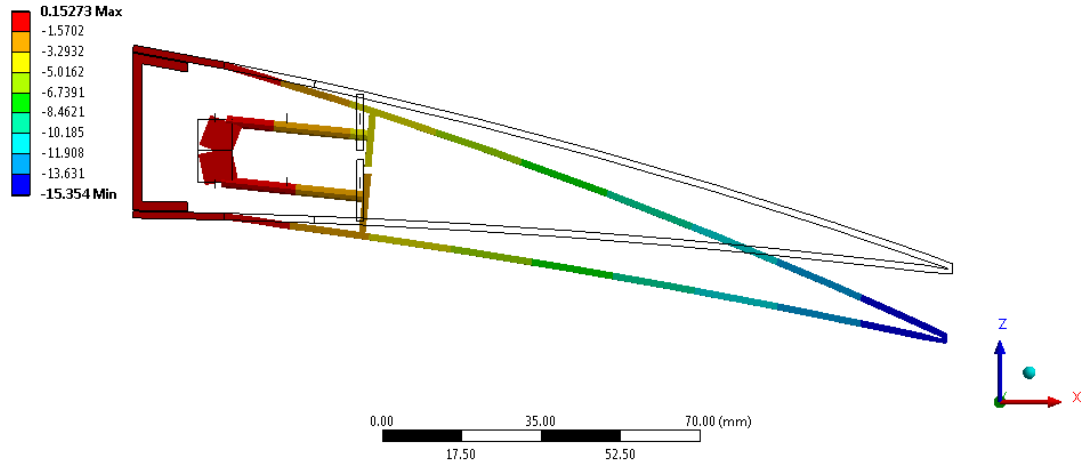


Figure 47: Transverse Displacement Contours for 15.2 [mm] Camber of Open Cell Design – Non-linear Case with Only Geometric Non-linearities – Maximum 15.354 [mm]

K: Aluminum - 2+2 - Open Cell - NACA9510 - Initial - NL  
 Equivalent Elastic Strain  
 Type: Equivalent Elastic Strain - Top/Bottom - Layer 0  
 Unit: mm/mm  
 Time: 1  
 16.02.2015 19:52

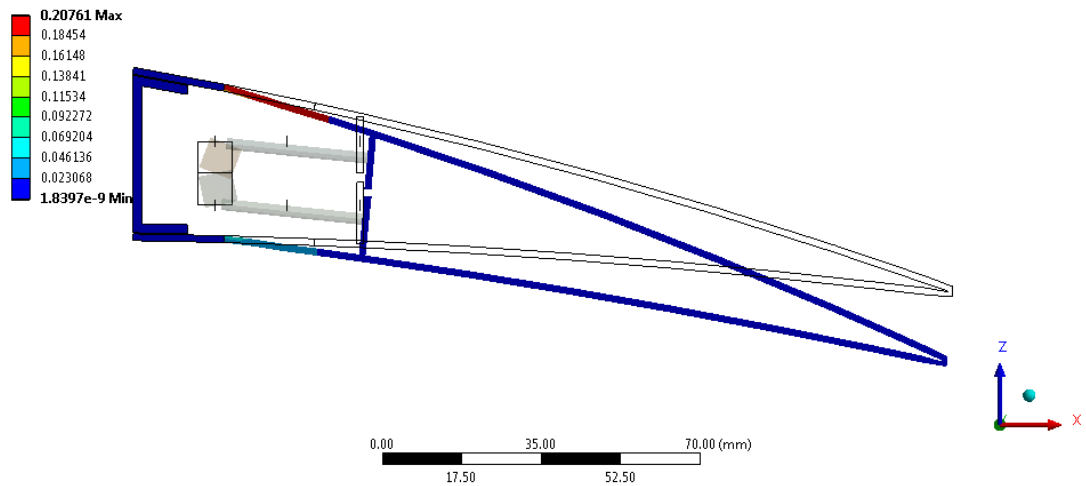


Figure 48: von-Mises Strain Distribution Contours for 15.2 [mm] Camber of Open Cell Design – Non-linear Case with Only Geometric Non-linearities – Maximum 0.208 [mm/mm]

K: Aluminum - 2+2 - Open Cell - NACA9510 - Initial - NL  
Maximum Combined Stress  
Type: Maximum Combined Stress - Top/Bottom - Layer 0  
Unit: MPa  
Time: 1  
16.02.2015 19:52

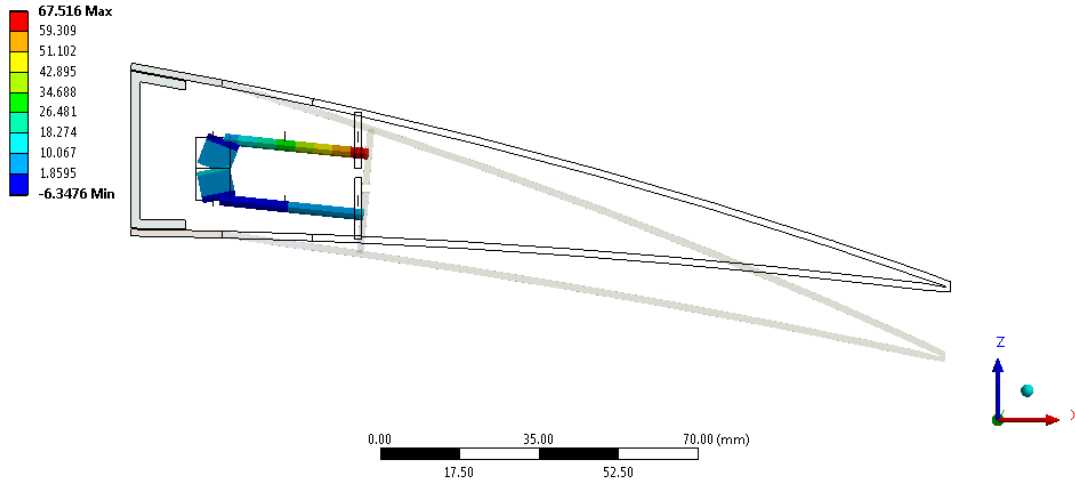


Figure 49: The Combined Beam Stresses for 15.2 [mm] Camber of Open Cell Design – Non-linear Case with Only Geometric Non-linearities – Maximum 67.516 [MPa]

The resulting reaction moments at moment arms are -141 [N-mm] per servo to actuate the upper portion of the transmission part, -213 [N-mm] per servo to actuate the lower portion of the transmission part. These values are below the maximum torque limit of selected servo actuator.

#### 4.2.2.3 Camber Variations of Open Cell Design – Non-linear Case with Geometric and Material Non-linearities

To increase the camber of the control surface, approximately 15.2 [mm] downward tip deflection was tried to be achieved. Therefore, 21 [deg] rotation about y axis was prescribed for moment arms of servo actuators to drive the upper portion of transmission parts, and -12 [deg] rotation about y axis was prescribed for moment arms of servo actuators to drive the lower portion of transmission parts as boundary conditions. Transverse displacement contours are shown in Figure 50. von-Mises strain distribution contours are shown in Figure 51.

**Directional Deformation**  
 Type: Directional Deformation(Z Axis)  
 Unit: mm  
 Global Coordinate System  
 Time: 1  
 10.02.2015 14:57

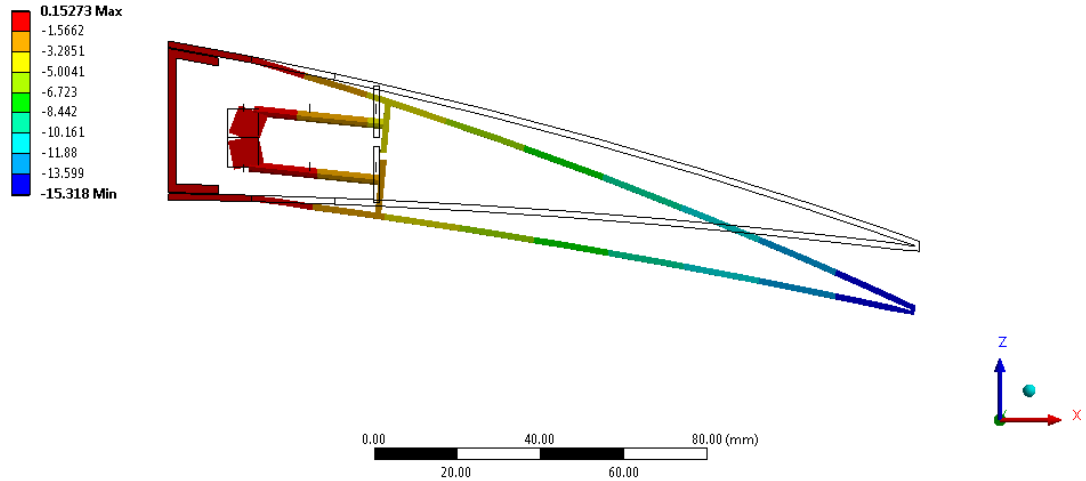


Figure 50: Transverse Displacement Contours for 15.2 [mm] Camber of Open Cell Design – Non-linear Case with Geometric and Material Non-linearities – Maximum 15.318 [mm]

**Equivalent Elastic Strain**  
 Type: Equivalent Elastic Strain - Top/Bottom - Layer 0  
 Unit: mm/mm  
 Time: 1  
 10.02.2015 14:57

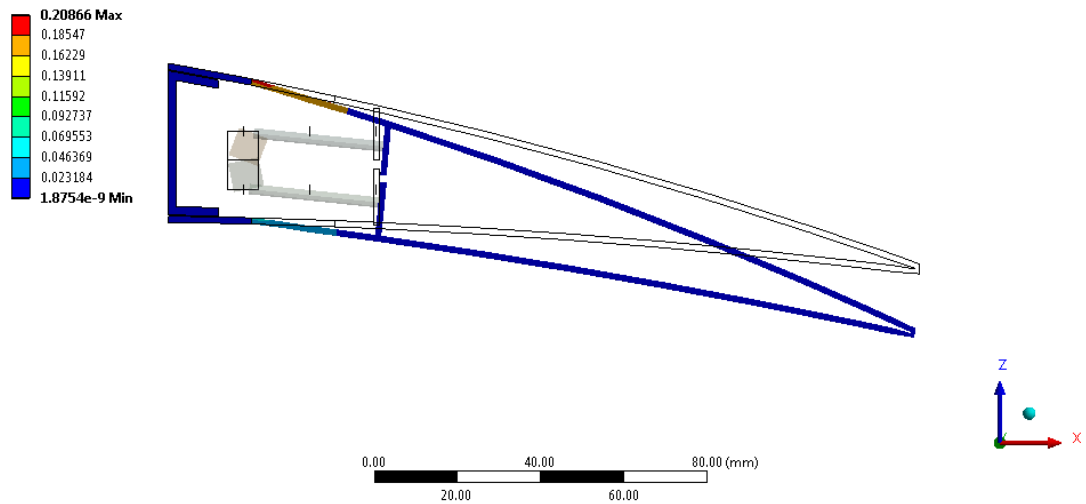


Figure 51: von-Mises Strain Distribution Contours for 15.2 [mm] Camber of Open Cell Design – Non-linear Case with Geometric and Material Non-linearities – Maximum 0.209 [mm/mm]

It can be seen from figure that the C part and the rigid part have negligible strains. In other words, they exhibit a rigid body behavior. The major source of strains occurring in the system is due to the stretching of compliant parts.

The combined beam stresses, which is a combination of axial and bending stresses in beam elements are shown in Figure 52.

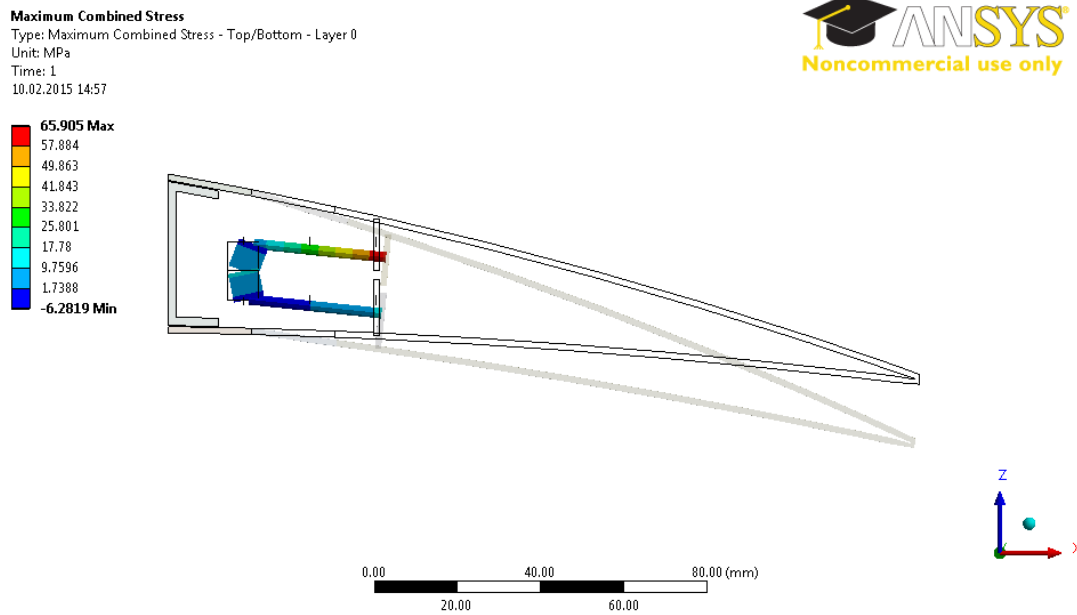


Figure 52: The Combined Beam Stresses for 15.2 [mm] Camber of Open Cell Design – Non-linear Case with Geometric and Material Non-linearities – Maximum 65.905 [MPa]

The resulting reaction moments at moment arms are -136 [N-mm] per servo to actuate the upper portion of the transmission part, -211 [N-mm] per servo to actuate the lower portion of the transmission part. These values are below the maximum torque limit of selected servo actuator.

#### 4.2.2.4 Decamber Variations of Open Cell Design – Linear Case

In order to perform decamber, approximately 15.2 [mm] and 20.2 [mm] upward deflection of the tip of the control surface was tried to be achieved.

For 15.2 [mm] upward deflection, 12 [deg] rotation about y axis was prescribed for moment arms of servo actuators to drive the upper portion of transmission parts, and -25 [deg] rotation about y axis was prescribed for moment arms of servo actuators to drive the lower portion of transmission parts as boundary conditions. Transverse displacement contours are shown in Figure 53. von-Mises strain distribution contours are depicted in Figure 54. The combined beam stresses are shown in Figure 55.

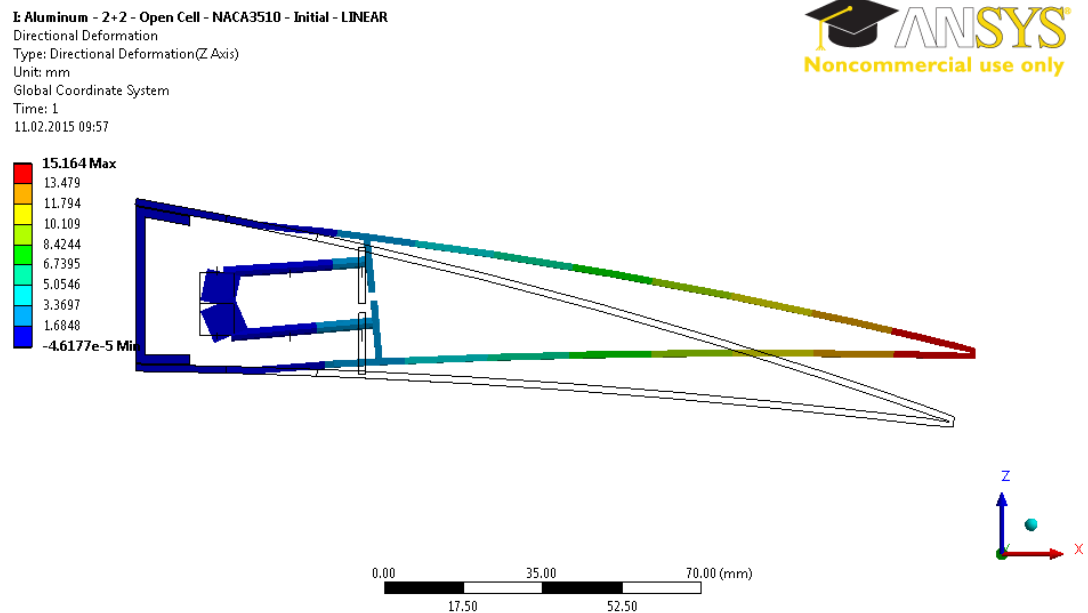


Figure 53: Transverse Displacement Contours for 15.2 [mm] Decamber of Open Cell Design – Linear Case – Maximum 15.164 [mm]

E Aluminum - 2+2 - Open Cell - NACA3510 - Initial - LINEAR  
 Equivalent Elastic Strain  
 Type: Equivalent Elastic Strain - Top/Bottom - Layer 0  
 Unit: mm/mm  
 Time: 1  
 11.02.2015 09:57

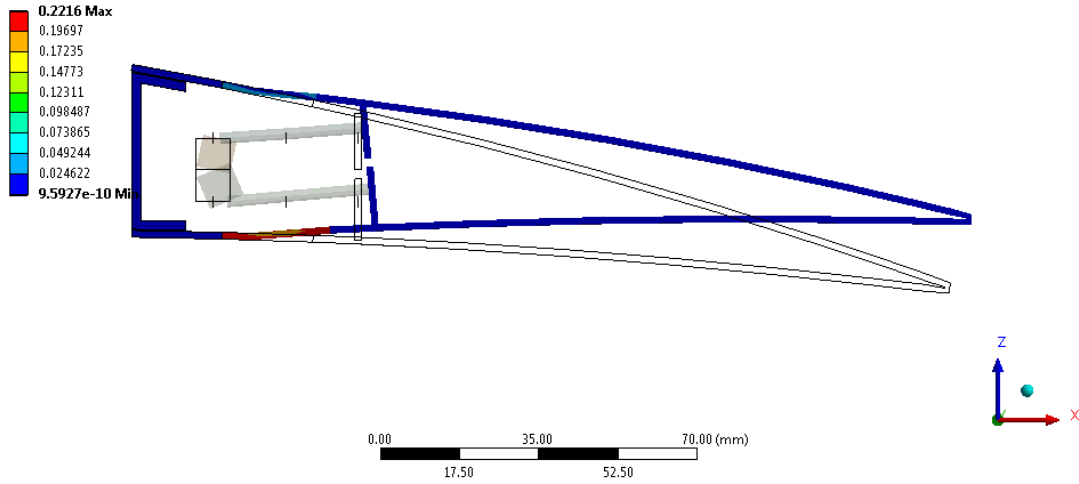


Figure 54: von-Mises Strain Distribution Contours for 15.2 [mm] Decamber of Open Cell Design – Linear Case – Maximum 0.222 [mm/mm]

E Aluminum - 2+2 - Open Cell - NACA3510 - Initial - LINEAR  
 Maximum Combined Stress  
 Type: Maximum Combined Stress - Top/Bottom - Layer 0  
 Unit: MPa  
 Time: 1  
 11.02.2015 09:57

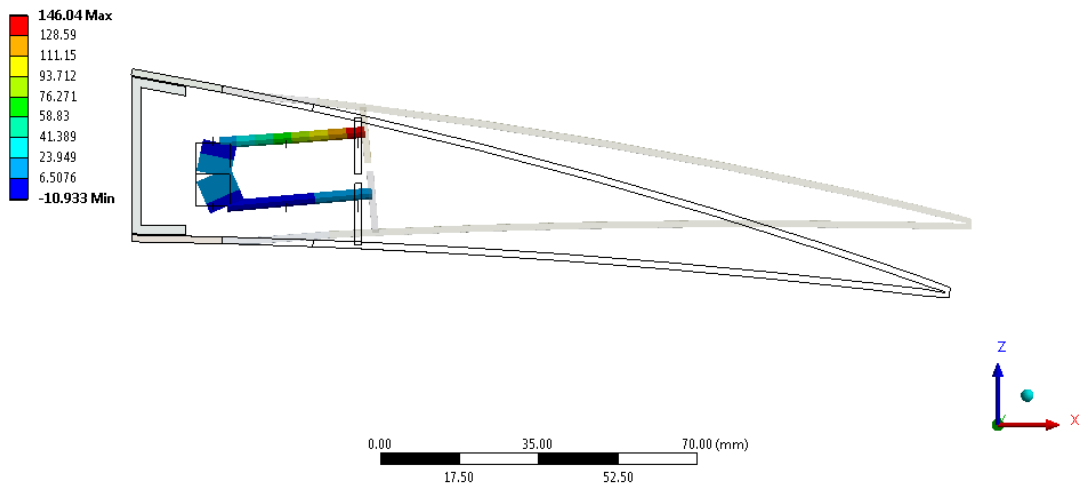


Figure 55: The Combined Beam Stresses for 15.2 [mm] Decamber of Open Cell Design – Linear Case – Maximum 146.040 [MPa]



The resulting reaction moments at moment arms are -281 [N-mm] per servo to actuate the upper portion of the transmission part, -382 [N-mm] per servo to actuate the lower portion of the transmission part. These values are below the maximum torque limit of selected servo actuator.

For 20.2 [mm] upward deflection, 18 [deg] rotation about y axis was prescribed for moment arms of servo actuators to drive the upper portion of transmission parts, and -35 [deg] rotation about y axis was prescribed for moment arms of servo actuators to drive the lower portion of transmission parts as boundary conditions. Transverse displacement contours are shown in Figure 56. von-Mises strain distribution contours are depicted in Figure 57. The combined beam stresses are shown in Figure 58.

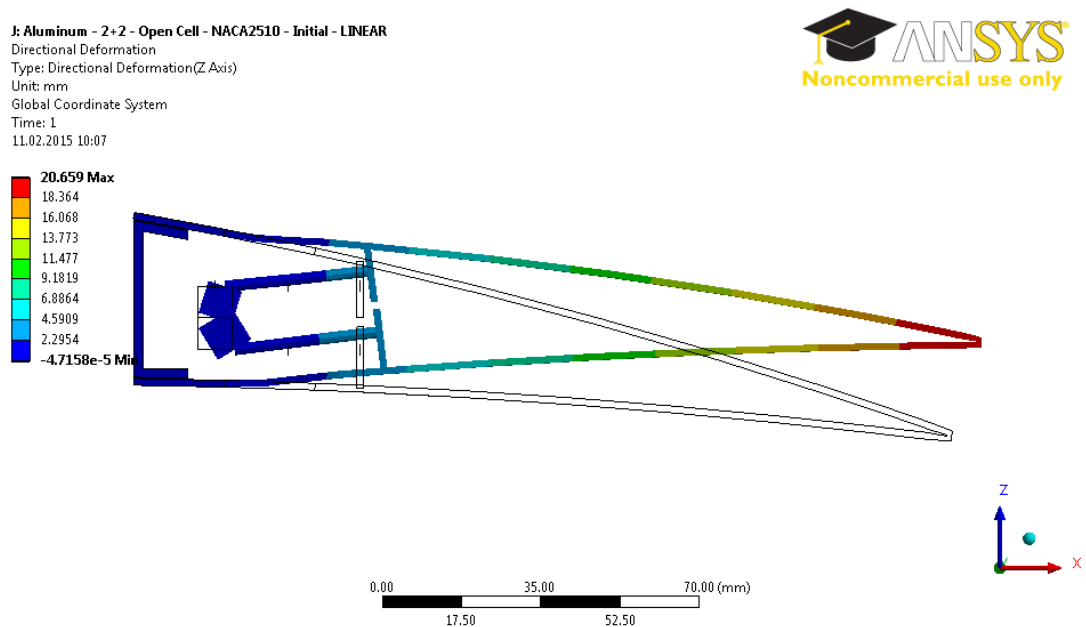


Figure 56: Transverse Displacement Contours for 20.2 [mm] Decamber of Open Cell Design – Linear Case – Maximum 20.659 [mm]

J: Aluminum - 2+2 - Open Cell - NACA2510 - Initial - LINEAR  
 Equivalent Elastic Strain  
 Type: Equivalent Elastic Strain - Top/Bottom - Layer 0  
 Unit: mm/mm  
 Time: 1  
 11.02.2015 10:06

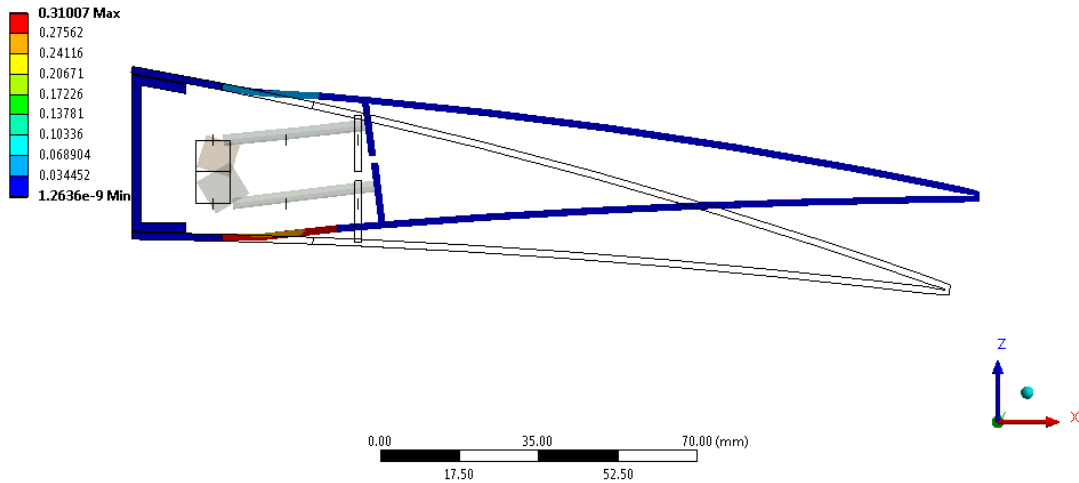


Figure 57: von-Mises Strain Distribution Contours for 20.2 [mm] Decamber of Open Cell Design – Linear Case – Maximum 0.310 [mm/mm]

J: Aluminum - 2+2 - Open Cell - NACA2510 - Initial - LINEAR  
 Maximum Combined Stress  
 Type: Maximum Combined Stress - Top/Bottom - Layer 0  
 Unit: MPa  
 Time: 1  
 11.02.2015 10:07

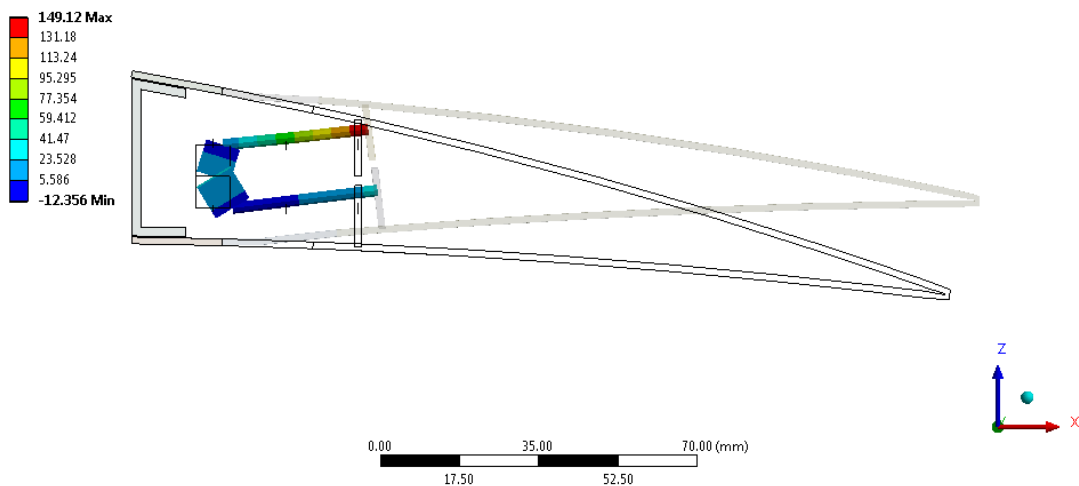


Figure 58: The Combined Beam Stresses for 20.2 [mm] Decamber of Open Cell Design – Linear Case – Maximum 149.120 [MPa]

The resulting reaction moments at moment arms are -286 [N-mm] per servo to actuate the upper portion of the transmission part, -432 [N-mm] per servo to actuate the lower portion of the transmission part. These values are below the maximum torque limit of selected servo actuator.

#### **4.2.2.5 Decamber Variations of Open Cell Design – Non-linear Case with Only Geometric Non-linearities**

In order to perform decamber, approximately 15.2 [mm] and 20.2 [mm] upward deflection of the tip of the control surface was tried to be achieved.

For 15.2 [mm] upward deflection, 12 [deg] rotation about y axis was prescribed for moment arms of servo actuators to drive the upper portion of transmission parts, and -25.5 [deg] rotation about y axis was prescribed for moment arms of servo actuators to drive the lower portion of transmission parts as boundary conditions. Transverse displacement contours are shown in Figure 59. von-Mises strain distribution contours are given in Figure 60. The combined beam stresses are shown in Figure 61.

E Aluminum - 2+2 - Open Cell - NACA3510 - Initial - NL  
 Directional Deformation  
 Type: Directional Deformation(Z Axis)  
 Unit: mm  
 Global Coordinate System  
 Time: 1  
 16.02.2015 19:52

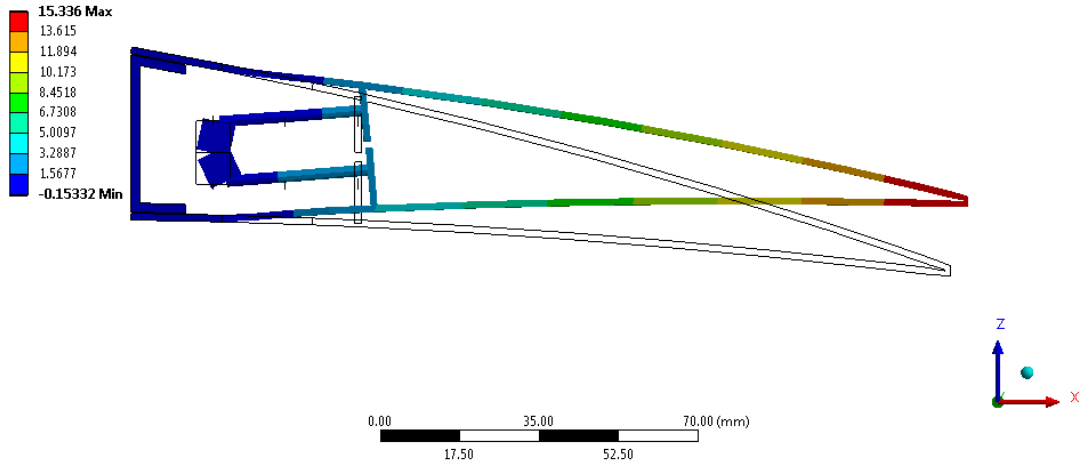


Figure 59: Transverse Displacement Contours for 15.2 [mm] Decamber of Open Cell Design – Non-linear Case with Only Geometric Non-linearities – Maximum 15.336 [mm]

E Aluminum - 2+2 - Open Cell - NACA3510 - Initial - NL  
 Equivalent Elastic Strain  
 Type: Equivalent Elastic Strain - Top/Bottom - Layer 0  
 Unit: mm/mm  
 Time: 1  
 16.02.2015 19:52

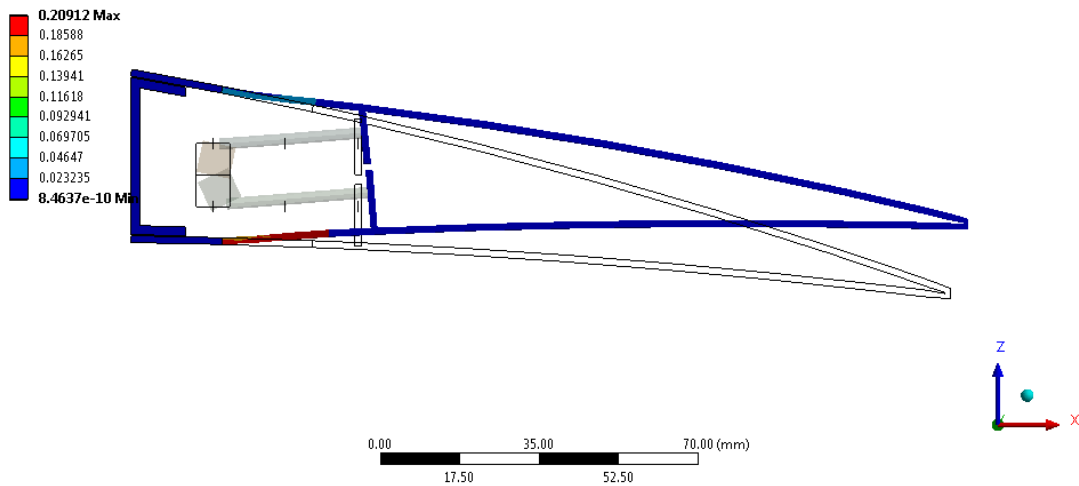


Figure 60: von-Mises Strain Distribution Contours for 15.2 [mm] Decamber of Open Cell Design – Non-linear Case with Only Geometric Non-linearities – Maximum 0.209 [mm/mm]

E: Aluminum - 2+2 - Open Cell - NACA3510 - Initial - NL  
Maximum Combined Stress  
Type: Maximum Combined Stress - Top/Bottom - Layer 0  
Unit: MPa  
Time: 1  
16.02.2015 19:52

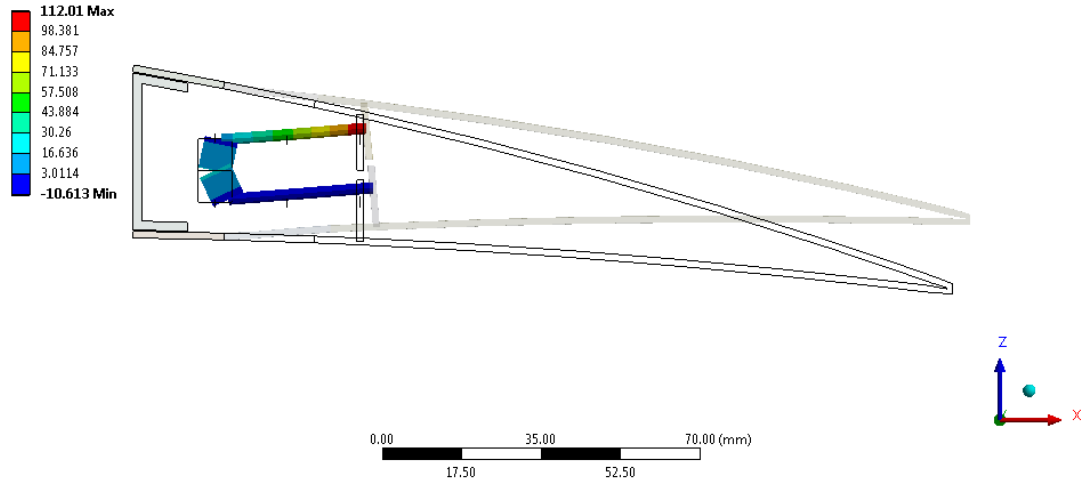


Figure 61: The Combined Beam Stresses for 15.2 [mm] Decamber of Open Cell Design – Non-linear Case with Only Geometric Non-linearities – Maximum 112.010 [MPa]

The resulting reaction moments at moment arms are -289 [N-mm] per servo to actuate the upper portion of the transmission part, -353 [N-mm] per servo to actuate the lower portion of the transmission part. These values are below the maximum torque limit of selected servo actuator.

For 20.2 [mm] upward deflection, 18 [deg] rotation about y axis was prescribed for moment arms of servo actuators to drive the upper portion of transmission parts, and -36 [deg] rotation about y axis was prescribed for moment arms of servo actuators to drive the lower portion of transmission parts as boundary conditions. Transverse displacement contours are shown in Figure 62. von-Mises strain distribution contours are given in Figure 63. The combined beam stresses are shown in Figure 64.

J: Aluminum - 2+2 - Open Cell - NACA2510 - Initial - NL  
 Directional Deformation  
 Type: Directional Deformation(Z Axis)  
 Unit: mm  
 Global Coordinate System  
 Time: 1  
 16.02.2015 19:53

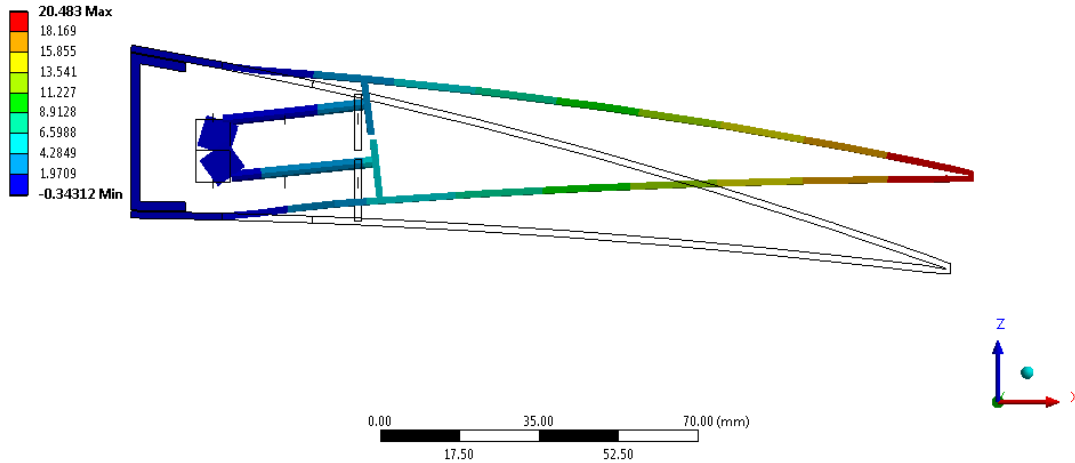


Figure 62: Transverse Displacement Contours for 20.2 [mm] Decamber of Open Cell Design – Non-linear Case with Only Geometric Non-linearities – Maximum 20.483 [mm]

J: Aluminum - 2+2 - Open Cell - NACA2510 - Initial - NL  
 Equivalent Elastic Strain  
 Type: Equivalent Elastic Strain - Top/Bottom - Layer 0  
 Unit: mm/mm  
 Time: 1  
 16.02.2015 19:53

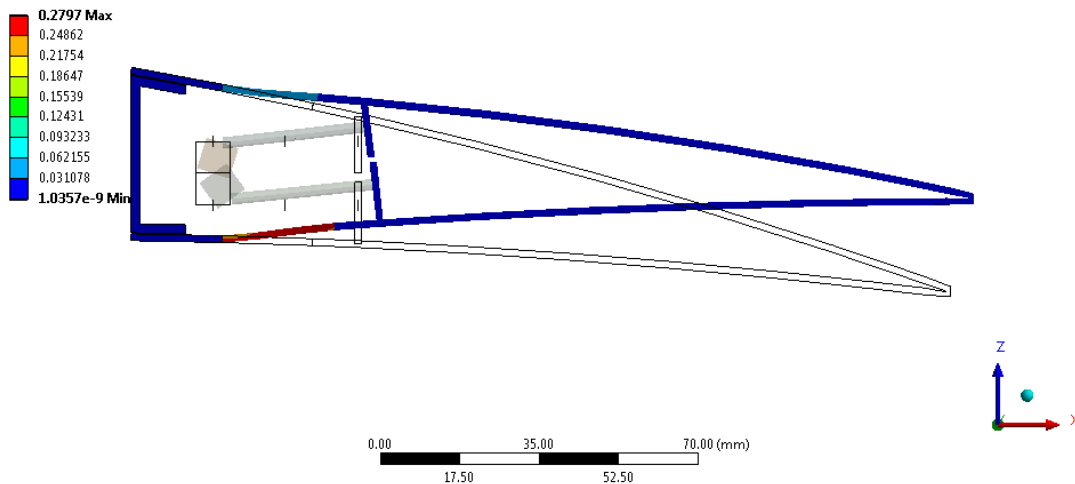


Figure 63: von-Mises Strain Distribution Contours for 20.2 [mm] Decamber of Open Cell Design – Non-linear Case with Only Geometric Non-linearities – Maximum 0.280 [mm/mm]

J: Aluminum - 2+2 - Open Cell - NACA2510 - Initial - NL  
Maximum Combined Stress  
Type: Maximum Combined Stress - Top/Bottom - Layer 0  
Unit: MPa  
Time: 1  
16.02.2015 19:53

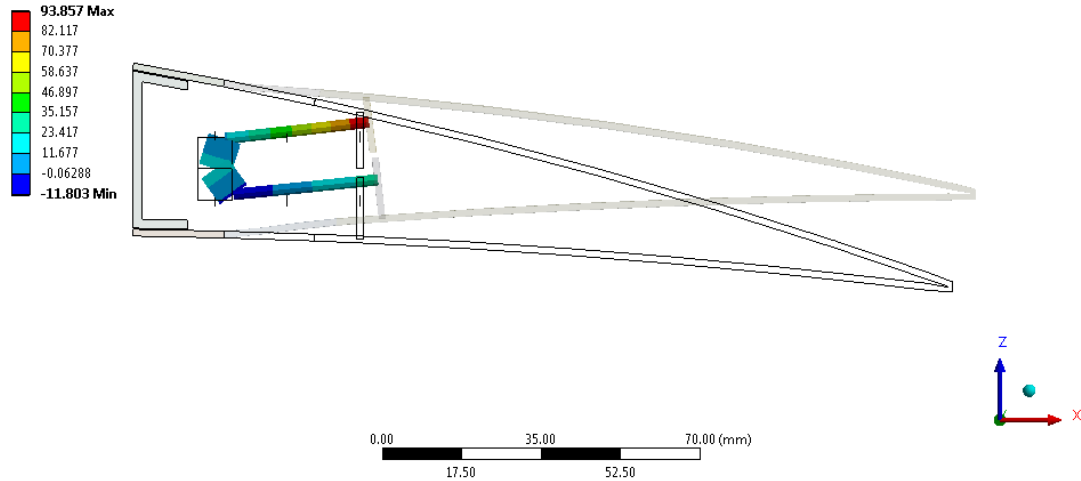


Figure 64: The Combined Beam Stresses for 20.2 [mm] Decamber of Open Cell Design – Non-linear Case with Only Geometric Non-linearities – Maximum 93.857 [MPa]

The resulting reaction moments at moment arms are -294 [N-mm] per servo to actuate the upper portion of the transmission part, -373 [N-mm] per servo to actuate the lower portion of the transmission part. These values are below the maximum torque limit of selected servo actuator.

#### 4.2.2.6 Decamber Variations of Open Cell Design – Non-linear Case with Geometric and Material Non-linearities

In order to perform decamber, approximately 15.2 [mm] and 20.2 [mm] upward deflection of the tip of the control surface was tried to be achieved.

For 15.2 [mm] upward deflection, 12 [deg] rotation about y axis was prescribed for moment arms of servo actuators to drive the upper portion of transmission parts, and -25.5 [deg] rotation about y axis was prescribed for moment arms of servo actuators to drive the lower portion of transmission parts as boundary conditions. Transverse displacement contours are shown in Figure 65. von-Mises strain

distribution contours are given in Figure 66. The combined beam stresses are shown in Figure 67.

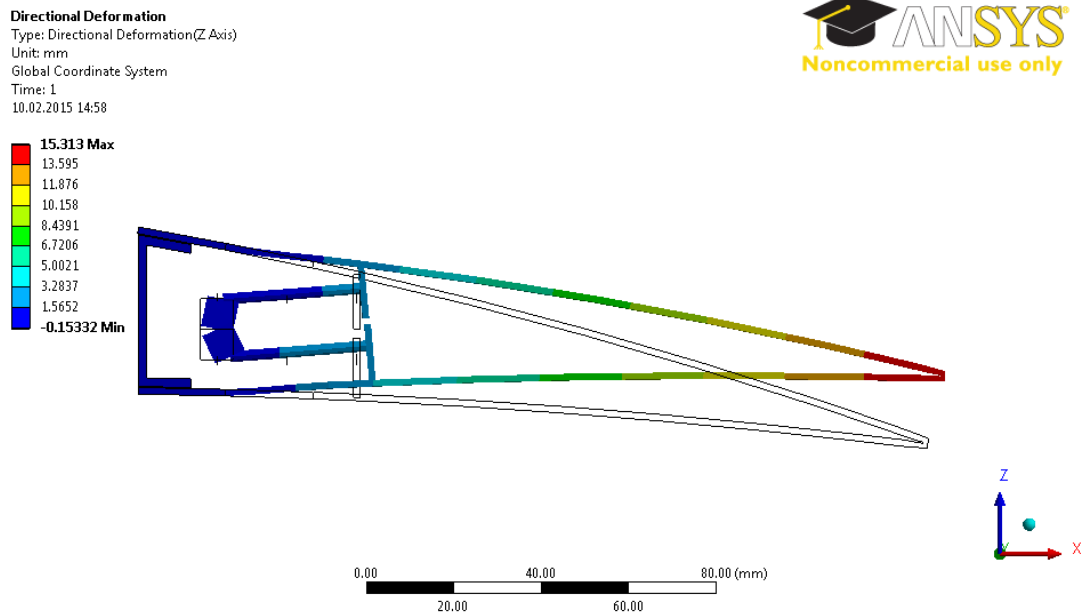


Figure 65: Transverse Displacement Contours for 15.2 [mm] Decamber of Open Cell Design – Non-linear Case with Geometric and Material Non-linearities – Maximum 15.313 [mm]



**Equivalent Elastic Strain 2**  
 Type: Equivalent Elastic Strain - Top/Bottom - Layer 0  
 Unit: mm/mm  
 Time: 1  
 10.02.2015 14:58

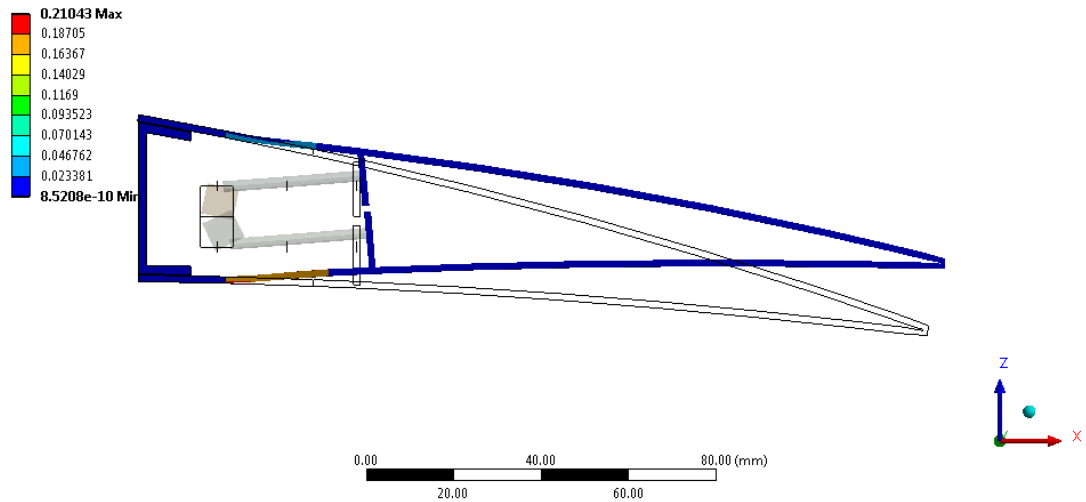


Figure 66: von-Mises Strain Distribution Contours for 15.2 [mm] Decamber of Open Cell Design – Non-linear Case with Geometric and Material Non-linearities – Maximum 0.210 [mm/mm]

**Maximum Combined Stress**  
 Type: Maximum Combined Stress - Top/Bottom - Layer 0  
 Unit: MPa  
 Time: 1  
 10.02.2015 14:58

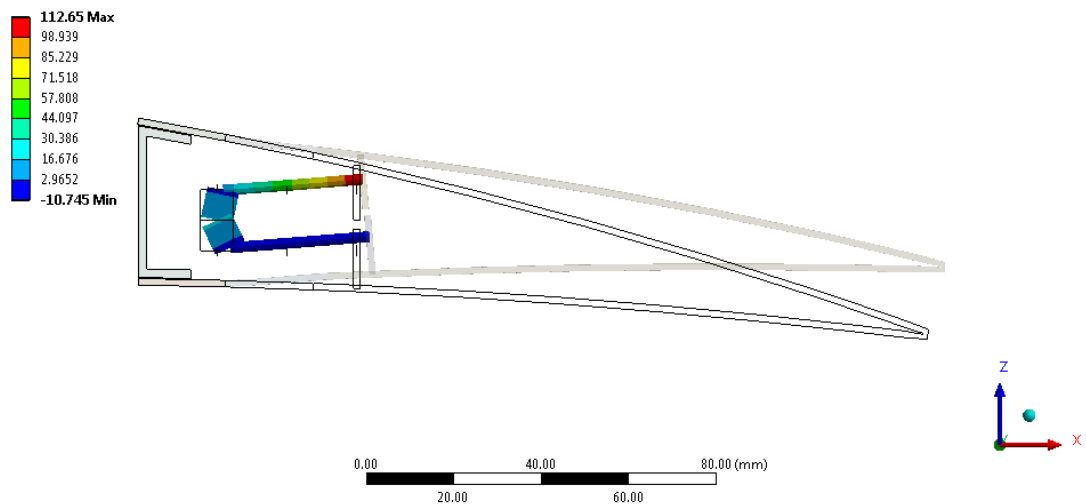


Figure 67: The Combined Beam Stresses for 15.2 [mm] Decamber of Open Cell Design – Non-linear Case with Geometric and Material Non-linearities – Maximum 112.650 [MPa]

The resulting reaction moments at moment arms are -291 [N-mm] per servo to actuate the upper portion of the transmission part, -357 [N-mm] per servo to actuate the lower portion of the transmission part. These values are below the maximum torque limit of selected servo actuator.

For 20.2 [mm] upward deflection, 18 [deg] rotation about y axis was prescribed for moment arms of servo actuators to drive the upper portion of transmission parts, and -36 [deg] rotation about y axis was prescribed for moment arms of servo actuators to drive the lower portion of transmission parts as boundary conditions.

Transverse displacement contours are shown in Figure 68. von-Mises strain distribution contours are given in Figure 69. The combined beam stresses are shown in Figure 70.

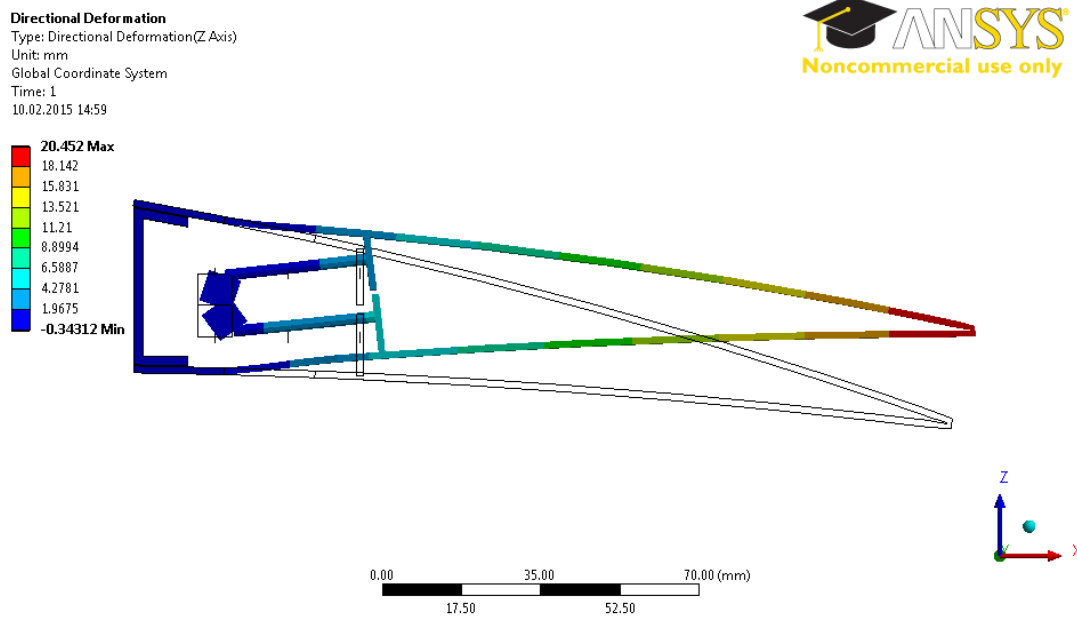


Figure 68: Transverse Displacement Contours for 20.2 [mm] Decamber of Open Cell Design – Non-linear Case with Geometric and Material Non-linearities – Maximum 20.452 [mm]

**Equivalent Elastic Strain**  
 Type: Equivalent Elastic Strain - Top/Bottom - Layer 0  
 Unit: mm/mm  
 Time: 1  
 10.02.2015 14:59

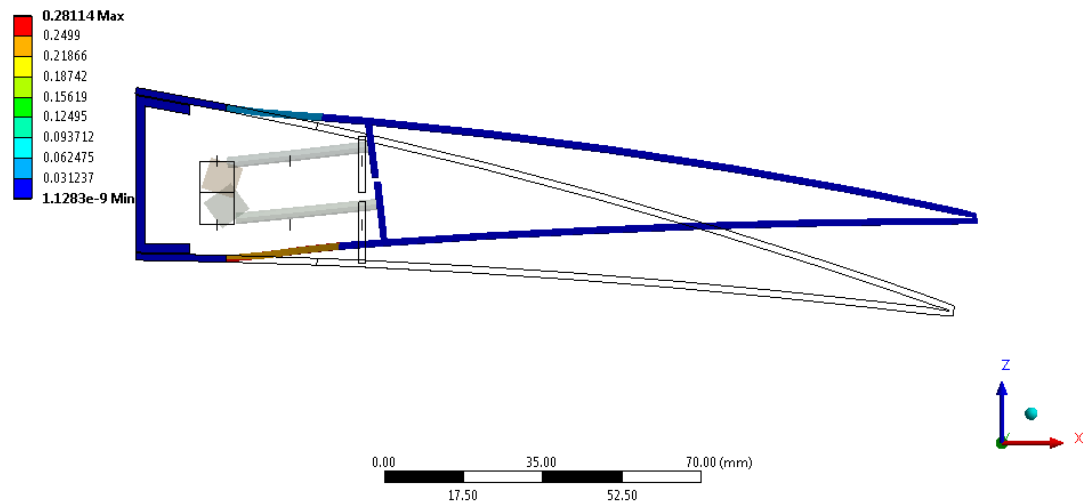


Figure 69: von-Mises Strain Distribution Contours for 20.2 [mm] Decamber of Open Cell Design – Non-linear Case with Geometric and Material Non-linearities – Maximum 0.281 [mm/mm]

**Maximum Combined Stress**  
 Type: Maximum Combined Stress - Top/Bottom - Layer 0  
 Unit: MPa  
 Time: 1  
 10.02.2015 14:59

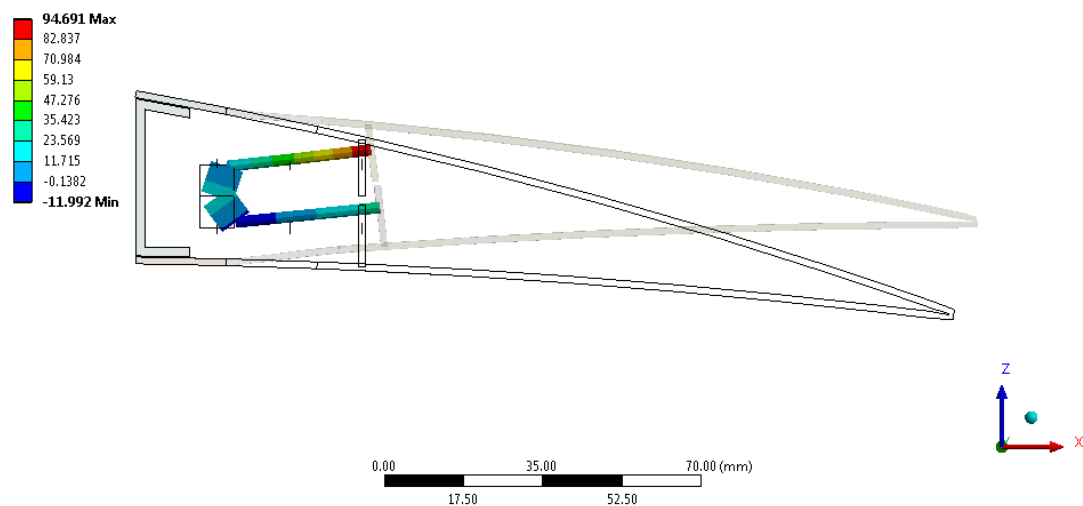


Figure 70: The Combined Beam Stresses for 20.2 [mm] Decamber of Open Cell Design – Non-linear Case with Geometric and Material Non-linearities – Maximum 94.691 [MPa]

The resulting reaction moments at moment arms are -296 [N-mm] per servo to actuate the upper portion of the transmission part, -379 [N-mm] per servo to actuate the lower portion of the transmission part. These values are below the maximum torque limit of selected servo actuator.

#### 4.2.2.7 Discussion and Conclusion

Obtained results for camber and decamber variations for both linear and non-linear cases are summarized as tables. Comparison of maximum von-Mises strain are presented in Table 6, comparison of combined beam stresses are given in Table 7, comparison of required servo actuator torques to actuate the upper and lower portions of the transmission parts are given in Table 8 and Table 9, respectively.

Table 6: Comparison of Maximum von-Mises Strains between Linear and Non-linear Cases

	Linear Case [mm/mm]	Non-linear Case with Only Geometric Non-linearities [mm/mm]	Non-linear Case with Geometric and Material Non- linearities [mm/mm]
15.2 [mm] Camber	0.226	0.208	0.209
15.2 [mm] Decamber	0.222	0.209	0.210
20.2 [mm] Decamber	0.310	0.280	0.281

Table 7: Comparison of Maximum Combined Beam Stresses between Linear and Non-linear Cases

	Linear Case [MPa]	Non-linear Case with Only Geometric Non- linearities [MPa]	Non-linear Case with Geometric and Material Non- linearities [MPa]
15.2 [mm] Camber	77.238	67.516	65.905
15.2 [mm] Decamber	146.040	112.01	112.650
20.2 [mm] Decamber	149.120	93.857	94.691

Table 8: Comparison of Required Servo Actuator Torques for Servos to Actuate the Upper Portion of the Transmission Parts between Linear and Non-linear Cases

	Linear Case [N-mm]	Non-linear Case with Only Geometric Non- linearities [N-mm]	Non-linear Case with Geometric and Material Non- linearities [N-mm]
15.2 [mm] Camber	95.540	141.300	136.170
15.2 [mm] Decamber	280.780	289.010	290.830
20.2 [mm] Decamber	286.120	294.47	296.260

Table 9: Comparison of Required Servo Actuator Torques for Servos to Actuate the Lower Portion of the Transmission Parts between Linear and Non-linear Cases

	Linear Case [N-mm]	Non-linear Case with Only Geometric Non- linearities [N-mm]	Non-linear Case with Geometric and Material Non- linearities [N-mm]
15.2 [mm] Camber	203.000	213.240	210.990
15.2 [mm] Decamber	382.920	353.080	357.250
20.2 [mm] Decamber	431.920	373.310	378.730

According to the tables presented above, the linear case shows a substantial deviation from the non-linear cases. The most reliable solutions are the non-linear case with geometric and material non-linearities, since these solutions use the exact material model while the rest using the linearized material model. It must be noted that the results do not differ significantly between non-linear cases of only geometric non-linearities, and non-linear case with geometric and material non-linearities. In addition, the elimination of the material non-linearity is also known to reduce the computational time. However, from now on, all the solutions will be performed with non-linear case with geometric and material non-linearities in order to use the exact material model and to calculate necessary torque requirements of servo actuators more accurately.

#### 4.2.3 Analysis of Material Variations of Open Cell Design

In the previous section, it is shown that the designed hybrid trailing edge control surface is capable of performing both camber and decamber. It is also stated that strains in the rigid part are negligible.

In this section, the material of the rigid part is changed to glass-fibre prepreg EHG250-68-37 composite to check whether this material can also have small strains or not. Since the thickness of rigid part is 1.5 [mm] and ply thickness of composite is 0.25 [mm], total number of six plies were used to model the material. Orientation of plies were defined as  $0^\circ/90^\circ/0^\circ/0^\circ/90^\circ/0^\circ$  where  $0^\circ$  denotes orientation in chordwise direction and  $90^\circ$  denotes orientation in spanwise direction. Both camber and decamber variations were taken into account in this section.

In order to increase camber, approximately 15.2 [mm] downward deflection of the tip of the control surface was tried to be achieved. 20 [deg] rotation about y axis was prescribed for moment arms of servo actuators to drive the upper portion of transmission parts, and -12 [deg] rotation about y axis was prescribed for moment arms of servo actuators to drive the lower portion of transmission parts as boundary conditions.

Transverse displacement contours are shown in Figure 71. von-Mises strain distribution contours are given in Figure 72.

R: Composite - 2+2 - Open Cell - NACA9510  
 Directional Deformation  
 Type: Directional Deformation(Z Axis)  
 Unit: mm  
 Global Coordinate System  
 Time: 1  
 10.02.2015 14:44

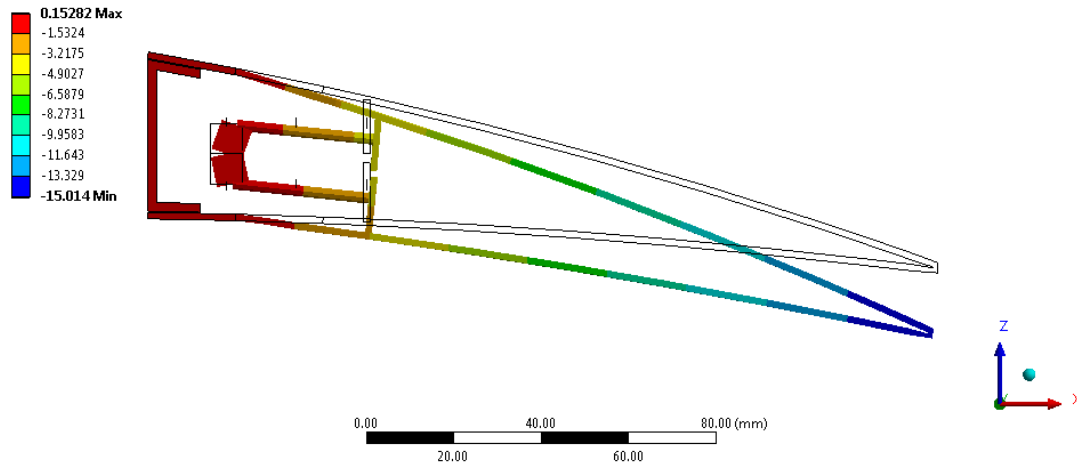


Figure 71: Transverse Displacement Contours for 15.2 [mm] Camber of Open Cell Design – The Rigid Part is Composite – Maximum 15.014 [mm]

R: Composite - 2+2 - Open Cell - NACA9510  
 Equivalent Elastic Strain 2  
 Type: Equivalent Elastic Strain - Top/Bottom - Layer 0  
 Unit: mm/mm  
 Time: 1  
 10.02.2015 14:45

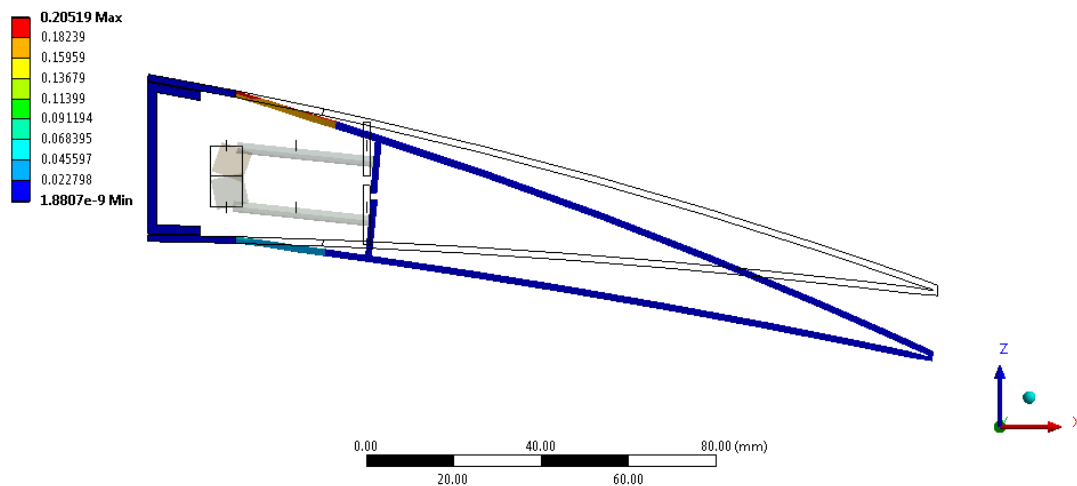


Figure 72: von-Mises Strain Distribution Contours for 15.2 [mm] Camber of Open Cell Design – The Rigid Part is Composite – Maximum 0.205 [mm/mm]



It can be seen from Figure 72 that using composite instead of Aluminium does not alter the characteristics of the rigid part. In other words, the strains in the rigid part are also negligible for composite. The combined beam stresses are shown in Figure 73.

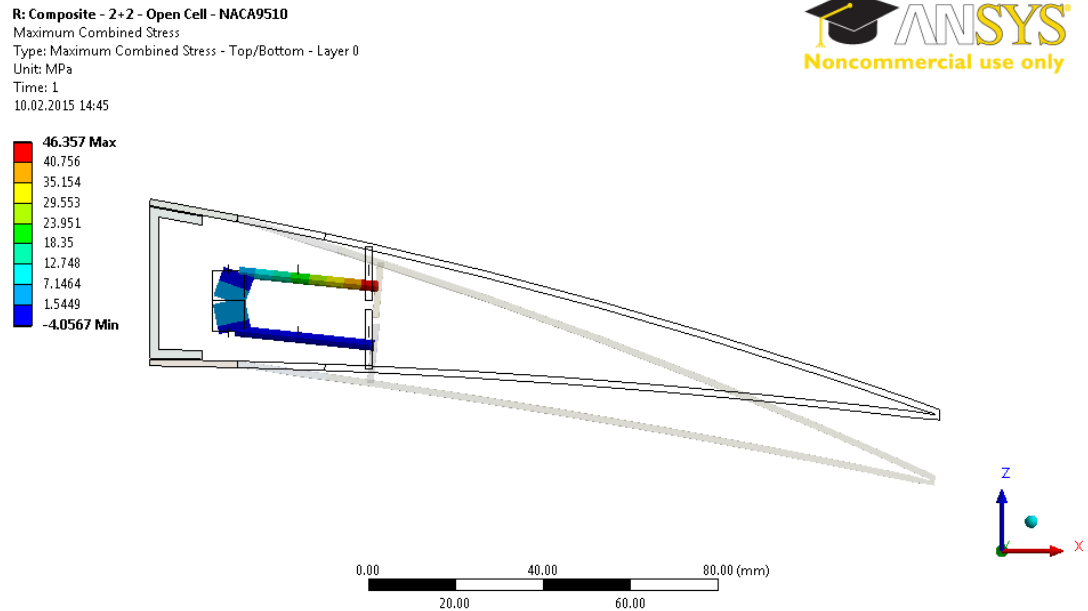


Figure 73: The Combined Beam Stresses for 15.2 [mm] Camber of Open Cell Design – The Rigid Part is Composite – Maximum 46.357 [MPa]

The resulting reaction moments at moment arms are -59 [N-mm] per servo to actuate the upper portion of the transmission part, -133 [N-mm] per servo to actuate the lower portion of the transmission part. These values are below the maximum torque limit of selected servo actuator.

For 15.2 [mm] upward deflection, 11 [deg] rotation about y axis was prescribed for moment arms of servo actuators to drive the upper portion of transmission parts, and -27 [deg] rotation about y axis was prescribed for moment arms of servo actuators to drive the lower portion of transmission parts as boundary conditions.

Transverse displacement contours are shown in Figure 74. von-Mises strain distribution contours are given in Figure 75. The combined beam stresses are shown in Figure 76.

P: Composite - 2+2 - Open Cell - NACA3510  
 Directional Deformation  
 Type: Directional Deformation(Z Axis)  
 Unit: mm  
 Global Coordinate System  
 Time: 1  
 10.02.2015 14:46

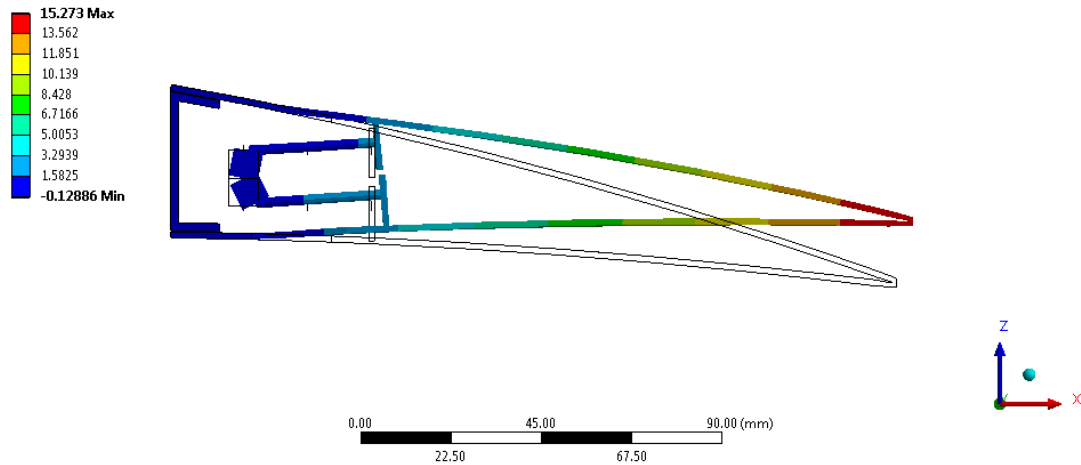


Figure 74: Transverse Displacement Contours for 15.2 [mm] Decamber of Open Cell Design – The Rigid Part is Composite – Maximum 15.273 [mm]

P: Composite - 2+2 - Open Cell - NACA3510  
 Equivalent Elastic Strain 2  
 Type: Equivalent Elastic Strain - Top/Bottom - Layer 0  
 Unit: mm/mm  
 Time: 1  
 10.02.2015 14:47

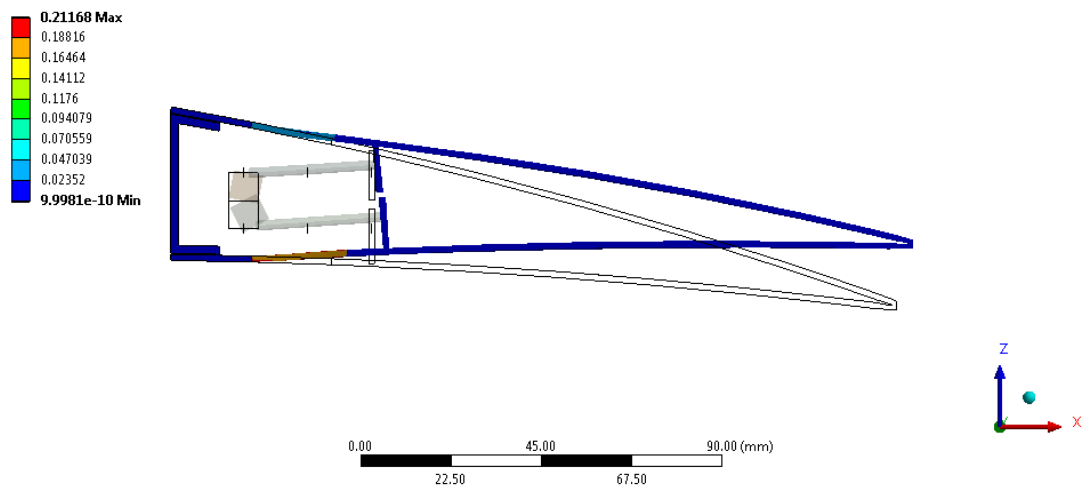


Figure 75: von-Mises Strain Distribution Contours for 15.2 [mm] Decamber of Open Cell Design – The Rigid Part is Composite – Maximum 0.212 [mm/mm]

P: Composite - 2+2 - Open Cell - NACA3510  
Maximum Combined Stress  
Type: Maximum Combined Stress - Top/Bottom - Layer 0  
Unit: MPa  
Time: 1  
10.02.2015 14:48

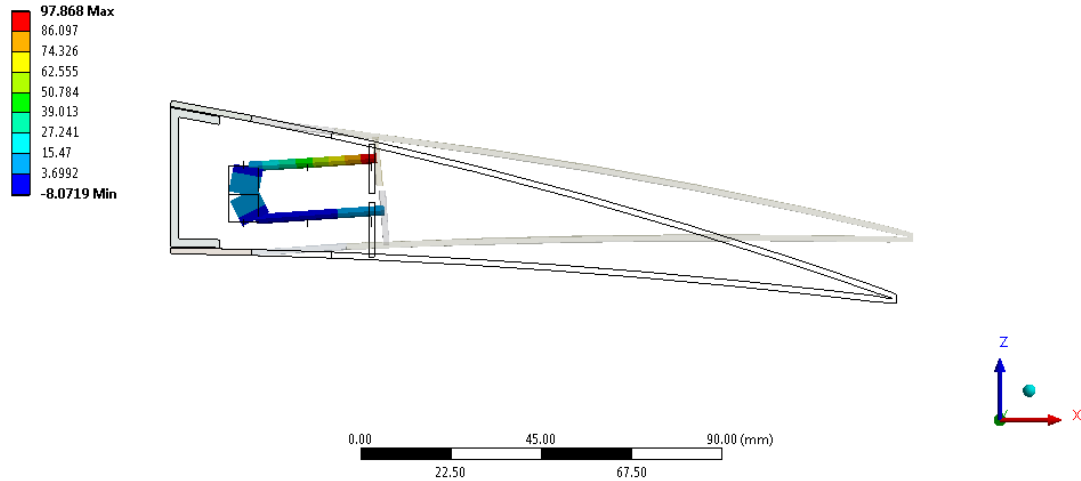


Figure 76: The Combined Beam Stresses for 15.2 [mm] Decamber of Open Cell Design – The Rigid Part is Composite – Maximum 97.868 [MPa]

The resulting reaction moments at moment arms are -210 [N-mm] per servo to actuate the upper portion of the transmission part, -272 [N-mm] per servo to actuate the lower portion of the transmission part. These values are below the maximum torque limit of selected servo actuator.

For 20.2 [mm] upward deflection, 17 [deg] rotation about y axis was prescribed for moment arms of servo actuators to drive the upper portion of transmission parts, and -38 [deg] rotation about y axis was prescribed for moment arms of servo actuators to drive the lower portion of transmission parts as boundary conditions.

Transverse displacement contours are shown in Figure 77. von-Mises strain distribution contours are given in Figure 78. The combined beam stresses are shown in Figure 79.

Q: Composite - 2+2 - Open Cell - NACA2510  
 Directional Deformation  
 Type: Directional Deformation(Z Axis)  
 Unit: mm  
 Global Coordinate System  
 Time: 1  
 10.02.2015 14:48

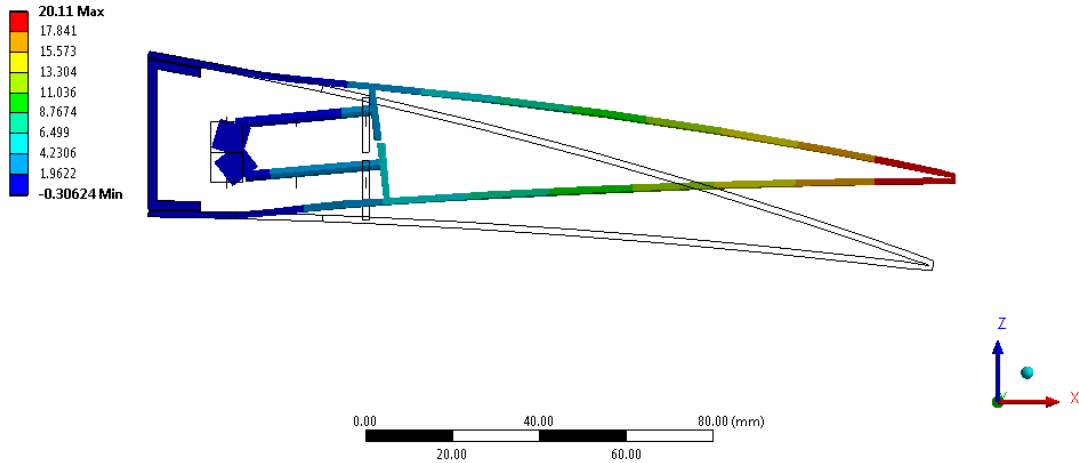


Figure 77: Transverse Displacement Contours for 20.2 [mm] Decamber of Open Cell Design – The Rigid Part is Composite – Maximum 20.110 [mm]

Q: Composite - 2+2 - Open Cell - NACA2510  
 Equivalent Elastic Strain 2  
 Type: Equivalent Elastic Strain - Top/Bottom - Layer 0  
 Unit: mm/mm  
 Time: 1  
 10.02.2015 14:49

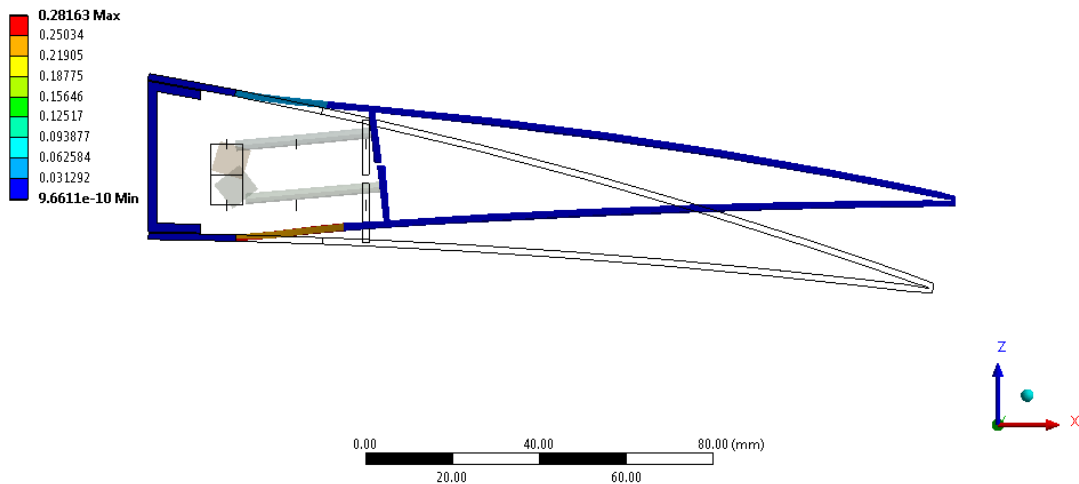


Figure 78: von-Mises Strain Distribution Contours for 20.2 [mm] Decamber of Open Cell Design – The Rigid Part is Composite – Maximum 0.282 [mm/mm]

Q: Composite - 2+2 - Open Cell - NACA2510  
Maximum Combined Stress  
Type: Maximum Combined Stress - Top/Bottom - Layer 0  
Unit: MPa  
Time: 1  
10.02.2015 14:49

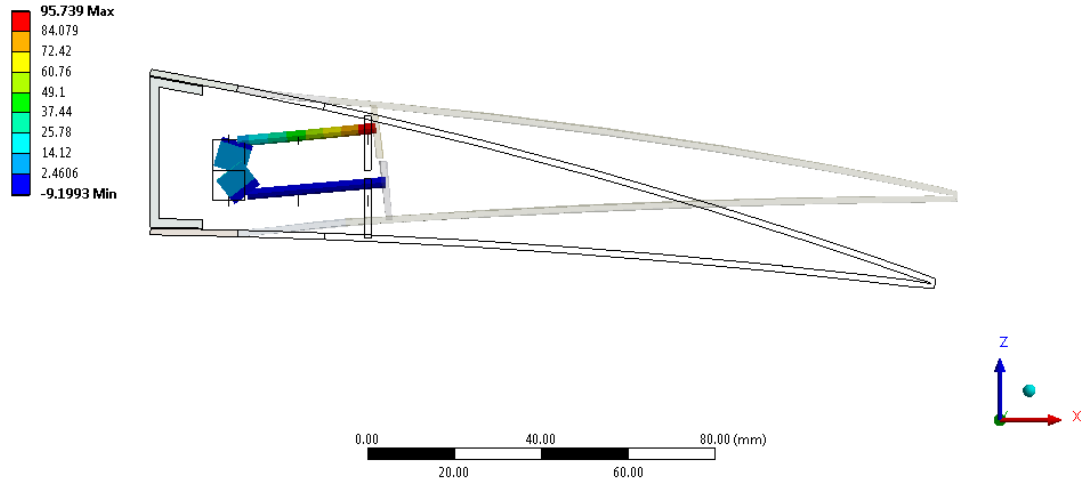


Figure 79: The Combined Beam Stresses for 20.2 [mm] Decamber of Open Cell Design – The Rigid Part is Composite – Maximum 95.739 [MPa]

The resulting reaction moments at moment arms are -220 [N-mm] for servo to actuate the upper portion of the transmission part, -288 [N-mm] for servo to actuate the lower portion of the transmission part. These values are below the maximum torque limit of selected servo actuator.

It can be from the results that composite in rigid part also has negligible strains. Therefore, from now on, in order to reduce the weight of the system while still ensuring that rigid part is stiff enough, the composite will be used as material of the rigid part.

It can also be concluded that both beam stresses and required servo actuator torques are decreased compared to the Aluminum case.

#### 4.2.4 Analysis of Geometric Variations of Open Cell Design

Now that the rigid part's material was fixed, in this section, thickness of the skin parts was changed to 1 [mm] to reduce the weight further. Analyses were

performed again to check whether this thickness could withstand the actuation loads or not.

Since 1 [mm] skin thickness was used, in rigid part four plies were used with  $0^\circ/90^\circ/90^\circ/0^\circ$  ply orientation.

In order to increase camber, approximately 15.2 [mm] downward deflection of the tip of the control surface was tried to be achieved. 18.5 [deg] rotation about y axis was prescribed for moment arms of servo actuators to drive the upper portion of transmission parts, and -12 [deg] rotation about y axis was prescribed for moment arms of servo actuators to drive the lower portion of transmission parts as boundary conditions.

Transverse displacement contours are shown in Figure 80. von-Mises strain distribution contours are shown in Figure 81. The combined beam stresses are shown in Figure 82.

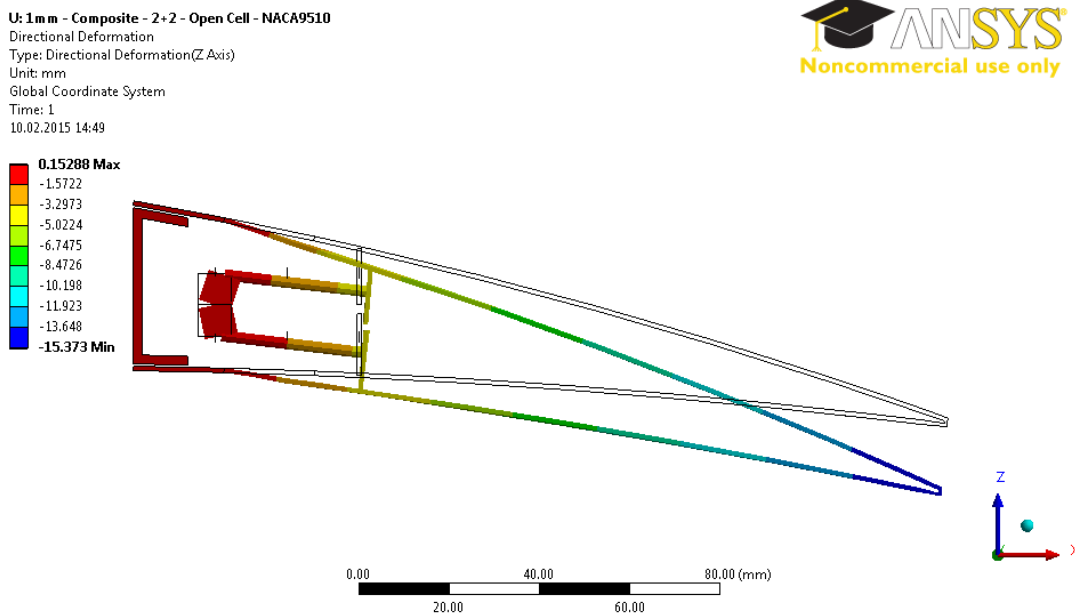


Figure 80: Transverse Displacement Contours for 15.2 [mm] Camber of Open Cell Design – The Skin Thicknesses are 1 [mm] – Maximum 15.373 [mm]

U: 1 mm - Composite - 2+2 - Open Cell - NACA9510  
 Equivalent Elastic Strain 2  
 Type: Equivalent Elastic Strain - Top/Bottom - Layer 0  
 Unit: mm/mm  
 Time: 1  
 10.02.2015 14:50

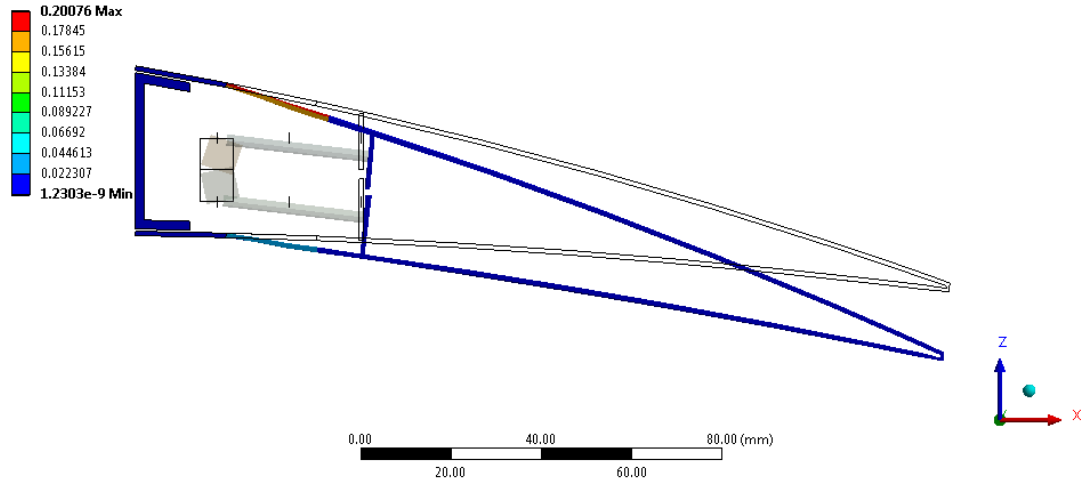


Figure 81: von-Mises Strain Distribution Contours for 15.2 [mm] Camber Increase of Open Cell Design – The Skin Thicknesses are 1 [mm] – Maximum 0.201 [mm/mm]

U: 1 mm - Composite - 2+2 - Open Cell - NACA9510  
 Maximum Combined Stress  
 Type: Maximum Combined Stress - Top/Bottom - Layer 0  
 Unit: MPa  
 Time: 1  
 10.02.2015 14:50

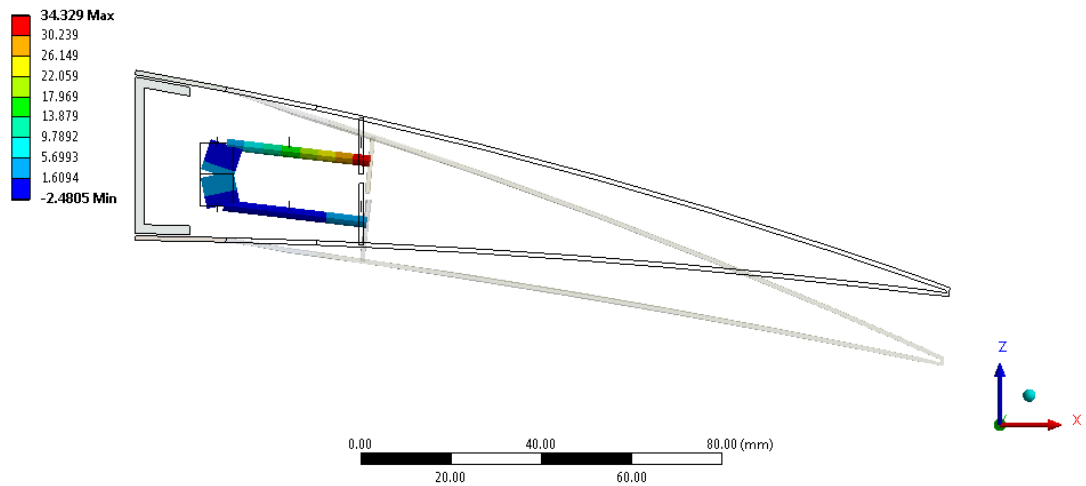


Figure 82: The Combined Beam Stresses for 15.2 [mm] Camber Increase of Open Cell Design – The Skin Thicknesses are 1 [mm] – Maximum 34.329 [MPa]

The resulting reaction moments at moment arms are -40 [N-mm] per servo to actuate the upper portion of the transmission part, -86 [N-mm] per servo to actuate the lower portion of the transmission part. These values are below the maximum torque limit of selected servo actuator.

For 15.2 [mm] upward deflection, 9 [deg] rotation about y axis was prescribed for moment arms of servo actuators to drive the upper portion of transmission parts, and -29.5 [deg] rotation about y axis was prescribed for moment arms of servo actuators to drive the lower portion of transmission parts as boundary conditions.

Transverse displacement contours are shown in Figure 83. von-Mises strain distribution contours are shown in Figure 84. The combined beam stresses are shown in Figure 85.

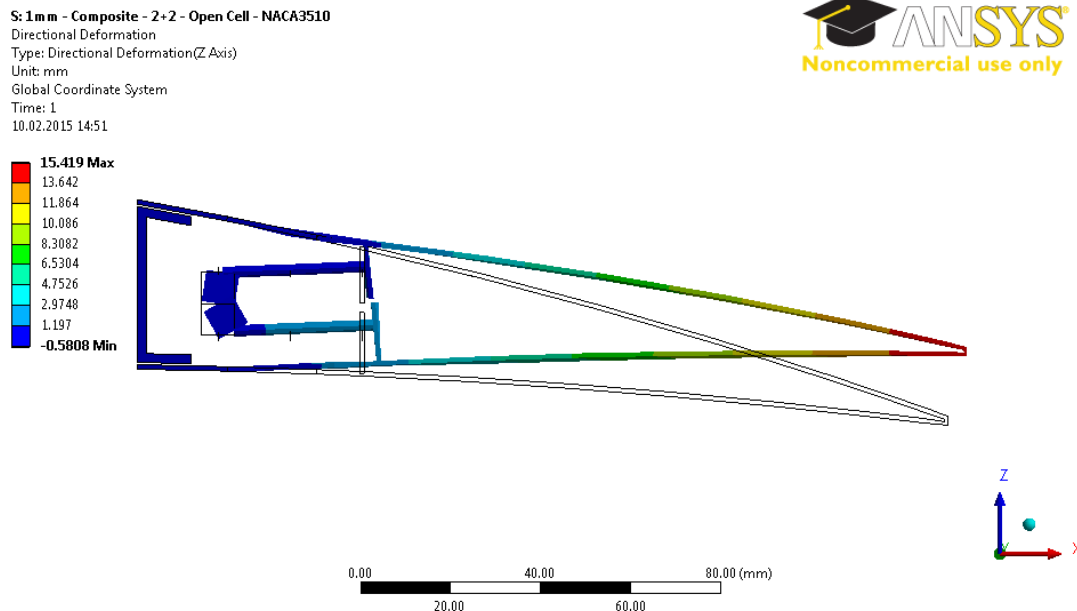


Figure 83: Transverse Displacement Contours for 15.2 [mm] Deflection of Open Cell Design – The Skin Thicknesses are 1 [mm] – Maximum 15.419 [mm]



S: 1mm - Composite - 2+2 - Open Cell - NACA3510  
 Equivalent Elastic Strain 2  
 Type: Equivalent Elastic Strain - Top/Bottom - Layer 0  
 Unit: mm/mm  
 Time: 1  
 10.02.2015 14:51

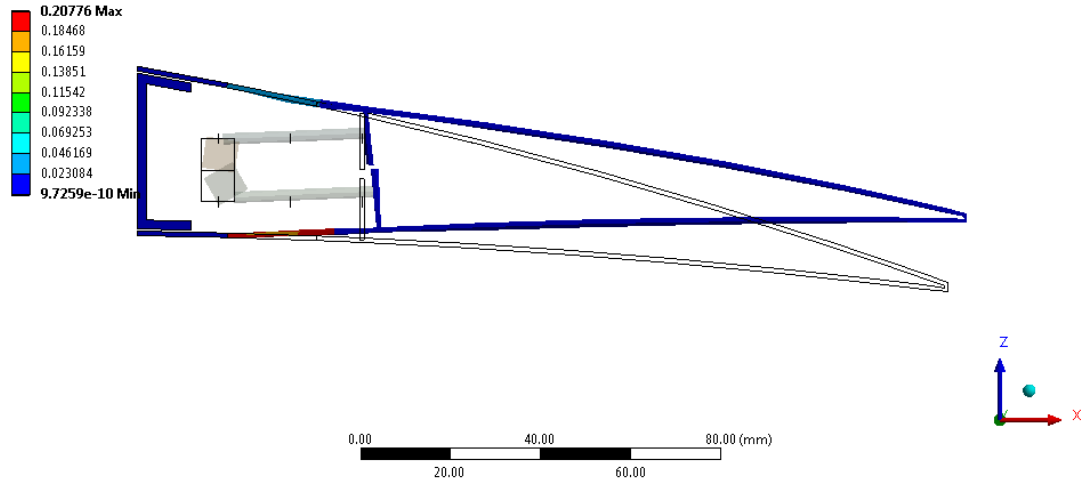


Figure 84: von-Mises Strain Distribution Contours for 15.2 [mm] Decamber of Open Cell Design – The Skin Thicknesses are 1 [mm] – Maximum 0.208 [mm/mm]

S: 1mm - Composite - 2+2 - Open Cell - NACA3510  
 Maximum Combined Stress  
 Type: Maximum Combined Stress - Top/Bottom - Layer 0  
 Unit: MPa  
 Time: 1  
 10.02.2015 14:51

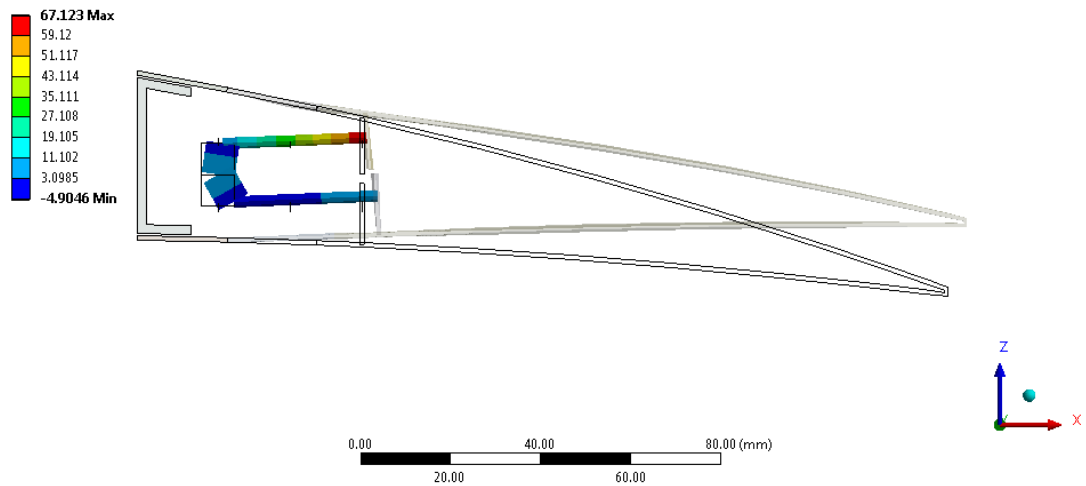


Figure 85: The Combined Beam Stresses for 15.2 [mm] Decamber of Open Cell Design – The Skin Thicknesses are 1 [mm] – Maximum 67.123 [MPa]

The resulting reaction moments at moment arms are -143 [N-mm] for servo to actuate the upper portion of the transmission part, -178 [N-mm] for servo to actuate the lower portion of the transmission part. These values are below the maximum torque limit of selected servo actuator.

For 20.2 [mm] upward deflection, 13 [deg] rotation about y axis was prescribed for moment arms of servo actuators to drive the upper portion of transmission parts, and -39.5 [deg] rotation about y axis was prescribed for moment arms of servo actuators to drive the lower portion of transmission parts as boundary conditions.

Transverse displacement contours are shown in Figure 86. von-Mises strain distribution contours are shown in Figure 87. The combined beam stresses are shown in Figure 88.

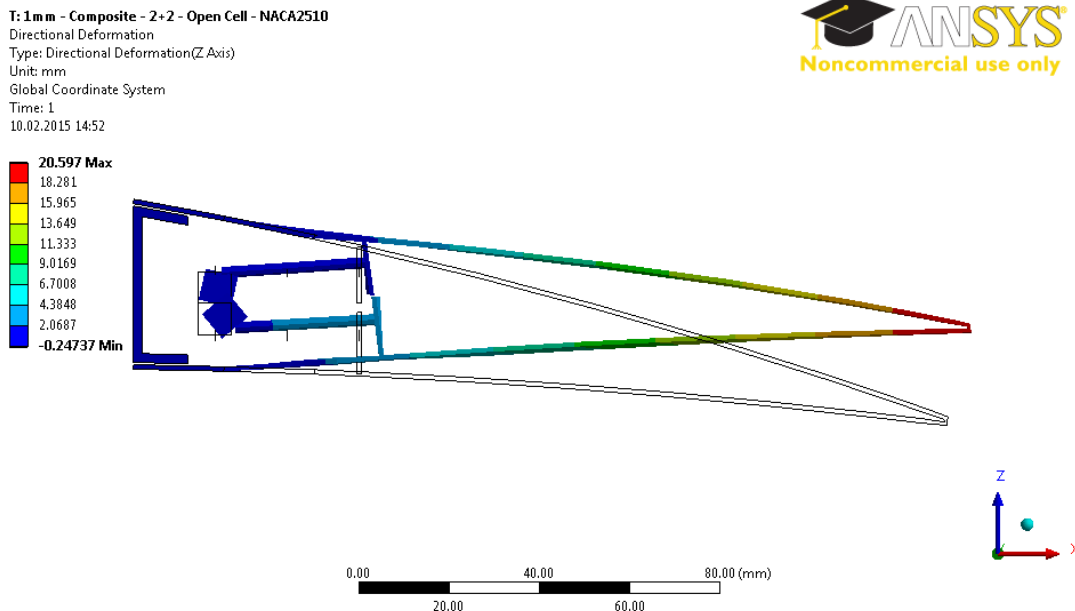


Figure 86: Transverse Displacement Contours for 20.2 [mm] of Open Cell Design – The Skin Thicknesses are 1 [mm] – Maximum 20.597 [mm]

T: 1 mm - Composite - 2+2 - Open Cell - NACA2510  
 Equivalent Elastic Strain 2  
 Type: Equivalent Elastic Strain - Top/Bottom - Layer 0  
 Unit: mm/mm  
 Time: 1  
 10.02.2015 14:52

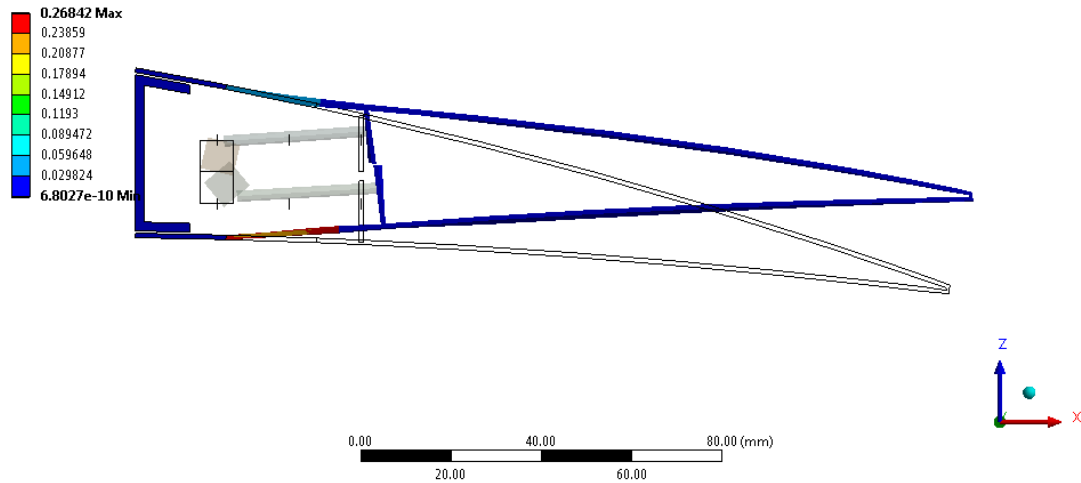


Figure 87: von-Mises Strain Distribution Contours for 20.2 [mm] Decamber of Open Cell Design – The Skin Thicknesses are 1 [mm] – Maximum 0.268 [mm/mm]

T: 1 mm - Composite - 2+2 - Open Cell - NACA2510  
 Maximum Combined Stress  
 Type: Maximum Combined Stress - Top/Bottom - Layer 0  
 Unit: MPa  
 Time: 1  
 10.02.2015 14:53

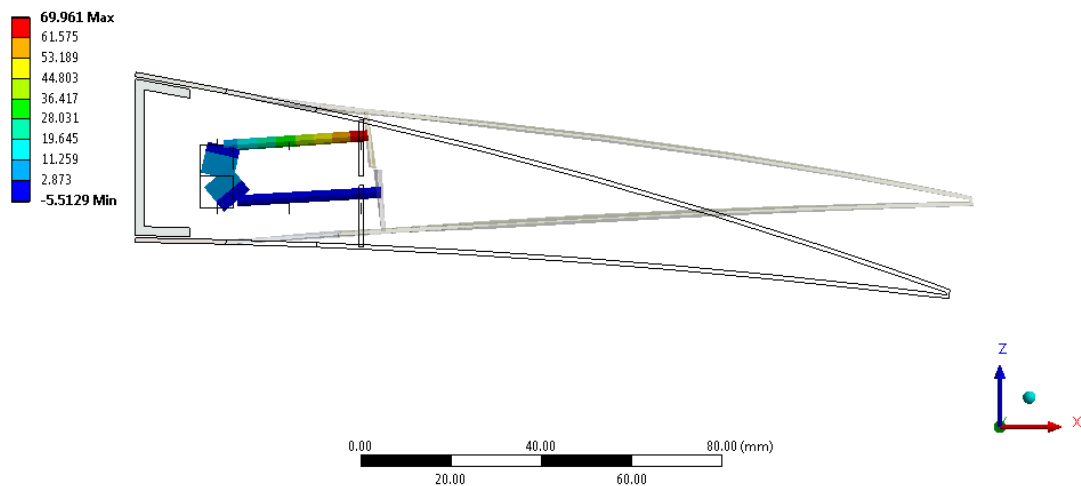


Figure 88: The Combined Beam Stresses for 20.2 [mm] Decamber of Open Cell Design – The Skin Thicknesses are 1 [mm] – Maximum 69.961 [MPa]

The resulting reaction moments at moment arms are -156 [N-mm] for servo to actuate the upper portion of the transmission part, -186 [N-mm] for servo to actuate the lower portion of the transmission part. These values are below the maximum torque limit of selected servo actuator.

It can be concluded from this analysis that 1 [mm] thickness is also acceptable for skin parts. Both C part and rigid part still exhibit almost a rigid body behavior under actuation loads. From now on, skin thicknesses are fixed as 1 [mm].

#### 4.2.5 Analysis of Servo Actuator Variations of Open Cell Design

In this section, number and location of servo actuators were altered in two different ways. Firstly, three servo actuators were utilized for actuation of upper portion of the transmission part and two servo actuators were utilized for actuation of lower portion of the transmission part. This configuration is called as Case 1. The location of servo actuators are depicted in Figure 89.

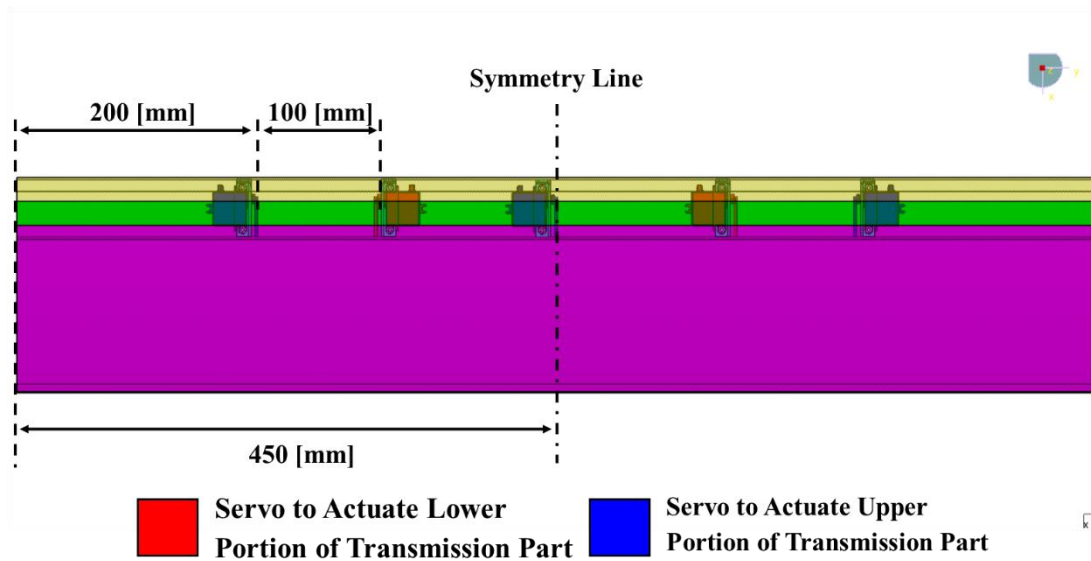


Figure 89: Top View of Servo Actuators in Open Cell Design with Dimensions – Case 1

Secondly, two servo actuators were utilized for actuation of upper portion of the transmission part and three servo actuators were utilized for actuation of lower

portion of the transmission part. This configuration is called as Case 2. The location of servo actuators are shown in Figure 90.

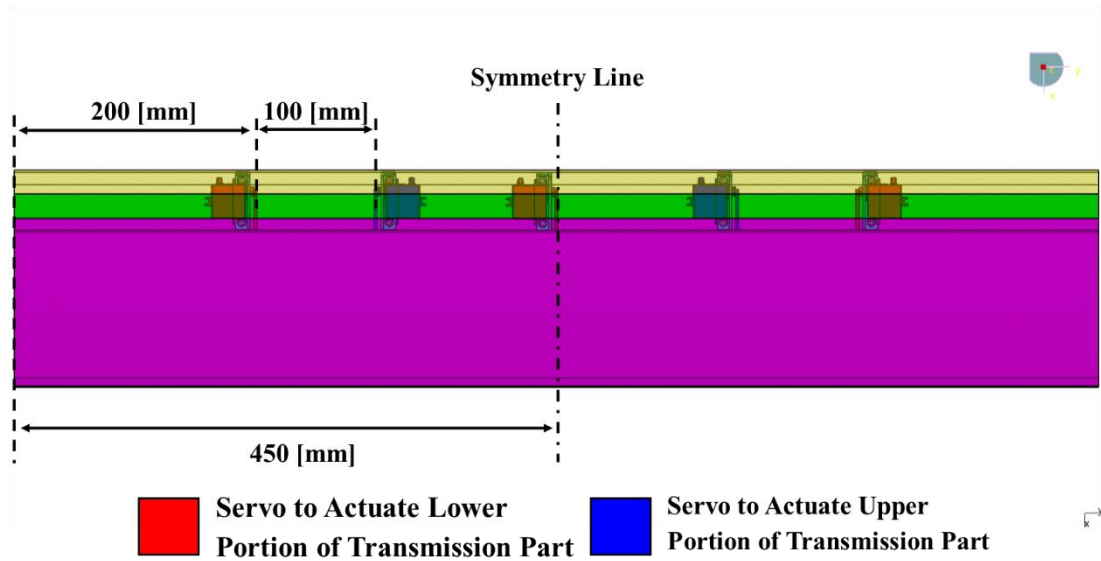


Figure 90: Top View of Servo Actuators in Open Cell Design with Dimensions – Case 2

#### 4.2.5.1 Case 1

In order to increase camber, approximately 15.2 [mm] downward deflection of the tip of the control surface was tried to be achieved. 19 [deg] rotation about y axis was prescribed for moment arms of servo actuators to drive the upper portion of transmission parts, and -12 [deg] rotation about y axis was prescribed for moment arms of servo actuators to drive the lower portion of transmission parts as boundary conditions.

Transverse displacement contours are shown in Figure 91. von-Mises strain distribution contours are shown in Figure 92. The combined beam stresses are shown in Figure 93.

C: 3U-2L - NACA9510  
 Directional Deformation  
 Type: Directional Deformation(Z Axis)  
 Unit: mm  
 Global Coordinate System  
 Time: 1  
 10.02.2015 15:03

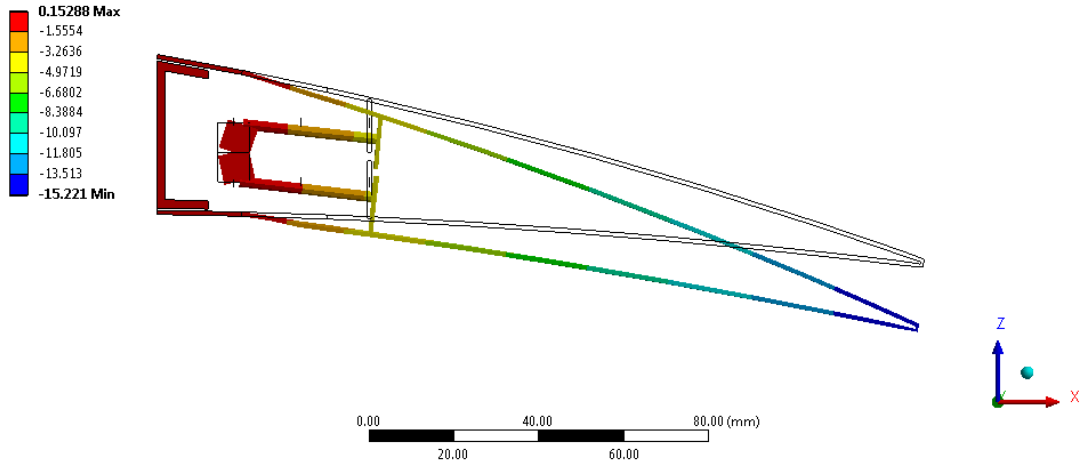


Figure 91: Transverse Displacement Contours for 15.2 [mm] Camber of Open Cell Design – Servo Actuators Variation Case 1 – Maximum 15.221 [mm]

C: 3U-2L - NACA9510  
 Equivalent Elastic Strain 2  
 Type: Equivalent Elastic Strain - Top/Bottom - Layer 0  
 Unit: mm/mm  
 Time: 1  
 10.02.2015 15:03

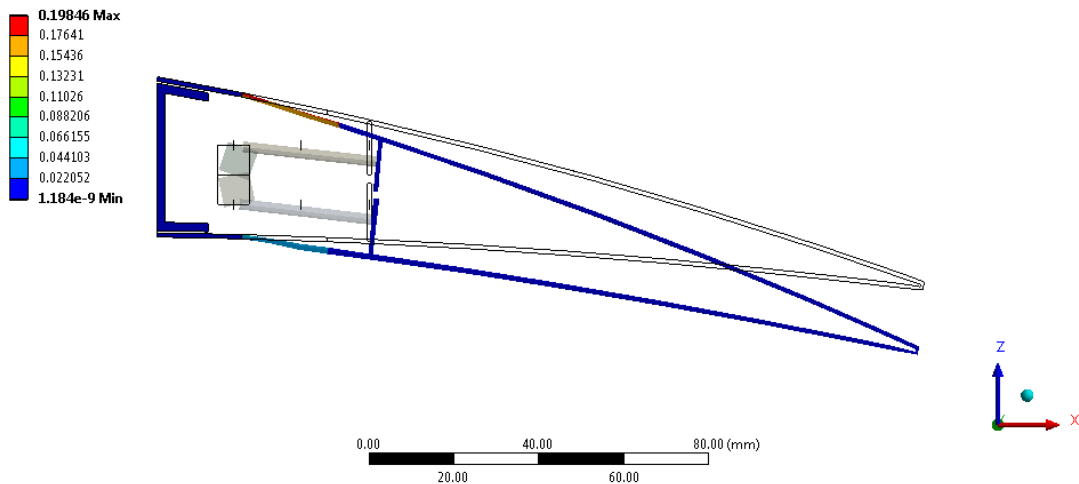


Figure 92: von-Mises Strain Distribution Contours for 15.2 [mm] Camber of Open Cell Design – Servo Actuators Variation Case 1 – Maximum 0.198 [mm/mm]

C: 3U-2L - NACA9510  
Maximum Combined Stress  
Type: Maximum Combined Stress - Top/Bottom - Layer 0  
Unit: MPa  
Time: 1  
10.02.2015 15:04

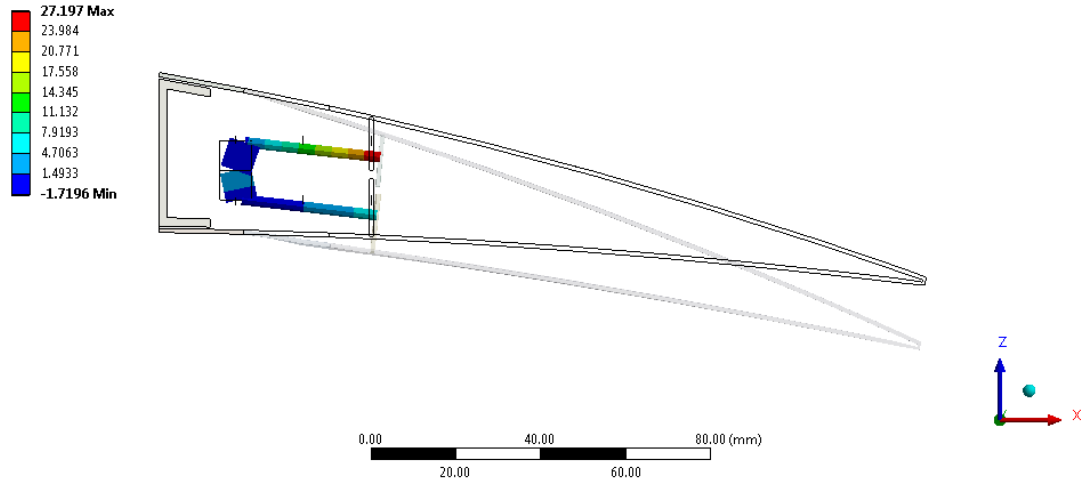


Figure 93: The Combined Beam Stresses for 15.2 [mm] Camber of Open Cell Design  
– Servo Actuators Variation Case 1 – Maximum 27.197 [MPa]

The resulting reaction moments at moment arms are -23 [N-mm] for inboard and outboard servo to actuate the upper portion of the transmission part, -33 [N-mm] for middle servo to actuate the upper portion of the transmission part, -86 [N-mm] for servo to actuate the lower portion of the transmission part. These values are below the maximum torque limit of selected servo actuator.

For 15.2 [mm] upward deflection, 10 [deg] rotation about y axis was prescribed for moment arms of servo actuators to drive the upper portion of transmission parts, and -29 [deg] rotation about y axis was prescribed for moment arms of servo actuators to drive the lower portion of transmission parts as boundary conditions.

Transverse displacement contours are shown in Figure 94. von-Mises strain distribution contours are shown in Figure 95. The combined beam stresses are shown in Figure 96.

A: 3U-2L - NACA3510  
 Directional Deformation  
 Type: Directional Deformation(Z Axis)  
 Unit: mm  
 Global Coordinate System  
 Time: 1  
 10.02.2015 15:04

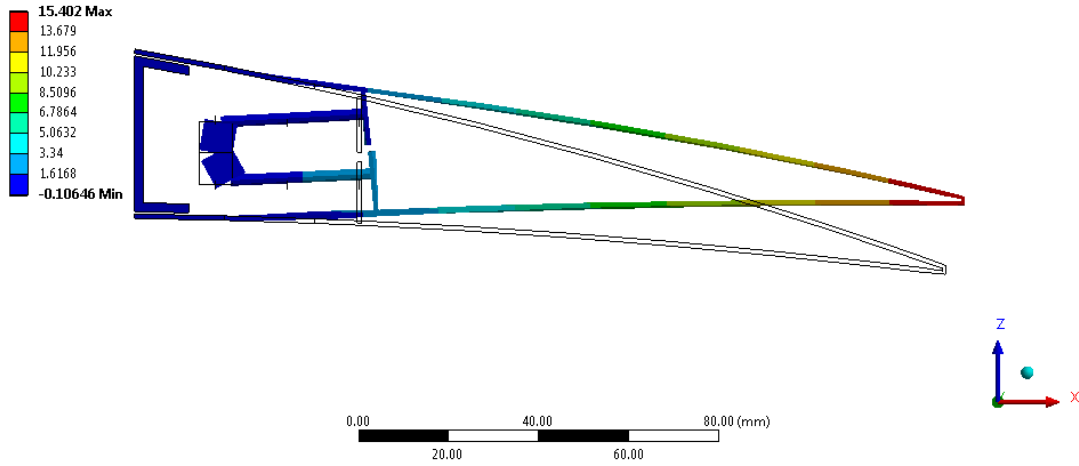


Figure 94: Transverse Displacement Contours for 15.2 [mm] Decamber of Open Cell Design – Servo Actuators Variation Case 1 – Maximum 15.402 [mm]

A: 3U-2L - NACA3510  
 Equivalent Elastic Strain 2  
 Type: Equivalent Elastic Strain - Top/Bottom - Layer 0  
 Unit: mm/mm  
 Time: 1  
 10.02.2015 15:04

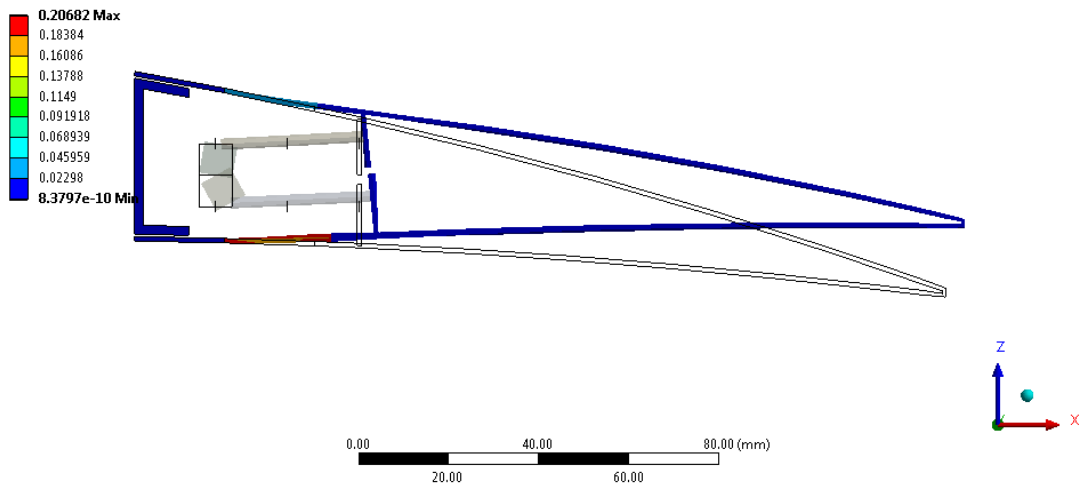


Figure 95: von-Mises Strain Distribution Contours for 15.2 [mm] Decamber of Open Cell Design – Servo Actuators Variation Case 1 – Maximum 0.207 [mm/mm]



A: 3U-2L - NACA3510  
Maximum Combined Stress  
Type: Maximum Combined Stress - Top/Bottom - Layer 0  
Unit: MPa  
Time: 1  
10.02.2015 15:04

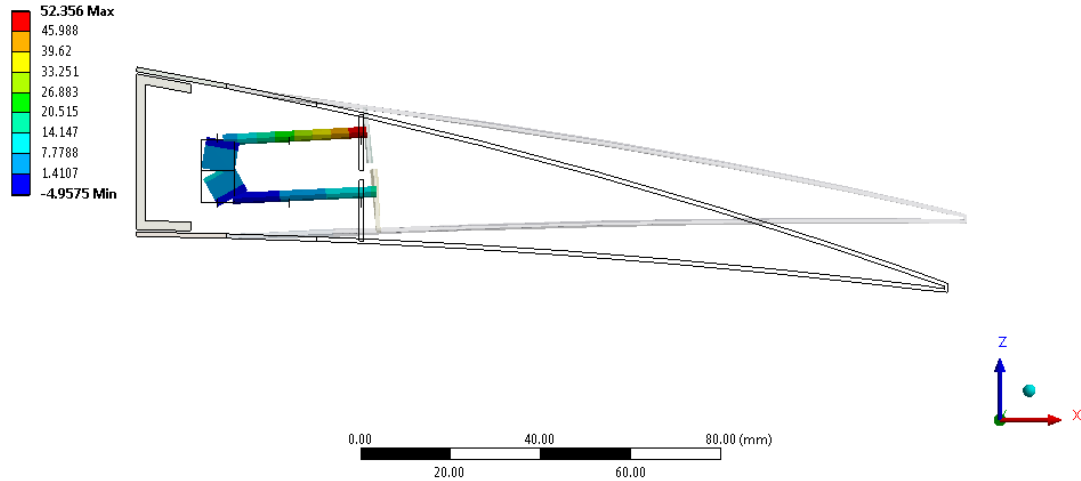


Figure 96: The Combined Beam Stresses for 15.2 [mm] Deflection of Open Cell Design – Servo Actuators Variation Case 1 – Maximum 52.356 [MPa]

The resulting reaction moments at moment arms are -94 [N-mm] for inboard and outboard servo to actuate the upper portion of the transmission part, -100 [N-mm] for middle servo to actuate the upper portion of the transmission part, -178 [N-mm] for servo to actuate the lower portion of the transmission part. These values are below the maximum torque limit of selected servo actuator.

For 20.2 [mm] upward deflection, 13 [deg] rotation about y axis was prescribed for moment arms of servo actuators to drive the upper portion of transmission parts, and -37.5 [deg] rotation about y axis was prescribed for moment arms of servo actuators to drive the lower portion of transmission parts as boundary conditions.

Transverse displacement contours are shown in Figure 97. von-Mises strain distribution contours are shown in Figure 98. The combined beam stresses are shown in Figure 99.

B: 3U-2L - NACA2510  
 Directional Deformation  
 Type: Directional Deformation(Z Axis)  
 Unit: mm  
 Global Coordinate System  
 Time: 1  
 10.02.2015 15:05

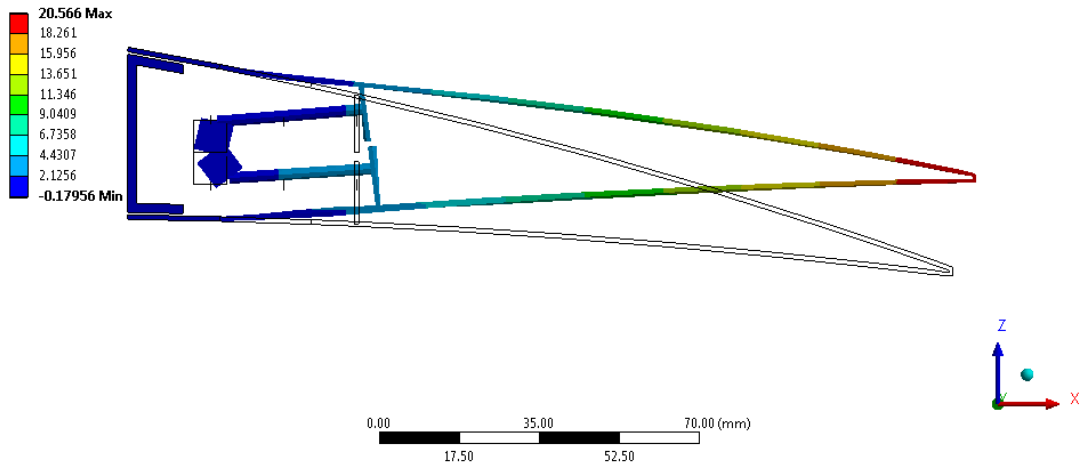


Figure 97: Transverse Displacement Contours for 20.2 [mm] Decamber of Open Cell Design – Servo Actuators Variation Case 1 – Maximum 20.566 [mm]

B: 3U-2L - NACA2510  
 Equivalent Elastic Strain 2  
 Type: Equivalent Elastic Strain - Top/Bottom - Layer 0  
 Unit: mm/mm  
 Time: 1  
 10.02.2015 15:05

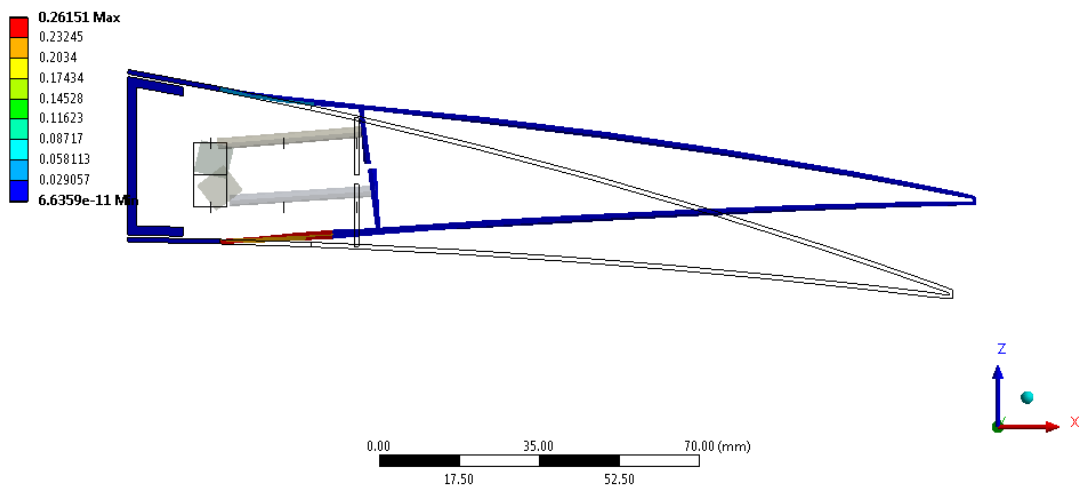


Figure 98: von-Mises Strain Distribution Contours for 20.2 [mm] Decamber of Open Cell Design – Servo Actuators Variation Case 1 – Maximum 0.262 [mm/mm]

B: 3U-2L - NACA2510  
Maximum Combined Stress  
Type: Maximum Combined Stress - Top/Bottom - Layer 0  
Unit: MPa  
Time: 1  
10.02.2015 15:05

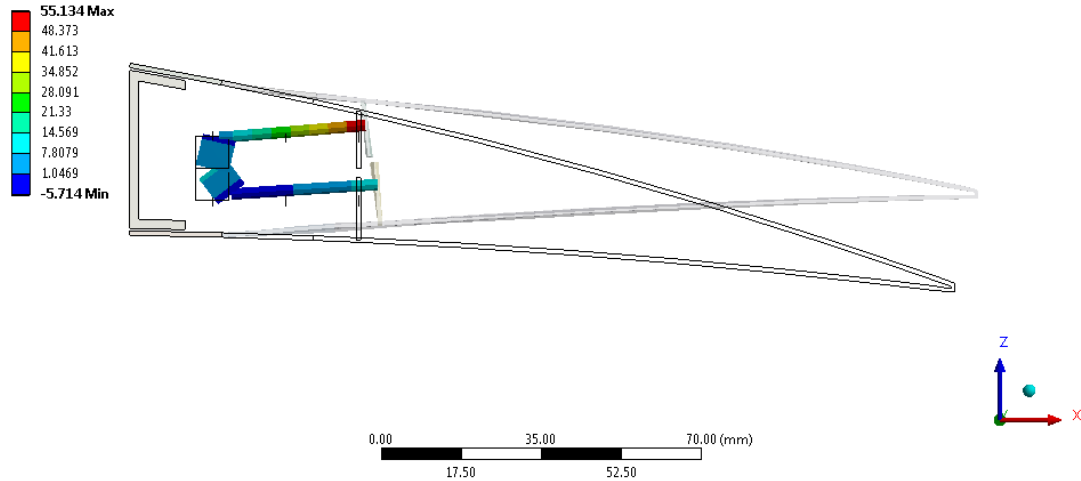


Figure 99: The Combined Beam Stresses for 20.2 [mm] Decamber of Open Cell  
Design – Servo Actuators Variation Case 1 – Maximum 55.134 [MPa]

The resulting reaction moments at moment arms are -104 [N-mm] for inboard and outboard servos to actuate the upper portion of the transmission part, -108 [N-mm] for middle servo to actuate the upper portion of the transmission part, -188 [N-mm] per servo to actuate the lower portion of the transmission part. These values are below the maximum torque limit of selected servo actuator.

#### 4.2.5.2 Case 2

In order to increase camber, approximately 15.2 [mm] downward deflection of the tip of the control surface is tried to be achieved. 19 [deg] rotation about y axis was prescribed for moment arms of servo actuators to drive the upper portion of transmission parts, and -12 [deg] rotation about y axis was prescribed for moment arms of servo actuators to drive the lower portion of transmission parts as boundary conditions.

Transverse displacement contours are shown in Figure 100. von-Mises strain distribution contours are shown in Figure 101. The combined beam stress results are shown in Figure 102.

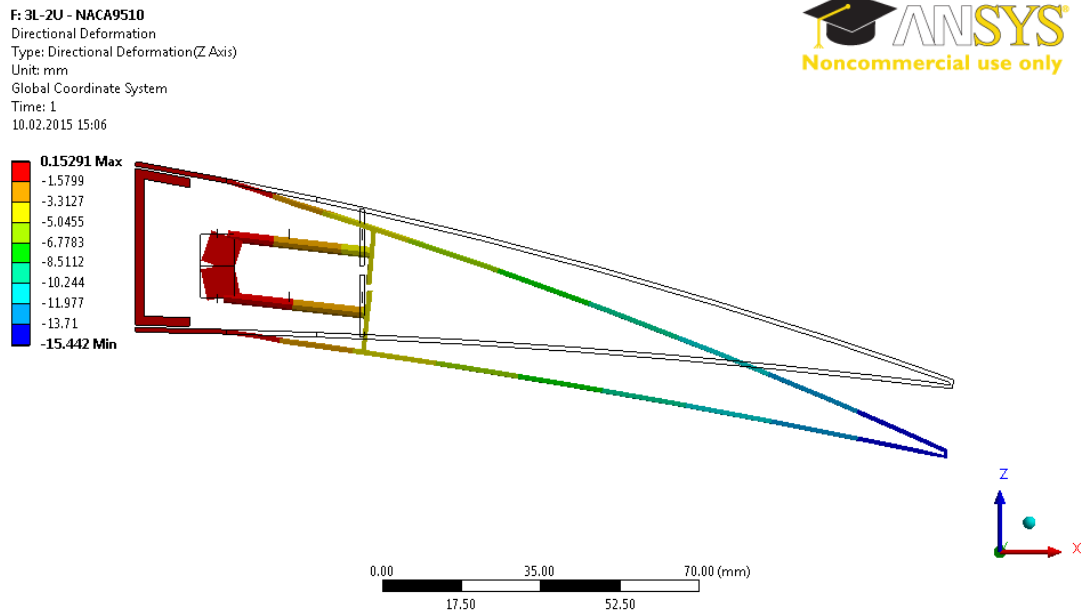


Figure 100: Transverse Displacement Contours for 15.2 [mm] Camber of Open Cell Design – Servo Actuators Variation Case 2 – Maximum 15.442 [MPa]

F: 3L-2U - NACA9510  
 Equivalent Elastic Strain 2  
 Type: Equivalent Elastic Strain - Top/Bottom - Layer 0  
 Unit: mm/mm  
 Time: 1  
 10.02.2015 15:06

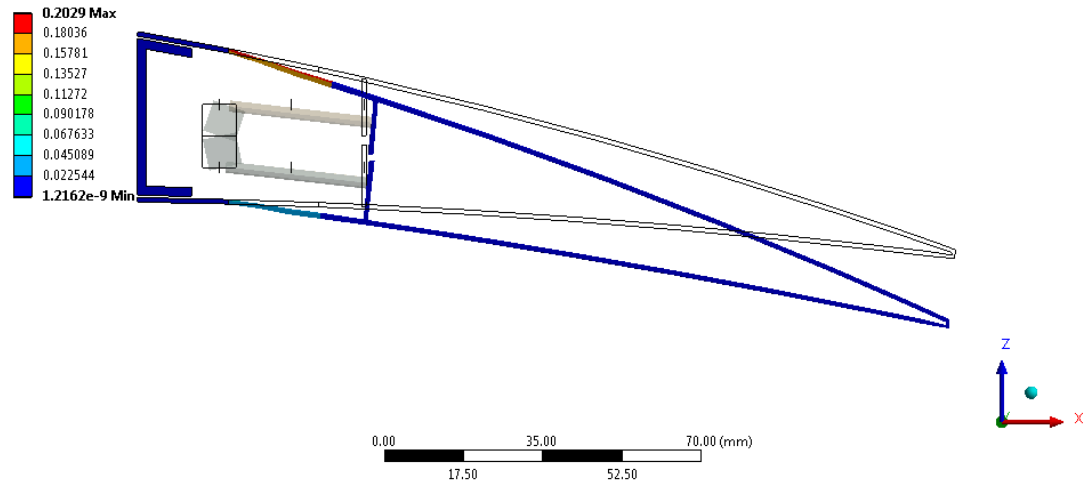


Figure 101: von-Mises Strain Distribution Contours for 15.2 [mm] Camber of Open Cell Design – Servo Actuators Variation Case 2 – Maximum 0.203 [mm/mm]

F: 3L-2U - NACA9510  
 Maximum Combined Stress  
 Type: Maximum Combined Stress - Top/Bottom - Layer 0  
 Unit: MPa  
 Time: 1  
 10.02.2015 15:06

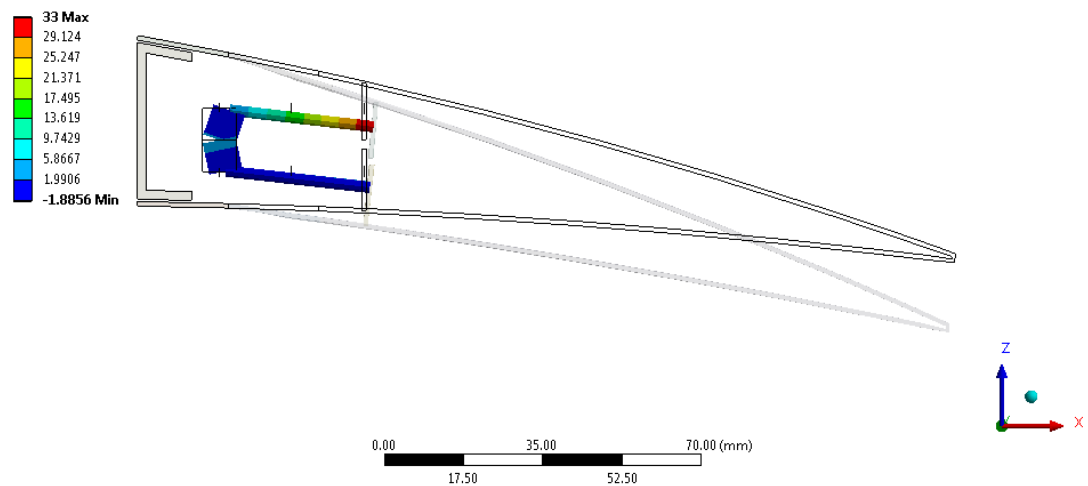


Figure 102: The Combined Beam Stresses for 15.2 [mm] Camber of Open Cell Design – Servo Actuators Variation Case 2 – Maximum 33.000 [MPa]

The resulting reaction moments at moment arms are -39 [N-mm] for servos to actuate the upper portion of the transmission part, -57 [N-mm] for inboard and outboard servos to actuate the lower portion of the transmission part, -61 [N-mm] for the middle servo to actuate the lower portion of the transmission part. These values are below the maximum torque limit of selected servo actuator.

For 15.2 [mm] upward deflection, 9 [deg] rotation about y axis was prescribed for moment arms of servo actuators to drive the upper portion of transmission parts, and -28 [deg] rotation about y axis was prescribed for moment arms of servo actuators to drive the lower portion of transmission parts as boundary conditions.

Transverse displacement contours are shown in Figure 103. von-Mises strain distribution contours are given in Figure 104. The combined beam stresses are shown in Figure 105.

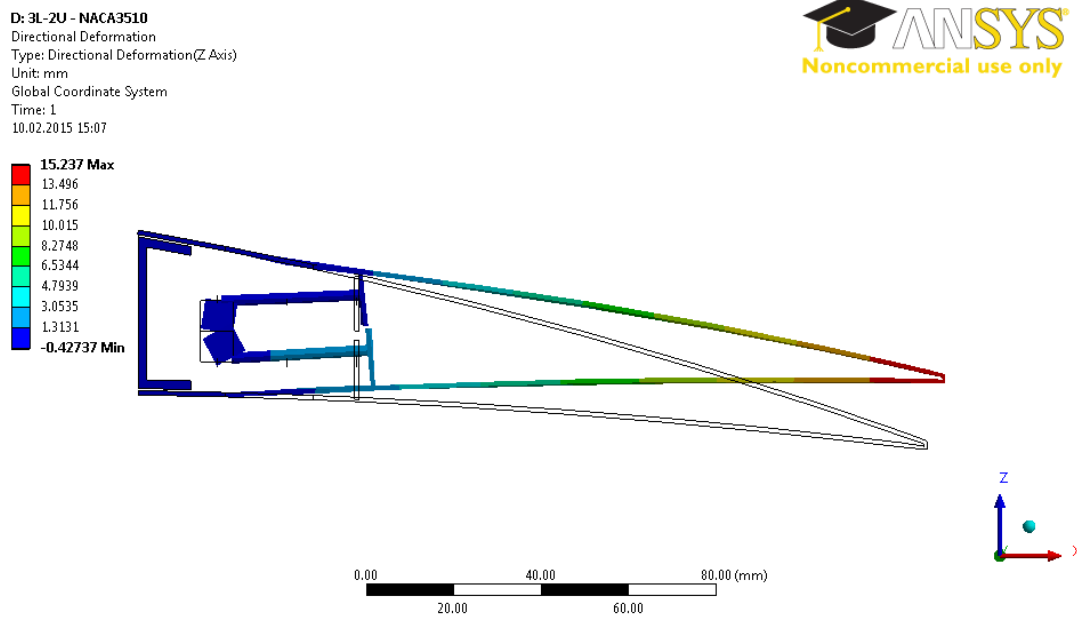


Figure 103: Transverse Displacement Contours for 15.2 [mm] Decamber of Open Cell Design – Servo Actuators Variation Case 2 – Maximum 15.237 [mm]

D: 3L-2U - NACA3510  
 Equivalent Elastic Strain 2  
 Type: Equivalent Elastic Strain - Top/Bottom - Layer 0  
 Unit: mm/mm  
 Time: 1  
 10.02.2015 15:07

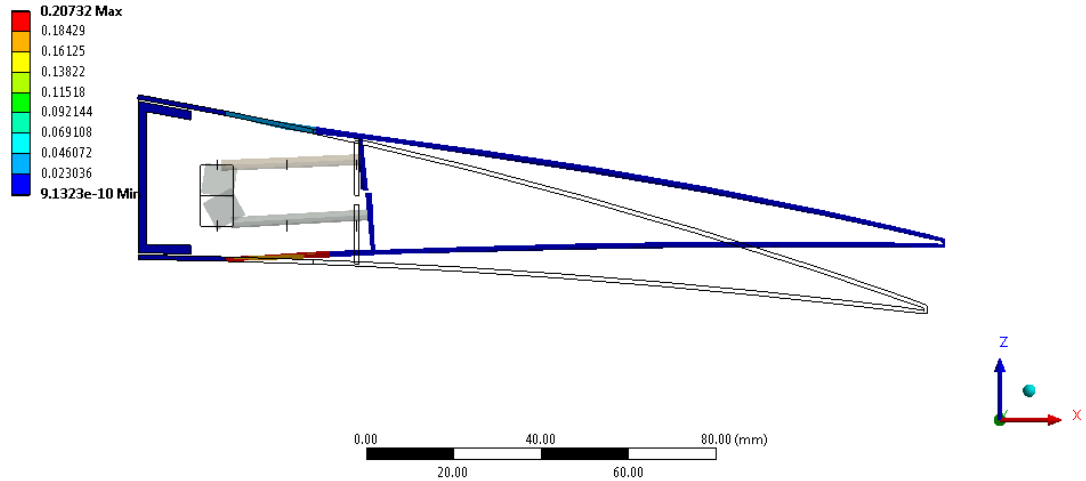


Figure 104: von-Mises Strain Distribution Contours for 15.2 [mm] Decamber of Open Cell Design – Servo Actuators Variation Case 2 – Maximum 0.207 [mm/mm]

D: 3L-2U - NACA3510  
 Maximum Combined Stress  
 Type: Maximum Combined Stress - Top/Bottom - Layer 0  
 Unit: MPa  
 Time: 1  
 10.02.2015 15:08

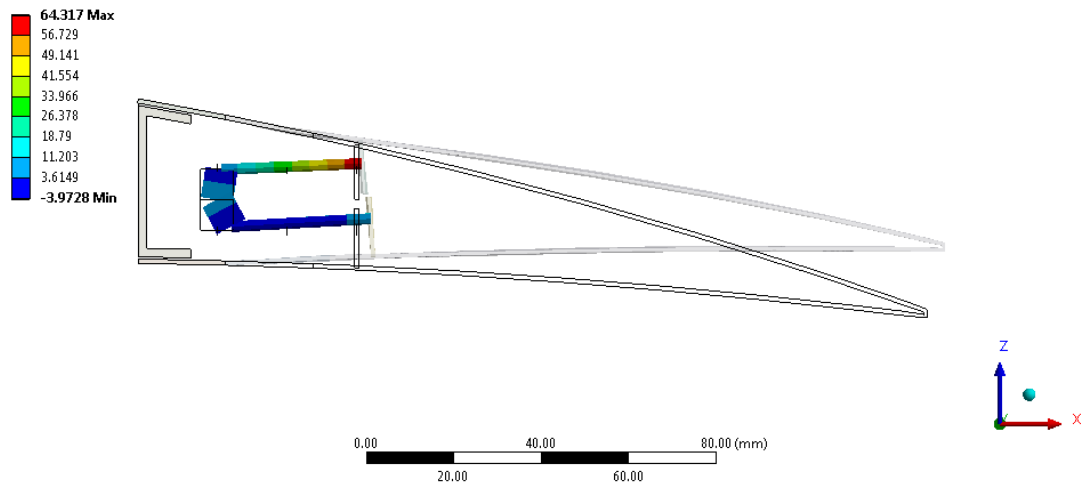


Figure 105: The Combined Beam Stresses for 15.2 [mm] Decamber of Open Cell Design – Servo Actuators Variation Case 2 – Maximum 64.317 [MPa]

The resulting reaction moments at moment arms are -142 [N-mm] per servos to actuate the upper portion of the transmission part, -118 [N-mm] for inboard and outboard servos to actuate the lower portion of the transmission part, -122 [N-mm] for the middle servo to actuate the lower portion of the transmission part. These values are below the maximum torque limit of selected servo actuator.

For 20.2 [mm] upward deflection, 10.5 [deg] rotation about y axis was prescribed for moment arms of servo actuators to drive the upper portion of transmission parts, and -34.5 [deg] rotation about y axis was prescribed for moment arms of servo actuators to drive the lower portion of transmission parts as boundary conditions.

Transverse displacement contours are shown in Figure 106. von-Mises strain distribution contours are shown in Figure 107. The combined beam stresses are shown in Figure 108.

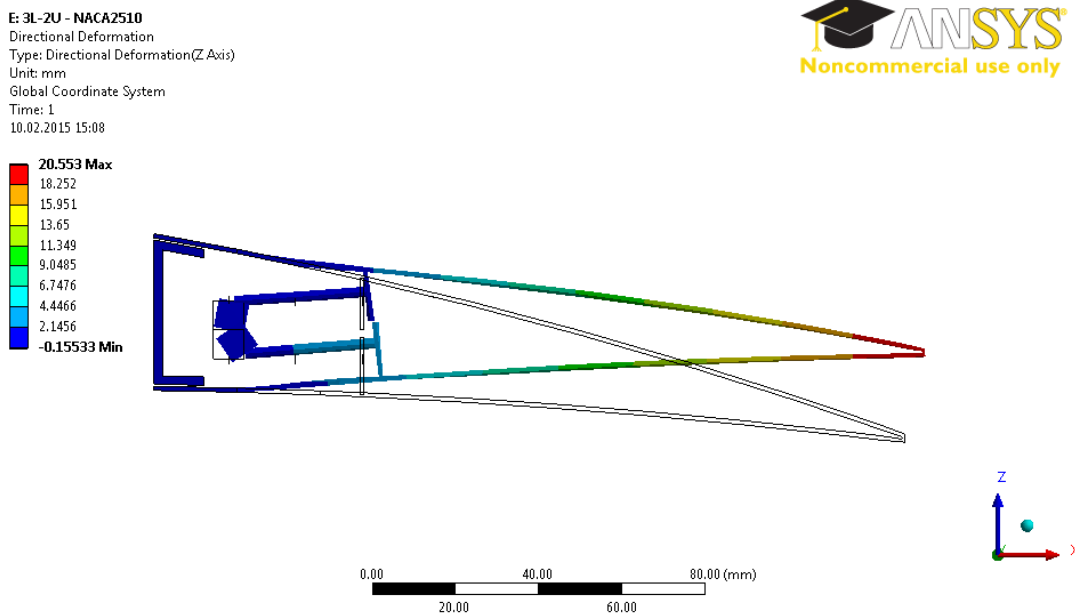


Figure 106: Transverse Displacement Contours for 20.2 [mm] Decamber of Open Cell Design – Servo Actuators Variation Case 2 – Maximum 20.553 [mm]



E: 3L-2U - NACA2510  
 Equivalent Elastic Strain 2  
 Type: Equivalent Elastic Strain - Top/Bottom - Layer 0  
 Unit: mm/mm  
 Time: 1  
 10.02.2015 15:08

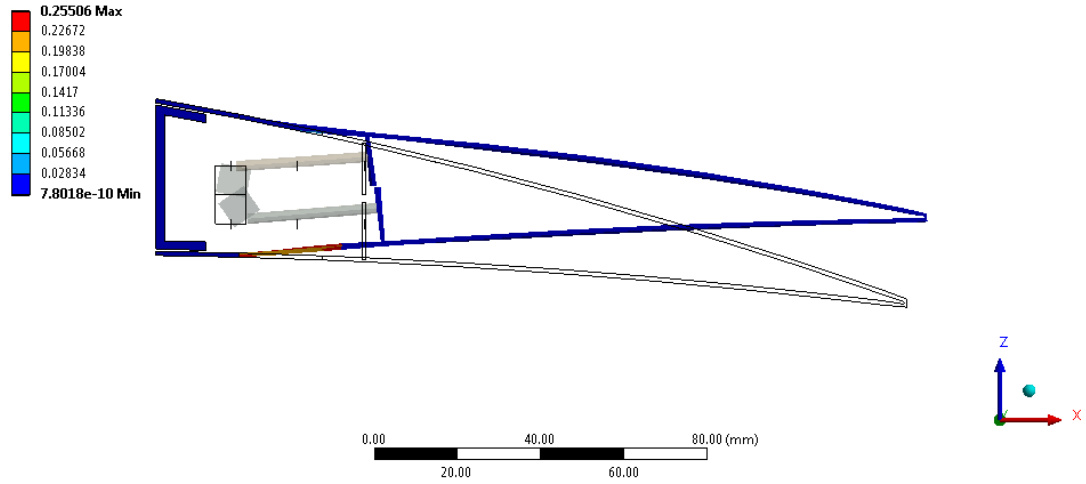


Figure 107: von-Mises Strain Distribution Contours for 20.2 [mm] Decamber of Open Cell Design – Servo Actuators Variation Case 2 – 0.255 [mm/mm]

E: 3L-2U - NACA2510  
 Maximum Combined Stress  
 Type: Maximum Combined Stress - Top/Bottom - Layer 0  
 Unit: MPa  
 Time: 1  
 10.02.2015 15:08

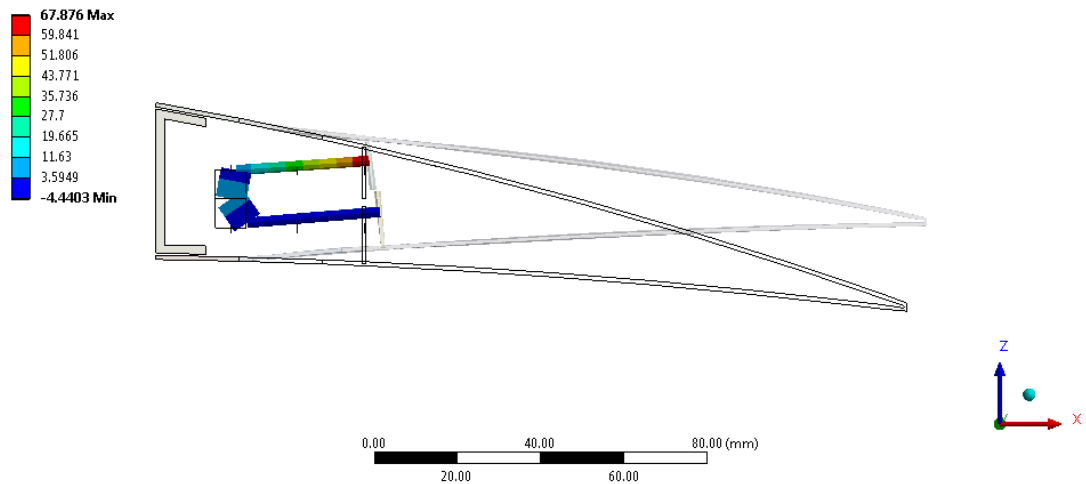


Figure 108: The Combined Beam Stresses for 20.2 [mm] Decamber of Open Cell Design – Servo Actuators Variation Case 2 – Maximum 67.876 [MPa]

The resulting reaction moments at moment arms are -157 [N-mm] per servos to actuate the upper portion of the transmission part, -126 [N-mm] for inboard and outboard servos to actuate the lower portion of the transmission part, -130 [N-mm] for the middle servo to actuate the lower portion of the transmission part. These values are below the maximum torque limit of selected servo actuator.

The results indicate that for intended further camber, it is beneficial to use three servo actuators to actuate the upper portion of transmission part and two servo actuators to actuate the lower portion of the transmission part. This configuration leads to decrease of reaction torques of servo actuators to actuate the upper portion of transmission part. In addition, beam stresses show a decreasing trend for this configuration.

For intended further decamber, it is beneficial to use two servo actuators to actuate the upper portion of the transmission part and three servo actuators to actuate the lower portion of the transmission part. This configuration leads to decrease of reaction torques of servo actuators to actuate the lower portion of the transmission part. In this configuration, maximum combined beam stresses do not alter significantly.

Since the aim of the hybrid trailing edge control surface is to perform both camber and decamber, four servo actuators configuration will be used in both open and closed cell designs.

#### **4.2.6 Analysis of Twist of Open Cell Design**

Analysis of twist of open cell design was conducted for total number of four servo actuators.

10 [deg] rotation about y axis was prescribed for servo actuators to actuate the upper portion of the transmission part, -25 [deg] rotation about y axis was prescribed for inboard servo actuator to actuate the lower portion of the transmission part and -30 [deg] rotation about y axis was prescribed for outboard servo actuator to actuate the lower portion of the transmission part as boundary conditions.

Transverse displacement contours are given in Figure 109. von-Mises strain distribution contours are shown in Figure 110. The combined beam stresses are shown in Figure 111.

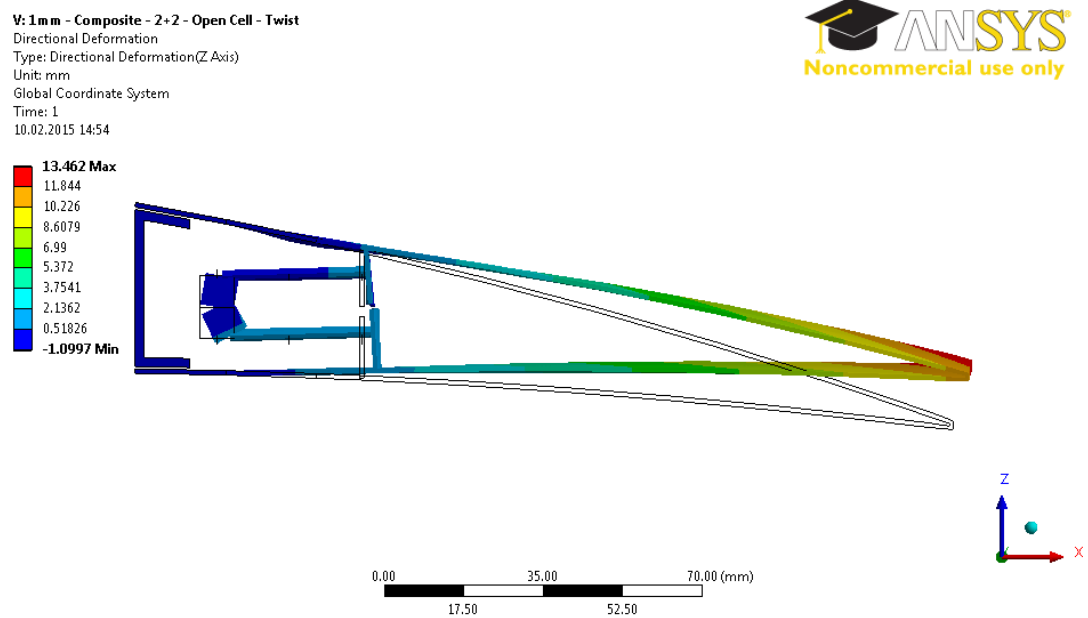


Figure 109: Transverse Displacement Contours for Twist of Open Cell Design –  
 Maximum 13.462 [mm]

V: 1 mm - Composite - 2+2 - Open Cell - Twist  
 Equivalent Elastic Strain 2  
 Type: Equivalent Elastic Strain - Top/Bottom - Layer 0  
 Unit: mm/mm  
 Time: 1  
 10.02.2015 14:54

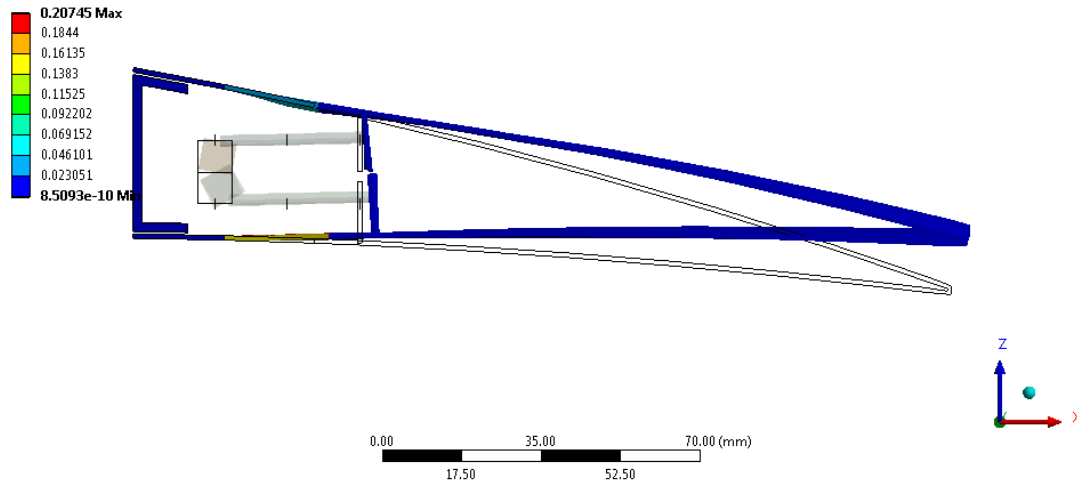


Figure 110: von-Mises Strain Distribution Contours for Twist of Open Cell Design –  
 Maximum 0.207 [mm/mm]

V: 1 mm - Composite - 2+2 - Open Cell - Twist  
 Maximum Combined Stress  
 Type: Maximum Combined Stress - Top/Bottom - Layer 0  
 Unit: MPa  
 Time: 1  
 10.02.2015 14:54

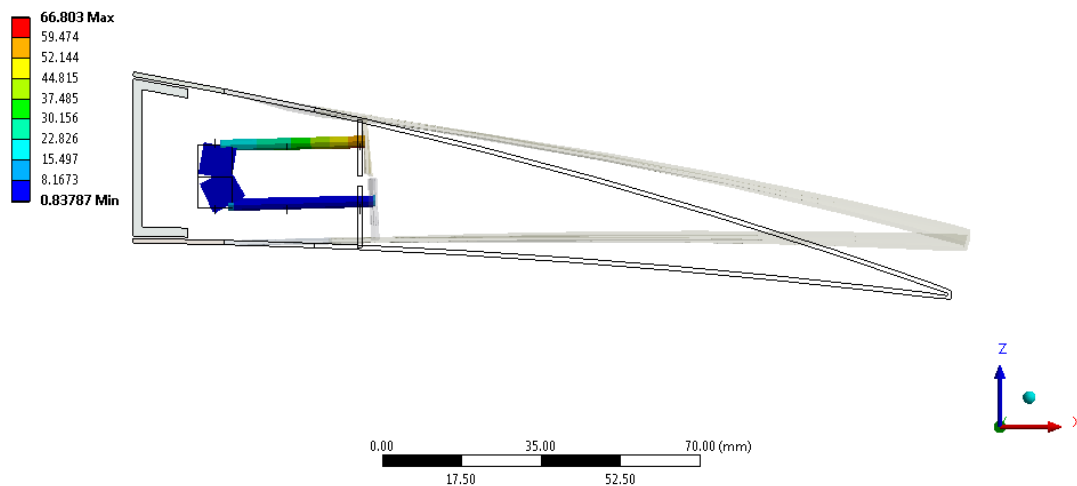


Figure 111: The Combined Beam Stresses for Twist of Open Cell Design –  
 Maximum 66.803 [MPa]

The resulting reaction moments at moment arms are -94 [N-mm] for inboard servo to actuate the upper portion of the transmission part, -168 [N-mm] for outboard servo to actuate the upper portion of the transmission part, -148 [N-mm] for inboard servo to actuate the lower portion of the transmission part and -188 [N-mm] for outboard servo to actuate the lower portion of the transmission part. These values are below the maximum torque limit of selected servo actuator.

The results indicate that the designed control surface is also capable of twist for open cell case.

### **4.3 Finite Element Analysis of Closed Cell Design in in-Vacuo Condition**

In this section, Finite Element Analysis of closed cell design is presented. The dimensions of parts of the control surface is same as in open cell design. Likewise, closed cell design is based on four servo actuators, two actuating the upper portion of the transmission part and two actuating the lower portion of the transmission part whose locations are same as in open cell design.

#### **4.3.1 Finite Element Modelling of Closed Cell Design**

The generated geometry for Finite Element Analysis of closed cell design is depicted in Figure 112.

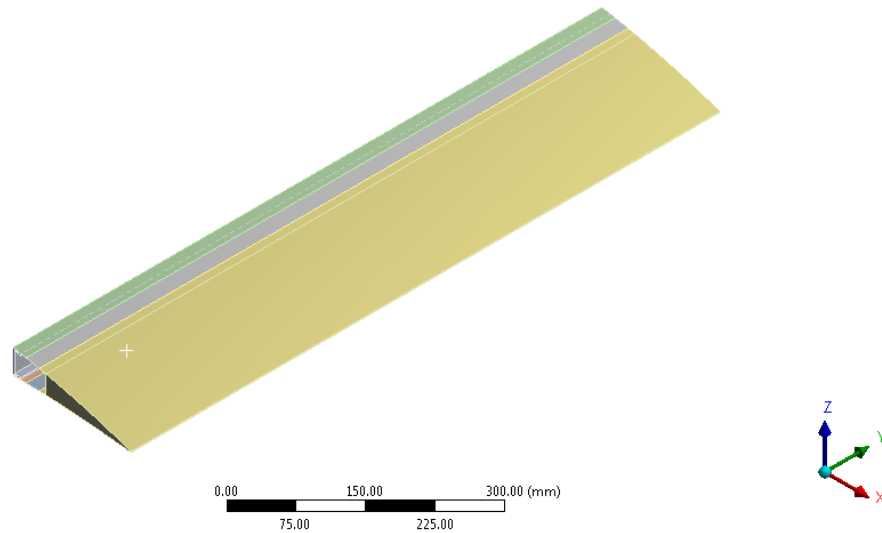


Figure 112: The Generated Geometry of Open Cell Design for Finite Element Model

Skin parts are decided to have a thickness of 1 [mm] after the analyses are conducted in the open cell case. Assigned element sizes, types and properties are the same as in open cell design. The only difference is the inclusion of the foam part. Foam part was modelled as a solid body. Therefore, 20 [mm] SOLID185 elements were used in the analysis.

Different views of the generated mesh for the closed cell case are shown in Figure 113 and Figure 114.

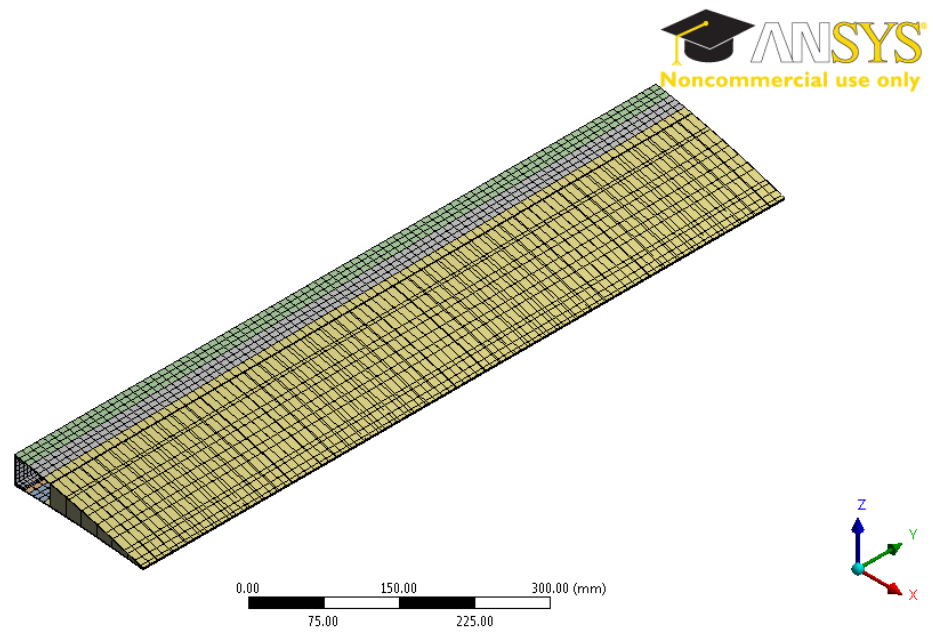


Figure 113: Isometric View of Generated Mesh for Closed Cell Design

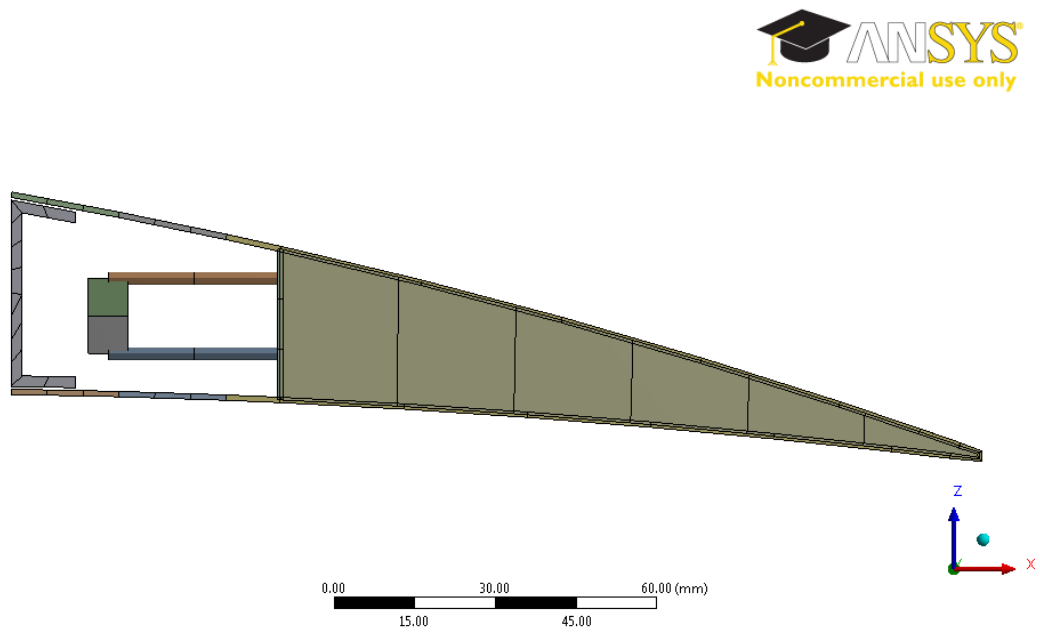


Figure 114: Side View of Generated Mesh for Closed Cell Design

Contact definitions between different parts are the same as open cell case. Additionally, another “Bonded Contact” was defined between foam part and the rigid part.

The boundary conditions are also as in open cell case. Likewise, the solution was performed with “Large Deformation” option to accommodate the non-linearities due to geometry and materials.

### **4.3.2 Analysis of Camber and Decamber Variations of Closed Cell Design**

#### **4.3.2.1 Camber Variations of Closed Cell Design**

To increase the camber of the control surface, approximately 15.2 [mm] downward tip deflection was tried to be achieved. Therefore, 22.5 [deg] rotation about y axis was prescribed for moment arms of servo actuators to drive the upper portion of transmission parts, and -12 [deg] rotation about y axis was prescribed for moment arms of servo actuators to drive the lower portion of transmission parts as boundary conditions.

Transverse displacement contours are shown in Figure 115. von-Mises strain distribution contours are shown in Figure 116. The combined beam stresses are shown in Figure 117.



F: Closed Cell - NACA9510  
 Directional Deformation  
 Type: Directional Deformation(Z Axis)  
 Unit: mm  
 Global Coordinate System  
 Time: 1  
 10.02.2015 15:11

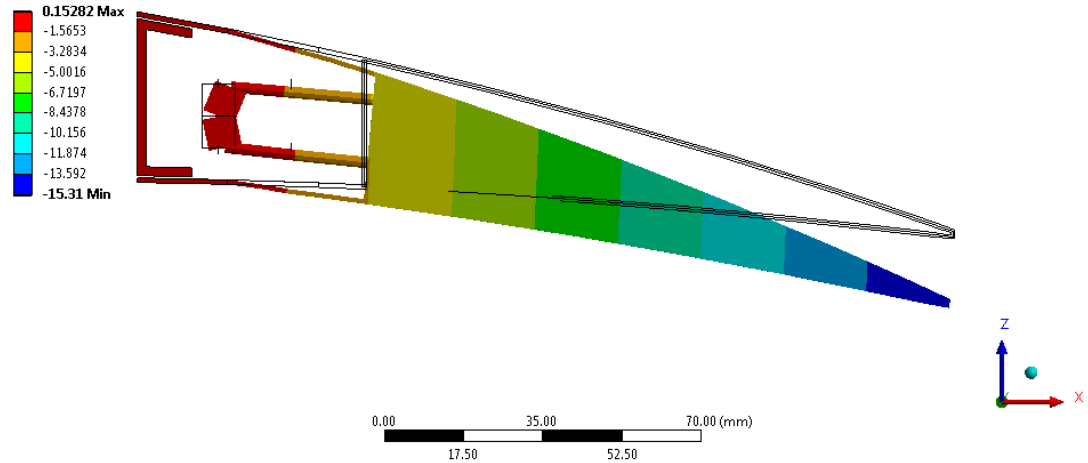


Figure 115: Transverse Displacement Contours for 15.2 [mm] Camber of Closed Cell Design – Maximum 15.310 [mm]

F: Closed Cell - NACA9510  
 Equivalent Elastic Strain 2  
 Type: Equivalent Elastic Strain - Top/Bottom - Layer 0  
 Unit: mm/mm  
 Time: 1  
 10.02.2015 15:11

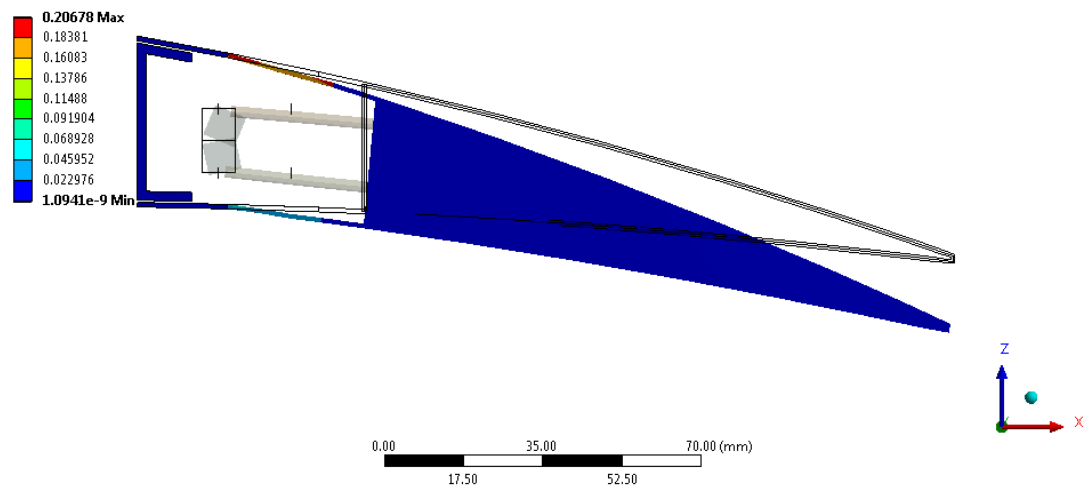


Figure 116: von-Mises Strain Distribution Contours for 15.2 [mm] Camber of Closed Cell Design – Maximum 0.207 [mm/mm]

F: Closed Cell - NACA9510  
Maximum Combined Stress  
Type: Maximum Combined Stress - Top/Bottom - Layer 0  
Unit: MPa  
Time: 1  
10.02.2015 15:12

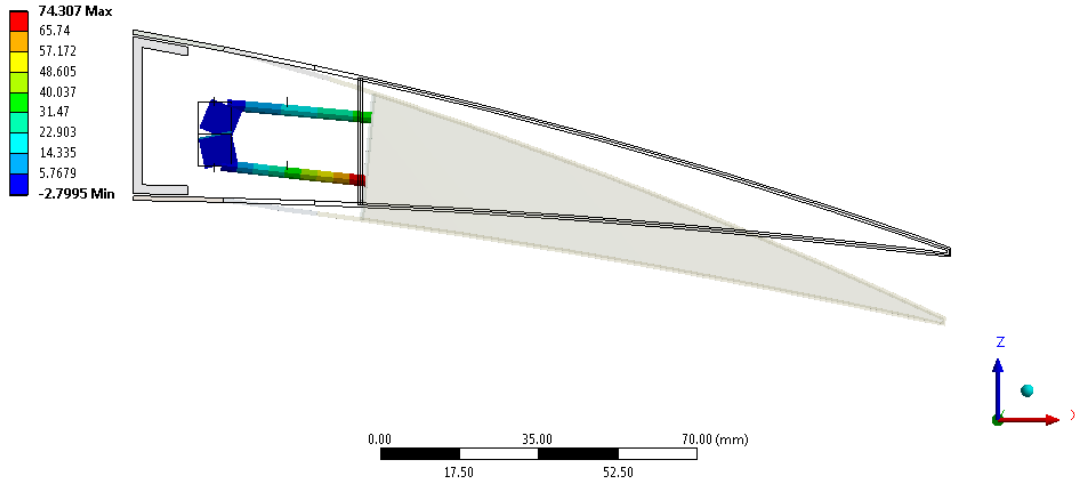


Figure 117: The Combined Beam Stresses for 15.2 [mm] Camber of Closed Cell  
Design – Maximum 74.307 [MPa]

The resulting reaction moments at moment arms are -43 [N-mm] per servo to actuate the upper portion of the transmission part, -110 [N-mm] per servo to actuate the lower portion of the transmission part. These values are below the maximum torque limit of selected servo actuator.

#### 4.3.2.2 Decamber Variations of Closed Cell Design

For 15.2 [mm] upward deflection, 12 [deg] rotation about y axis was prescribed for moment arms of servo actuators to drive the upper portion of transmission parts, and -23 [deg] rotation about y axis was prescribed for moment arms of servo actuators to drive the lower portion of transmission parts as boundary conditions.

Transverse displacement contours are shown in Figure 118. von-Mises strain distribution contours are shown in Figure 119. The combined beam stresses are shown in Figure 120.

D: Closed Cell - NACA3510  
 Directional Deformation  
 Type: Directional Deformation(Z Axis)  
 Unit: mm  
 Global Coordinate System  
 Time: 1  
 10.02.2015 15:13

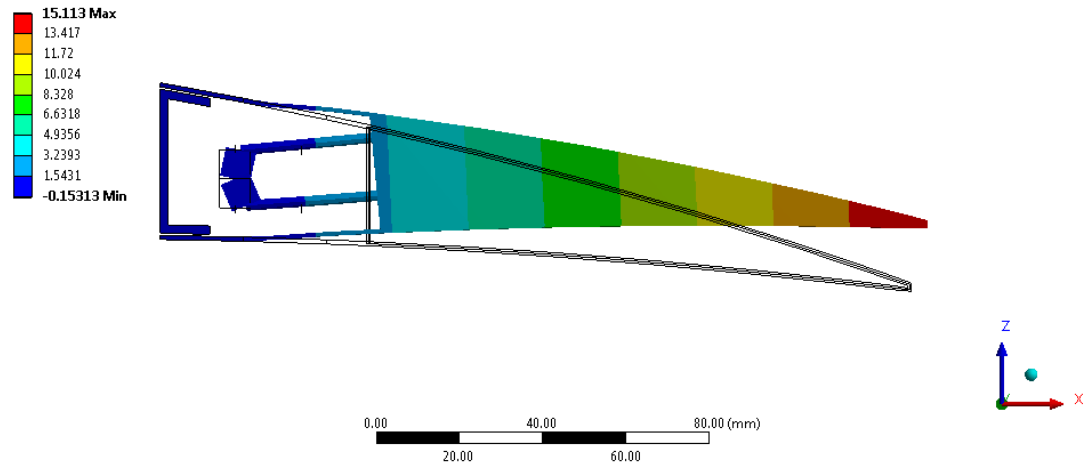


Figure 118: Transverse Displacement Contours for 15.2 [mm] Decamber of Closed Cell Design – Maximum 15.113 [mm]

D: Closed Cell - NACA3510  
 Equivalent Elastic Strain 2  
 Type: Equivalent Elastic Strain - Top/Bottom - Layer 0  
 Unit: mm/mm  
 Time: 1  
 10.02.2015 15:13

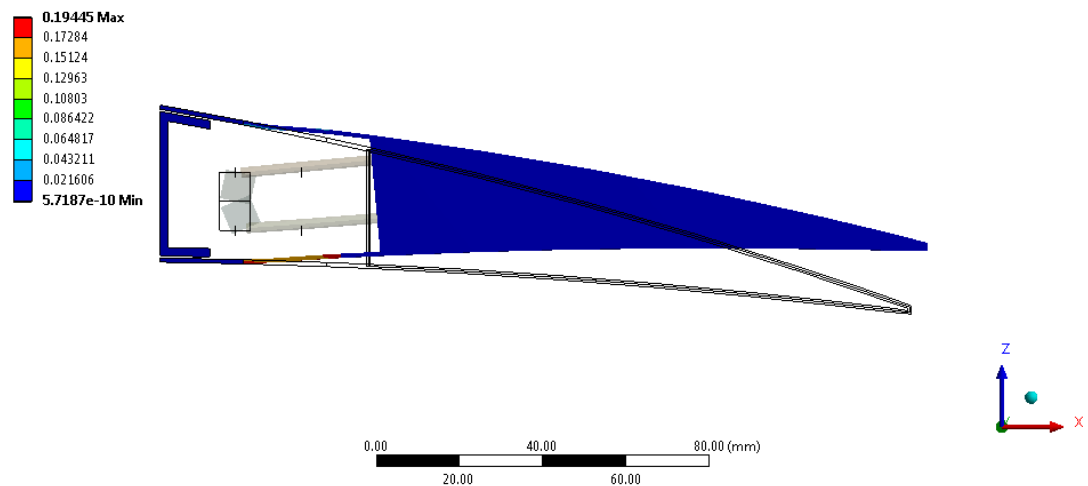


Figure 119: von-Mises Strain Distribution Contours for 15.2 [mm] Decamber of Closed Cell Design – Maximum 0.194 [mm/mm]

D: Closed Cell - NACA3510  
Maximum Combined Stress  
Type: Maximum Combined Stress - Top/Bottom - Layer 0  
Unit: MPa  
Time: 1  
10.02.2015 15:13

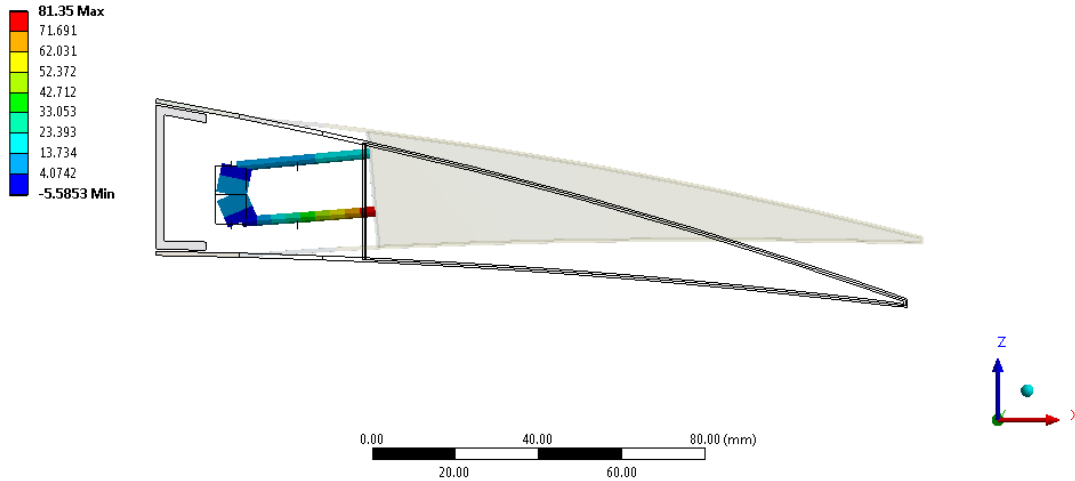


Figure 120: The Combined Beam Stresses for 15.2 [mm] Decamber of Closed Cell Design – Maximum 81.350 [MPa]

The resulting reaction moments at moment arms are -152 [N-mm] per servo to actuate the upper portion of the transmission part, -214 [N-mm] per servo to actuate the lower portion of the transmission part. These values are below the maximum torque limit of selected servo actuator.

For 20.2 [mm] upward deflection, 18 [deg] rotation about y axis was prescribed for moment arms of servo actuators to drive the upper portion of transmission parts, and -32.5 [deg] rotation about y axis was prescribed for moment arms of servo actuators to drive the lower portion of transmission parts as boundary conditions.

The transverse displacement contours are shown in Figure 121. von-Mises strain distribution contours are shown in Figure 122. The combined beam stresses are shown in Figure 123.

E: Closed Cell - NACA2510  
 Directional Deformation  
 Type: Directional Deformation(Z Axis)  
 Unit: mm  
 Global Coordinate System  
 Time: 1  
 10.02.2015 15:13

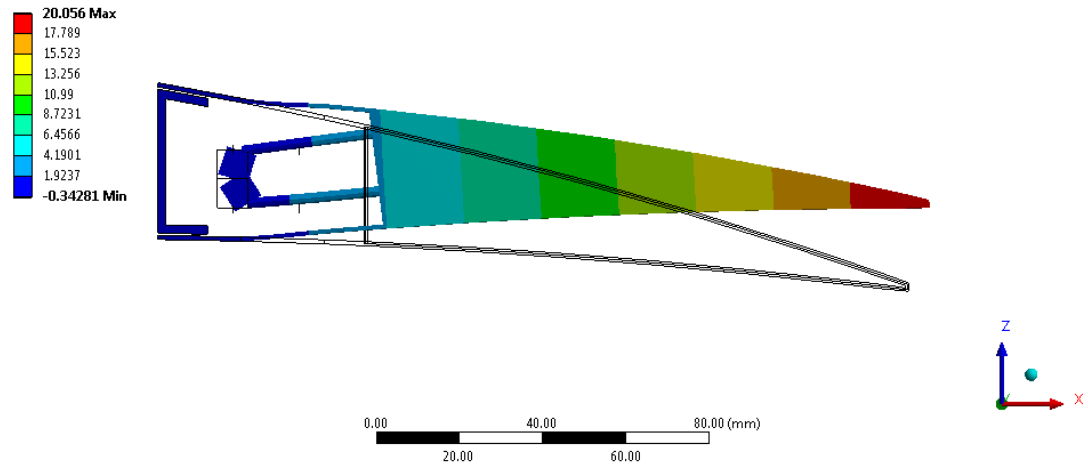


Figure 121: Transverse Displacement Contours for 20.2 [mm] Decamber of Closed Cell Design – Maximum 20.056 [mm]

E: Closed Cell - NACA2510  
 Equivalent Elastic Strain 2  
 Type: Equivalent Elastic Strain - Top/Bottom - Layer 0  
 Unit: mm/mm  
 Time: 1  
 10.02.2015 15:14

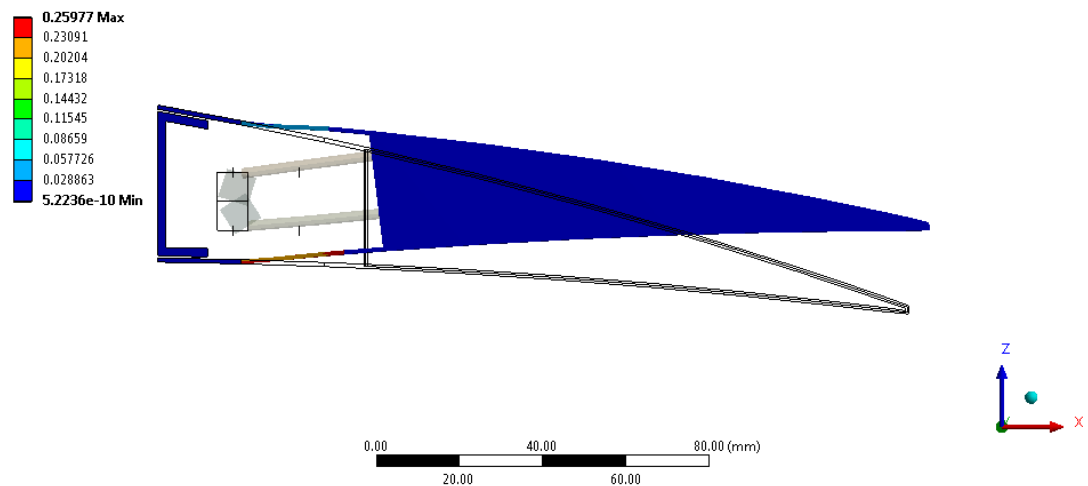


Figure 122: von-Mises Strain Distribution Contours for 20.2 [mm] Decamber of Closed Cell Design – Maximum 0.260 [mm/mm]

E: Closed Cell – NACA2510  
Maximum Combined Stress  
Type: Maximum Combined Stress - Top/Bottom - Layer 0  
Unit: MPa  
Time: 1  
10.02.2015 15:14

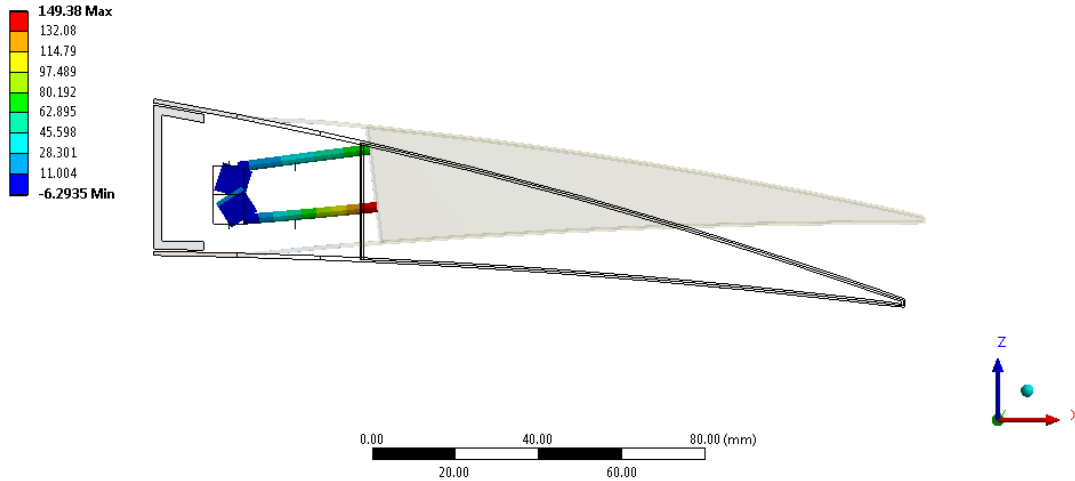


Figure 123: The Combined Beam Stresses for 20.2 [mm] Decamber of Closed Cell Design – Maximum 149.380 [MPa]

The resulting reaction moments at moment arms are -145 [N-mm] per servo to actuate the upper portion of the transmission part, -242 [N-mm] per servo to actuate the lower portion of the transmission part. These values are below the maximum torque limit of selected servo actuator.

#### 4.4 Discussion and Conclusion

In this chapter, Finite Element Analyses of the hybrid trailing edge control surface for both open and closed cell designs in in-vacuo condition were performed.

Initially, open cell design was investigated. It was shown that open cell design was capable of performing both camber and decamber for four servo actuators configuration and Aluminium Alloy was used for rigid part material. Then, composite was used for rigid part material and it was shown that this material also exhibits almost a rigid body behavior. In order to reduce the weight of the system, the rigid part's material was fixed as composite. After that, skin thicknesses were reduced from 1.5

[mm] to 1 [mm] and analyses were conducted. It was also shown for this case that system was capable of withstanding the actuation loads for cambering and decambering. Therefore, in order to reduce the weight further, skin thicknesses were fixed as 1 [mm]. The variations of servo actuators in terms of number and location were also conducted. It was also concluded that for intended further camber three servos should be used for actuation of the upper portion of the transmission part and two servos should be used for actuation of the lower portion of the transmission part. Likewise, it was concluded for intended further decamber two servos should be used for actuation of the upper portion of the transmission part and three servos should be used for actuation of the upper portion of the transmission part. These respective configurations are decreasing the required load per servo actuator. Finally, twist of open cell design was assessed and shown that open cell case can twist. The analyses of closed cell design were also conducted. It was also shown that closed cell design was capable of performing both camber and decamber.

The weight of the parts of the control surface and the total weight of the investigated designs are presented in Table 10. It was concluded that the material and the geometric variations in open cell design resulted in 0.709 [kg] weight reduction.

Table 10: Weight Comparison of Analyzed Designs in in-Vacuo Condition

	C Part [kg]	Compliant Part [kg]	Rigid Part [kg]	Servos and Equipment [kg]	Total Weight [kg]
Open Cell Design, Skin Thicknesses 1.5 [mm], Rigid Part is Aluminum	0.422	0.068	1.172	0.124	1.786
Open Cell Design, Skin Thicknesses 1.5 [mm], Rigid Part is Composite	0.422	0.068	0.804	0.124	1.418
Open Cell Design, Skin Thicknesses 1.0 [mm], Rigid Part is Composite	0.372	0.045	0.536	0.124	1.077
Open Cell Design, Skin Thicknesses 1.0 [mm], Rigid Part is Composite, Total Number of Servo Actuators is Five	0.372	0.045	0.536	0.155	1.108
Closed Cell Design, Skin Thicknesses 1.0 [mm], Rigid Part is Composite with Foam	0.372	0.045	0.632	0.124	1.173



The results of analyses are summarized in Table 11, Table 12, Table 13 and Table 14. These tables present the maximum von-Mises strains, maximum combined beam stresses and reaction moments of servo actuators in investigated design configurations.

Table 11: Maximum von-Mises Strains in Analyzed Designs in in-Vacuo Condition

	15.2 [mm] Camber Case [mm/mm]	15.2 [mm] Decamber Case [mm/mm]	20.2 [mm] Decamber Case [mm/mm]
Open Cell Design, Skin Thicknesses 1.5 [mm], Rigid Part is Aluminum	0.209	0.210	0.281
Open Cell Design, Skin Thicknesses 1.5 [mm], Rigid Part is Composite	0.205	0.212	0.282
Open Cell Design, Skin Thicknesses 1.0 [mm], Rigid Part is Composite	0.201	0.208	0.268
Closed Cell Design, Skin Thicknesses 1.0 [mm], Rigid Part is Composite with Foam	0.207	0.194	0.260

Table 12: Maximum Combined Beam Stresses in Analyzed Designs in in-Vacuo  
Condition

	15.2 [mm] Camber Case [MPa]	15.2 [mm] Decamber Case [MPa]	20.2 [mm] Decamber Case [MPa]
Open Cell Design, Skin Thicknesses 1.5 [mm], Rigid Part is Aluminum	65.905	112.650	94.691
Open Cell Design, Skin Thicknesses 1.5 [mm], Rigid Part is Composite	46.357	97.868	95.739
Open Cell Design, Skin Thicknesses 1.0 [mm], Rigid Part is Composite	34.329	67.123	69.961
Closed Cell Design, Skin Thicknesses 1.0 [mm], Rigid Part is Composite with Foam	74.307	81.350	149.380

Table 13: Reaction Moments of Servo Actuators to Actuate the Upper Portion of the Transmission Parts in Analyzed Designs in in-Vacuo Condition

	15.2 [mm] Camber Case [N-mm]	15.2 [mm] Decamber Case [N-mm]	20.2 [mm] Decamber Case [N-mm]
Open Cell Design, Skin Thicknesses 1.5 [mm], Rigid Part is Aluminum	136.170	290.830	296.260
Open Cell Design, Skin Thicknesses 1.5 [mm], Rigid Part is Composite	58.573	209.980	220.410
Open Cell Design, Skin Thicknesses 1.0 [mm], Rigid Part is Composite	39.647	143.300	156.480
Closed Cell Design, Skin Thicknesses 1.0 [mm], Rigid Part is Composite with Foam	43.348	152.220	145.370

Table 14: Reaction Moments of Servo Actuators to Actuate the Lower Portion of the Transmission Parts in Analyzed Designs in in-Vacuo Condition

	15.2 [mm] Camber Case [N-mm]	15.2 [mm] Decamber Case [N-mm]	20.2 [mm] Decamber Case [N-mm]
Open Cell Design, Skin Thicknesses 1.5 [mm], Rigid Part is Aluminum	210.990	357.250	378.730
Open Cell Design, Skin Thicknesses 1.5 [mm], Rigid Part is Composite	132.770	271.500	287.530
Open Cell Design, Skin Thicknesses 1.0 [mm], Rigid Part is Composite	86.246	177.800	185.620
Closed Cell Design, Skin Thicknesses 1.0 [mm], Rigid Part is Composite with Foam	110.400	213.540	241.550

The comparison of reaction moments of servo actuators in designs of servo actuator variations are presented in Table 15 and Table 16 along with the design having total number of four servo actuators.

Table 15: Comparison of Averaged Reaction Moments of Servo Actuators to Actuate the Upper Portion of the Transmission Parts in Designs of Servo Actuator Variations

	15.2 [mm] Camber Case [N-mm]	15.2 [mm] Decamber Case [N-mm]	20.2 [mm] Decamber Case [N-mm]
Open Cell Design, Skin Thicknesses 1.0 [mm], Rigid Part is Composite	39.647	143.300	156.480
Open Cell Design, Skin Thicknesses 1.0 [mm], Rigid Part is Composite, Servo Actuator Variations Case 1	26.721	96.246	105.663
Open Cell Design, Skin Thicknesses 1.0 [mm], Rigid Part is Composite, Servo Actuator Variations Case 2	38.932	141.750	156.710

Table 16: Comparison of Averaged Reaction Moments of Servo Actuators to Actuate the Lower Portion of the Transmission Parts in Designs of Servo Actuator Variations

	15.2 [mm] Camber Case [N-mm]	15.2 [mm] Decamber Case [N-mm]	20.2 [mm] Decamber Case [N-mm]
Open Cell Design, Skin Thicknesses 1.0 [mm], Rigid Part is Composite	86.246	177.800	185.620
Open Cell Design, Skin Thicknesses 1.0 [mm], Rigid Part is Composite, Servo Actuator Variations Case 1	86.388	177.980	187.580
Open Cell Design, Skin Thicknesses 1.0 [mm], Rigid Part is Composite, Servo Actuator Variations Case 2	57.943	119.543	127.747

It can be concluded from Table 15 and Table 16 that the reaction moments of the servo actuators necessary to actuate the upper portion of the transmission parts decrease if one uses the servo actuator variations case 1, in which, the total number of servo actuators in order to actuate the upper portion of the transmission parts was increased from two to three. Since the number of servo actuators actuating the lower portion of the transmission part was not altered in this case, the reaction moments are almost same as in the design having total number of four servo actuators, which is given in the first row of Table 15 and Table 16. Likewise, the reaction moments of the servo actuators necessary to actuate the lower portion of the transmission parts

decrease if one uses servo actuator variations case 2, in which, the total number of servo actuators in order to actuate the lower portion of the transmission parts was increased from two to three. Since the number of servo actuators actuating the upper portion of the transmission part was not altered in this case, the reaction moments are almost same as in design having total number of four servo actuators, which is given in the first row of Table 15 and Table 16. Therefore, it can be deduced that for intended further camber, case 1 can be used since the load required per servo actuator decreases. Similarly, for intended further decamber, case 2 can be used due to same reasons.





## **CHAPTER 5**

### **FINITE ELEMENT ANALYSIS OF THE HYBRID TRAILING EDGE CONTROL SURFACE UNDER AERODYNAMIC LOADING**

#### **5.1 Introduction**

In this chapter, the hybrid trailing edge control surface is analyzed structurally under aerodynamic loading to determine the effects of aerodynamic loads on the control surface.

In the first part of the chapter, the details of aerodynamic analyses are presented. In the second part, open cell and closed cell designs are assessed under aerodynamic loading for both camber and decamber variations. Finally, the conclusions drawn from the analyses are presented.

#### **5.2 Aerodynamic Analyses**

Since the main aim of the thesis is to show the capability of camber and decamber morphings of the hybrid trailing edge control surface both in in-vacuo condition and under aerodynamic loading, only take-off, cruise or high speed dash and landing phases, in which morphing characteristics are required, were analyzed.

Using the obtained morphing results in in-vacuo condition, CAD models of the morphed wing in different flight phases were generated to be used in aerodynamic analyses by using CATIA V5-6R2012 package program. The aerodynamic analyses were conducted by using Computational Fluid Dynamics. Initially, an aerodynamic mesh was generated over the wing, and then outer domain was generated. Then, by using the respective flight parameters solutions were performed.

### 5.2.1 Aerodynamic Mesh

The aerodynamic mesh was generated by using Pointwise® V17.2R2 package program. The generated mesh has following properties:

- Element sizes are 8 [mm],
- Leading and trailing edge portions of the wing have finer mesh,
- Outer domain is hemisphere having radius of 20 times the chord value,
- In order to model the boundary layer over the wing, T-Rex meshing method is employed.

Mesh over the wing shown in Figure 124, boundary layer mesh illustrated in Figure 125 and outer domain mesh depicted in Figure 126.

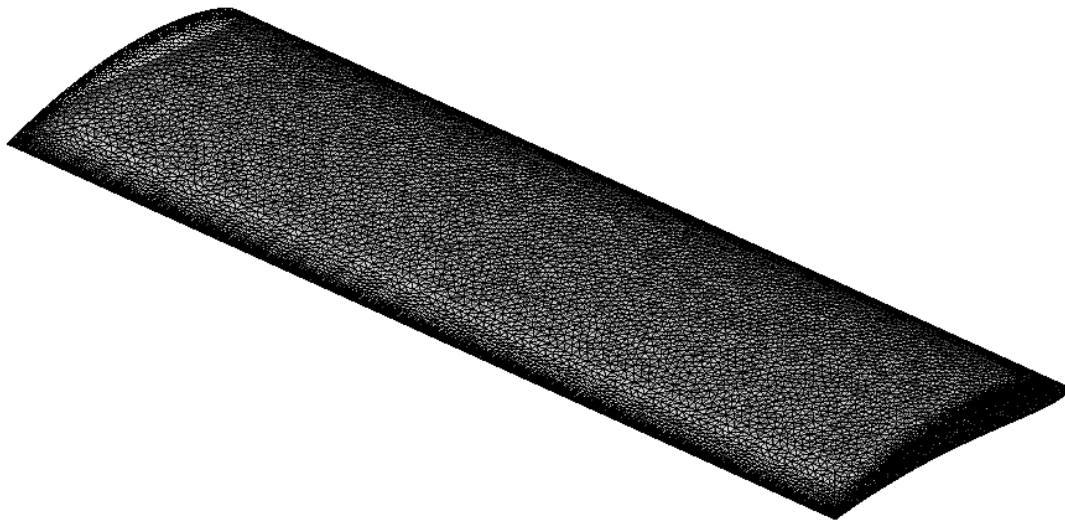


Figure 124: Generated Aerodynamic Mesh over the Wing

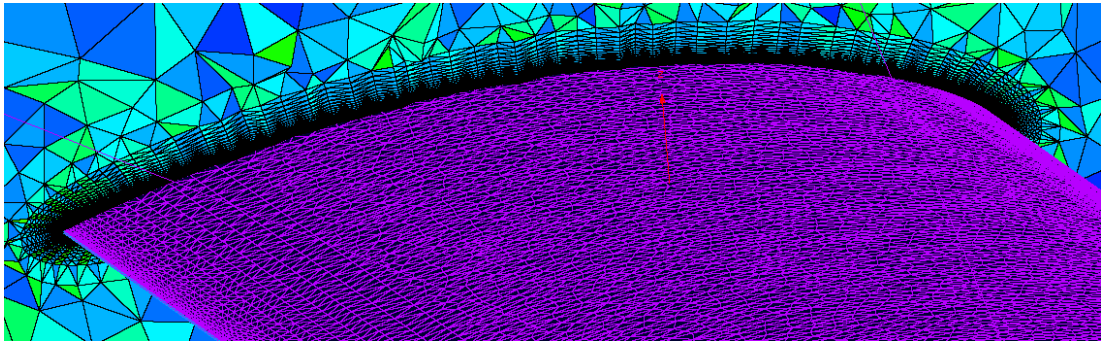


Figure 125: Generated Boundary Layer Mesh over the Wing Surface

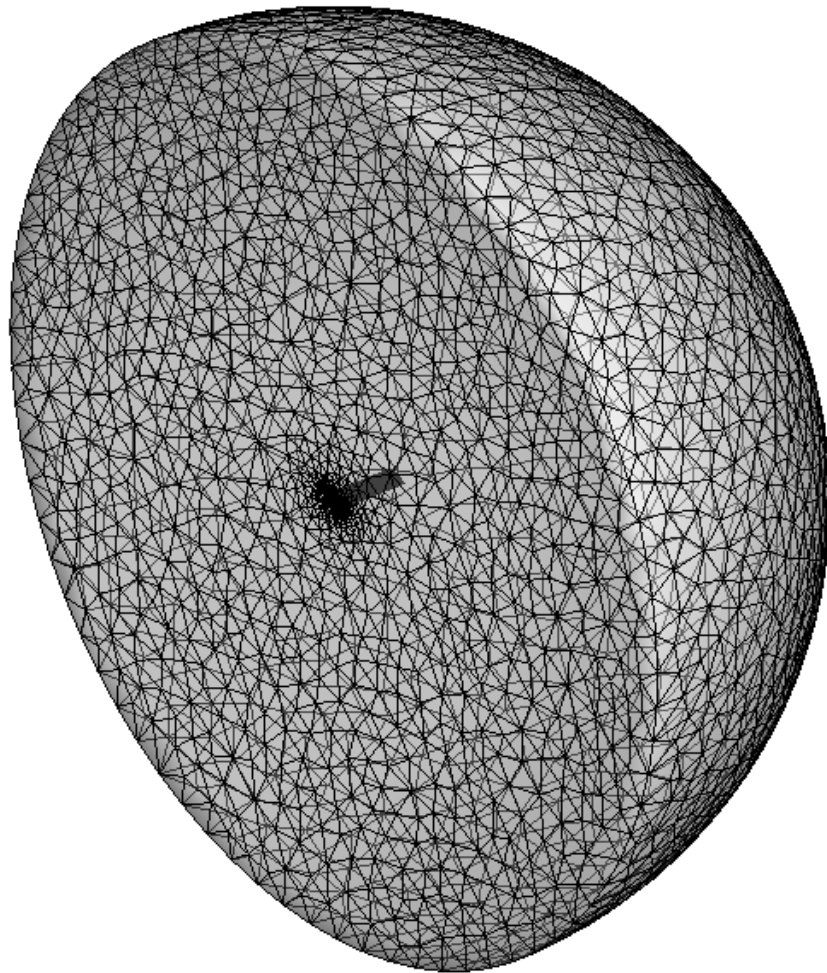


Figure 126: Generated Hemisphere Outer Domain Mesh

### 5.2.2 Computational Fluid Dynamics Analyses

Computational Fluid Dynamics (CFD) analyses were conducted by using Stanford University Unstructured (SU2) V3.2.1 open-source software, which was used as a solver. The SU2 CFD simulation requires both configuration file and the mesh file as its inputs. The former input was prepared according to flight parameters, and the latter input was generated directly by Pointwise® V17.2R2 package program.

The flight parameters defined to the solver are presented in Table 17. It must be noted that these flight parameters correspond to 1g flight condition. In other words, maneuvers at which the higher load factors occur, were not considered within the scope of this thesis.

Table 17: The Flight Parameters used in Aerodynamic Analyses

	Landing Phase	Take-off Phase	Cruise or High Speed Dash Phase
Flight Speed [m/s]	13.244	21.152	30.556
Angle of Attack [deg]	6.373	1.713	1.056
Reynolds Number	524536	857990	1210135
Density [kg/m <sup>3</sup> ]	1.189	1.225	1.189
Mach Number	0.039	0.063	0.090
Altitude [ft]	1000	0	1000

As it can be seen from Table 17, Mach number for each flight phase is very low. Therefore, incompressible flow was considered to be the case in the CFD analyses. Additionally, the flow was assumed to be viscous during modelling. This viscous flow was modelled by using Reynolds Averaged Navier-Stokes (RANS)

equations equipped with Spallart-Almaras Turbulence modelling. As a result, the flow was modelled as incompressible RANS in the CFD analysis.

The pressure distribution over the wing, and especially over the control surface were sought in order to determine the effects of aerodynamic loads. Additionally, the viscous forces should be taken into account. However, it was seen from the results of the analyses that the viscous forces were very small, and therefore, were neglected during the structural analyses. The obtained pressure distributions were applied to the structural mesh in Finite Element Analyses, and these distributions are presented in following sections.

### **5.3 Finite Element Analysis of Open Cell Design Under Aerodynamic Loading**

#### **5.3.1 Finite Element Modelling of Open Cell Design**

The finite element modelling of open cell design under aerodynamic loading is the same as explained in Chapter 4. In this chapter, due to aerodynamic loading, additional boundary condition was applied as pressure to the skin parts of the hybrid trailing edge control surface. ANSYS automatically maps the aerodynamic mesh on the structural mesh, and transfers the aerodynamic loads to the structural mesh nodes [34]. The applied boundary conditions are shown in Figure 127.

X: 1 mm - Composite - 2+2 - Open Cell - NACA3510  
 Static Structural  
 Time: 1. s  
 10.02.2015 15:21

- A Fixed Support
- B Standard Earth Gravity: 9806.6 mm/s<sup>2</sup>
- C Remote Displacement
- D Remote Displacement 2
- E Remote Displacement 3
- F Remote Displacement 4
- G Imported Pressure

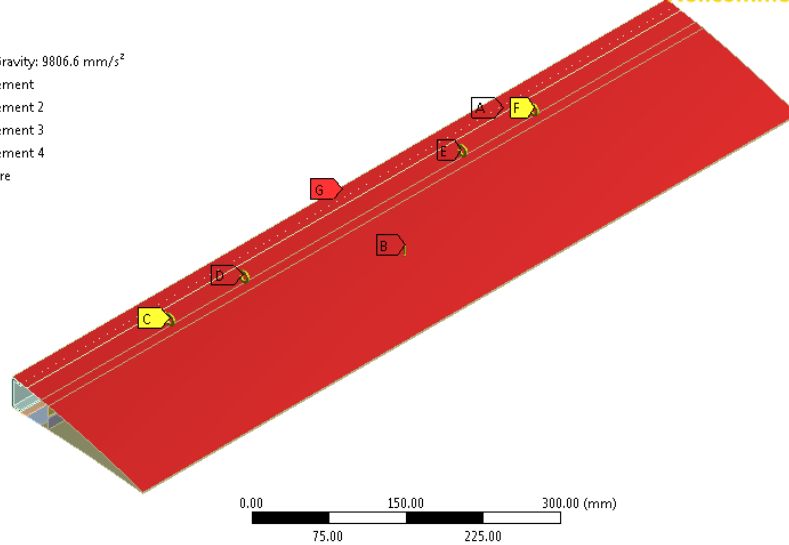


Figure 127: Applied Boundary Conditions to Open Cell Design under Aerodynamic Loading

### 5.3.2 Analysis of Camber and Decamber Variations of Open Cell Design

It is mentioned in Chapter 4 that for camber increase, approximately 15.2 [mm] transverse downward tip deflection was tried to be achieved. Then, based on the achieved profile, aerodynamic calculations were made and applied to the structure. Aerodynamic loads applied to upper and lower parts of the control surface for 15.2 [mm] camber increase case are shown in Figure 128 and Figure 129.

AD: 1mm - Composite - 2+2 - Open Cell - NACA9510  
 Imported Pressure  
 Unit: MPa  
 10.02.2015 15:25

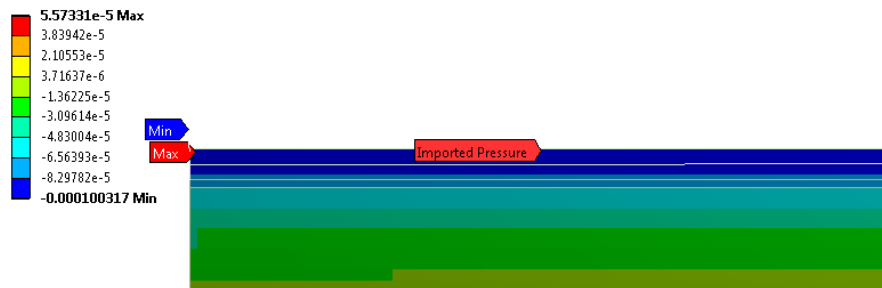


Figure 128: Pressure Contours of Applied Aerodynamic Loading for 15.2 [mm]  
 Camber – Upper Surface

AD: 1mm - Composite - 2+2 - Open Cell - NACA9510  
 Imported Pressure  
 Unit: MPa  
 10.02.2015 15:25

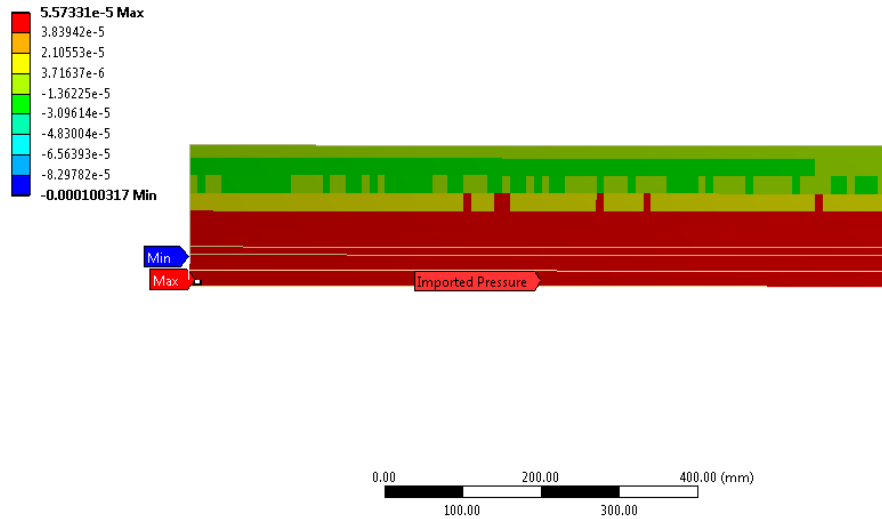


Figure 129: Pressure Contours of Applied Aerodynamic Loading for 15.2 [mm]  
 Camber – Lower Surface

In order to hold the control surface at same tip deflection, rotation boundary conditions were applied as in in-vacuo cases. Therefore, 25 [deg] rotation about y axis was prescribed for moment arms of servo actuators to drive the upper portion of transmission parts, and -11 [deg] rotation about y axis was prescribed for moment arms of servo actuators to drive the lower portion of transmission parts as boundary conditions. Transverse displacement contours are shown in Figure 130.

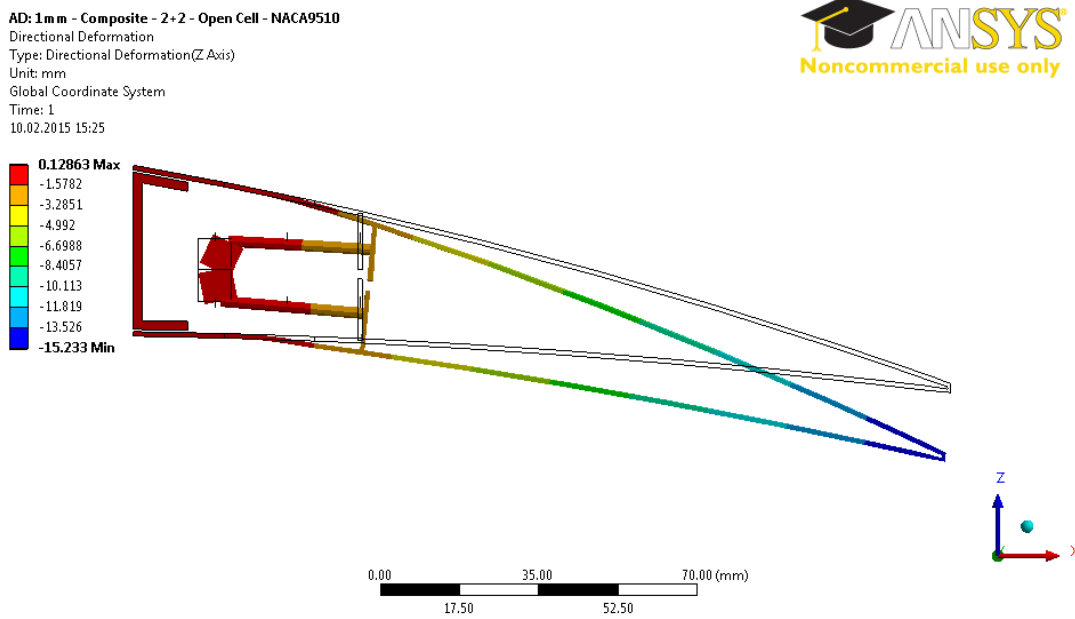


Figure 130: Transverse Displacement Contours for 15.2 [mm] Camber of Open Cell Design Under Aerodynamic Loading – Maximum 15.233 [mm]

The calculated aerodynamic loads for 15.2 [mm] decamber case are shown in Figure 131 and Figure 132.



X: 1mm - Composite - 2+2 - Open Cell - NACA3510  
 Imported Pressure  
 Unit: MPa  
 10.02.2015 15:22

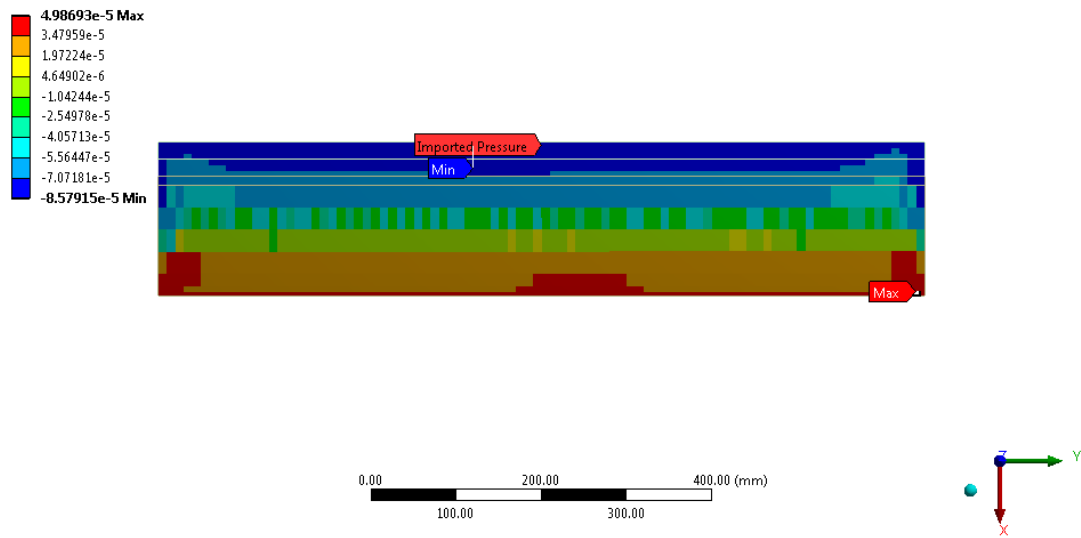


Figure 131: Pressure Contours of Applied Aerodynamic Loading for 15.2 [mm]  
 Decamber – Upper Surface

X: 1mm - Composite - 2+2 - Open Cell - NACA3510  
 Imported Pressure  
 Unit: MPa  
 10.02.2015 15:22

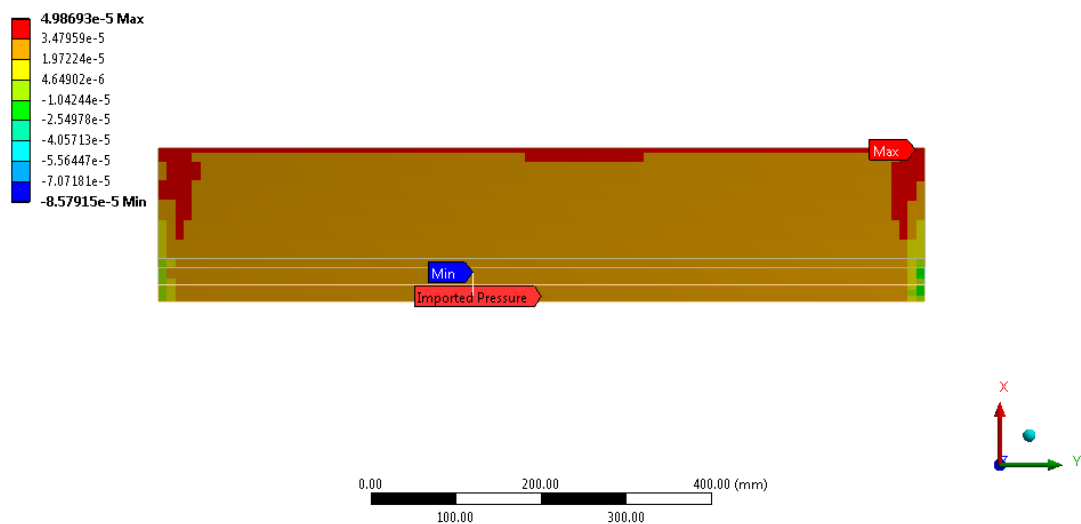


Figure 132: Pressure Contours of Applied Aerodynamic Loading for 15.2 [mm]  
 Decamber – Lower Surface

In order to hold the control surface at same tip deflection, rotation boundary conditions were applied as in in-vacuo cases. Therefore, 14 [deg] rotation about y axis was prescribed for moment arms of servo actuators to drive the upper portion of transmission parts, and -29 [deg] rotation about y axis was prescribed for moment arms of servo actuators to drive the lower portion of transmission parts as boundary conditions. Transverse displacement contours are shown in Figure 133.

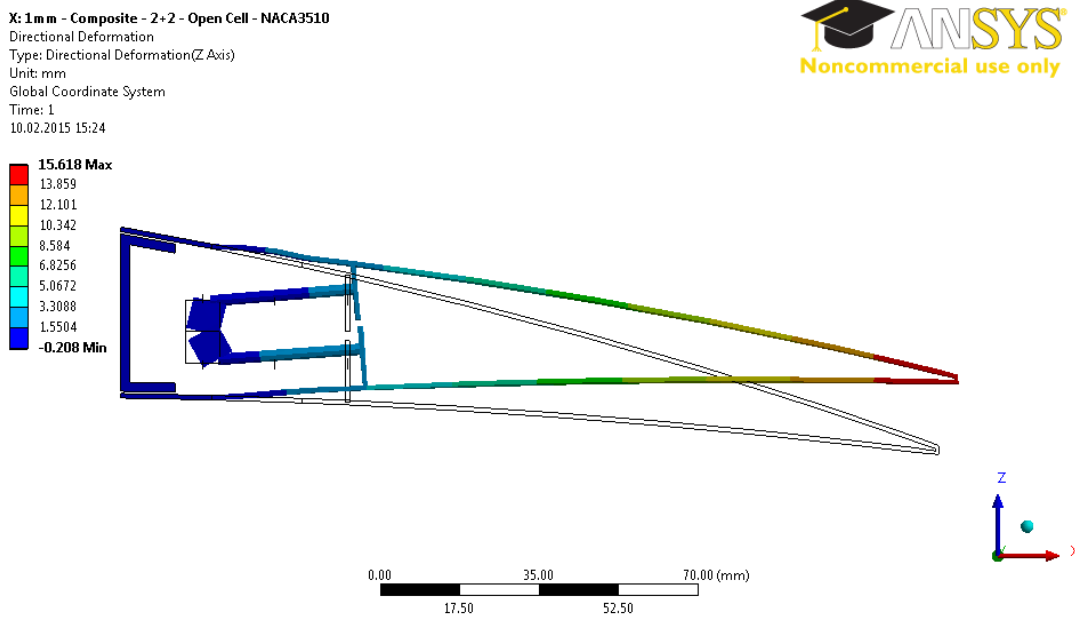


Figure 133: Transverse Displacement Contours for 15.2 [mm] Decamber of Open Cell Design Under Aerodynamic Loading – Maximum 15.618 [mm]

As it can be seen from Figure 133 that upper compliant skin shows capping under aerodynamic loading, which is a problem for airflow over the control surface.

The calculated aerodynamic loads for 20.2 [mm] decamber case are shown in Figure 134 and Figure 135.

AB: 1.5 mm - Composite - 2+2 - Open Cell - NACA2510  
 Imported Pressure  
 Unit: MPa  
 10.02.2015 15:27

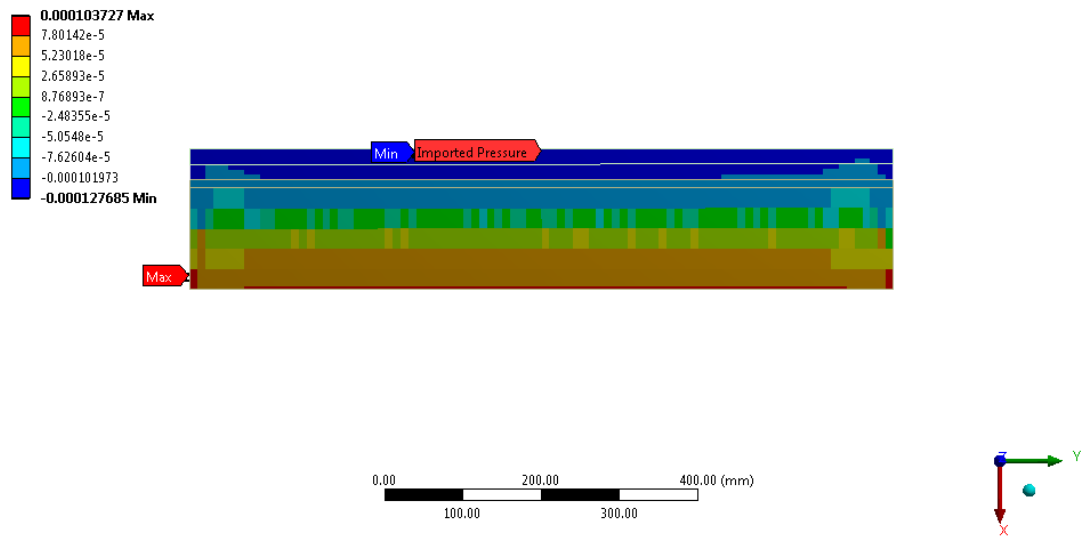


Figure 134: Pressure Contours of Applied Aerodynamic Loading for 20.2 [mm]  
 Decamber – Upper Surface

AB: 1.5 mm - Composite - 2+2 - Open Cell - NACA2510  
 Imported Pressure  
 Unit: MPa  
 10.02.2015 15:27

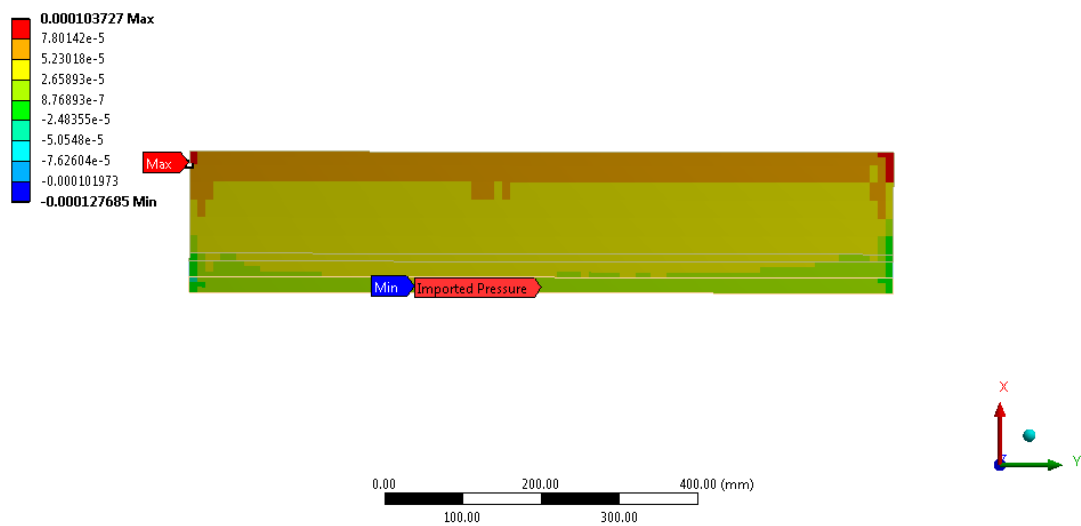


Figure 135: Pressure Contours of Applied Aerodynamic Loading for 20.2 [mm]  
 Decamber – Lower Surface

In order to hold the control surface at same tip deflection, rotation boundary conditions were applied as in in-vacuo cases. However, solution could not be achieved due the capping of upper compliant skin, which lead to excessive deformation of elements and results in unconverged solution.

Although, in in-vacuo analysis, 1 [mm] skin thickness cases showed a good performance, the same is not true for under aerodynamic loading cases. Hence, to eliminate the capping of the compliant surface and to obtain converged solutions, skin thicknesses were increased to 1.5 [mm]. Then, analysis were performed again to assess the system under aerodynamic loading.

In order to hold the control surface for 15.2 [mm] camber, rotation boundary conditions were applied as in in-vacuo cases. Therefore, 22 [deg] rotation about y axis was prescribed for moment arms of servo actuators to drive the upper portion of transmission parts, and -11 [deg] rotation about y axis was prescribed for moment arms of servo actuators to drive the lower portion of transmission parts as boundary conditions.

Transverse displacement contours are shown in Figure 136. von-Mises strain distribution contours are shown in Figure 137. The combined beam stresses are shown in Figure 138.

AE: 1.5 mm - Composite - 2+2 - Open Cell - NACA9510  
 Directional Deformation  
 Type: Directional Deformation(Z Axis)  
 Unit: mm  
 Global Coordinate System  
 Time: 1  
 10.02.2015 15:28

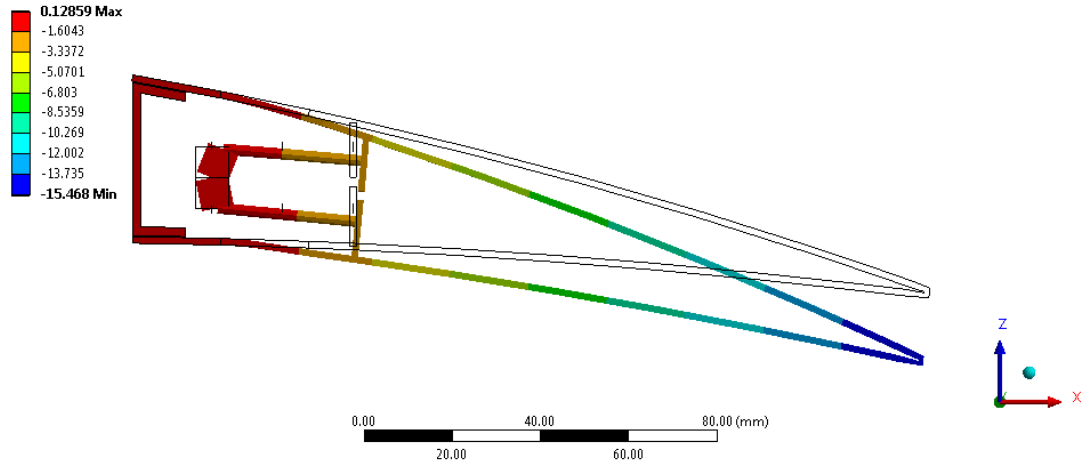


Figure 136: Transverse Displacement Contours for 15.2 [mm] Camber of Open Cell Design Under Aerodynamic Loading – Skin Thicknesses are 1.5 [mm] – Maximum 15.468 [mm]

AE: 1.5 mm - Composite - 2+2 - Open Cell - NACA9510  
 Equivalent Elastic Strain 2  
 Type: Equivalent Elastic Strain - Top/Bottom - Layer 0  
 Unit: mm/mm  
 Time: 1  
 10.02.2015 15:28

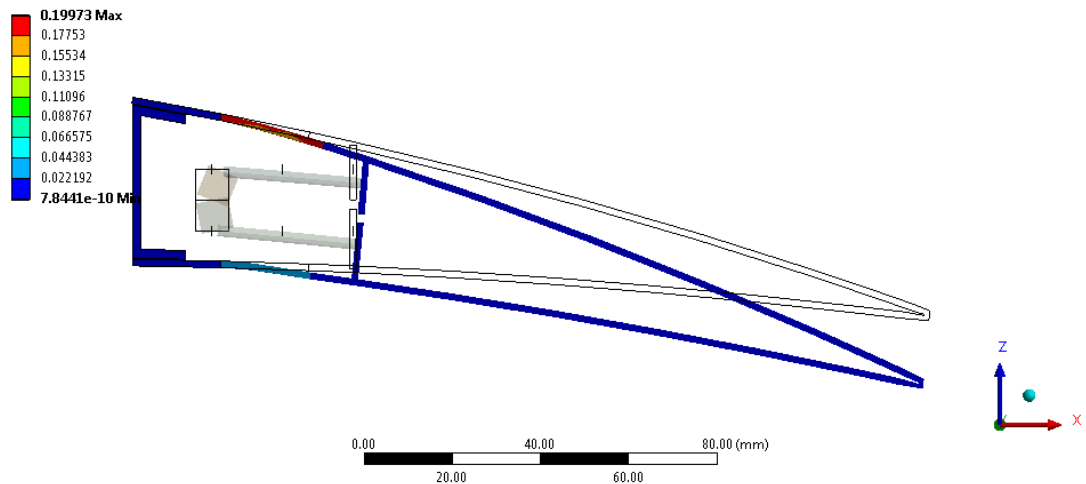


Figure 137: von-Mises Strain Distribution Contours for 15.2 [mm] Camber of Open Cell Design Under Aerodynamic Loading – Skin Thicknesses are 1.5 [mm] – Maximum 0.200 [mm/mm]

AE: 1.5mm - Composite - 2+2 - Open Cell - NACA9510  
Maximum Combined Stress  
Type: Maximum Combined Stress - Top/Bottom - Layer 0  
Unit: MPa  
Time: 1  
10.02.2015 15:29

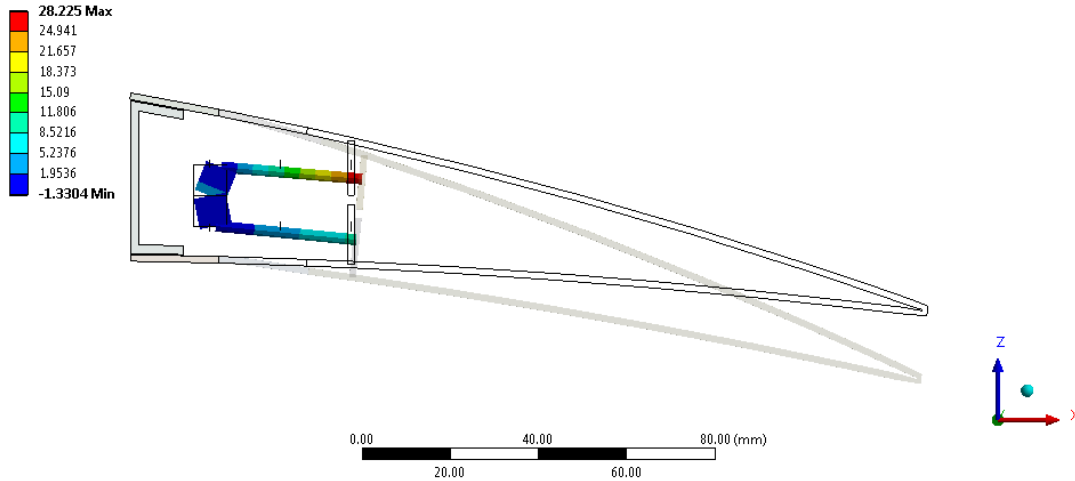


Figure 138: The Combined Beam Stresses for 15.2 [mm] Camber of Open Cell Design Under Aerodynamic Loading – Skin Thicknesses are 1.5 [mm] – Maximum 28.225 [MPa]

The resulting reaction moments at moment arms are 50 [N-mm] for servo to actuate the upper portion of the transmission part, -26 [N-mm] for servo to actuate the lower portion of the transmission part. These values are below the maximum torque limit of selected servo actuator.

In order to hold the control surface for 15.2 [mm] decamber, rotation boundary conditions were applied as in in-vacuo cases. Therefore, 14 [deg] rotation about y axis was prescribed for moment arms of servo actuators to drive the upper portion of transmission parts, and -28.5 [deg] rotation about y axis was prescribed for moment arms of servo actuators to drive the lower portion of transmission parts as boundary conditions.

Transverse displacement contours are shown in Figure 139. von-Mises strain distribution contours are shown in Figure 140. The combined beam stresses are shown in Figure 141. As it can be concluded from Figure 139 that capping is eliminated by increasing the skin thickness.

Y: 1.5mm - Composite - 2+2 - Open Cell - NACA3510  
 Directional Deformation  
 Type: Directional Deformation(Z Axis)  
 Unit: mm  
 Global Coordinate System  
 Time: 1  
 10.02.2015 15:29

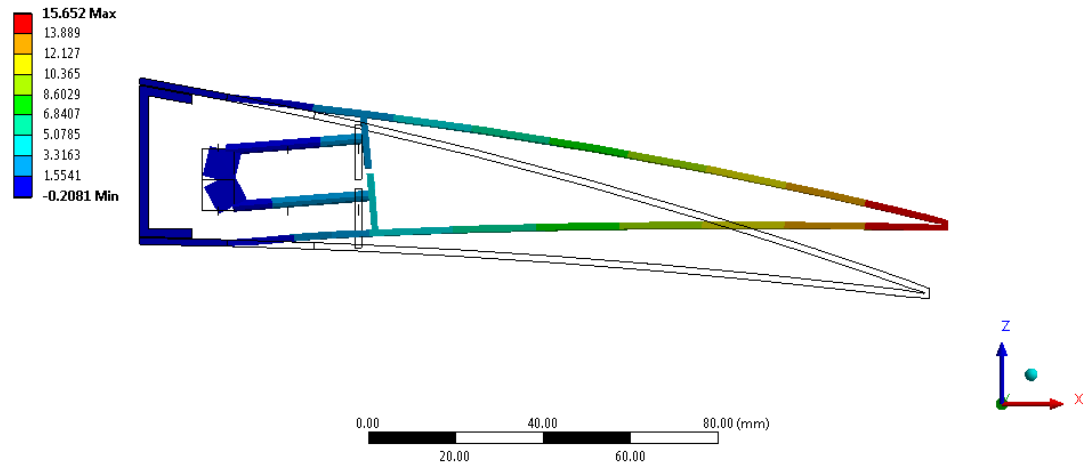


Figure 139: Transverse Displacement Contours for 15.2 [mm] Decamber of Open Cell Design Under Aerodynamic Loading – Skin Thicknesses are 1.5 [mm] – Maximum 15.652 [mm]

Y: 1.5mm - Composite - 2+2 - Open Cell - NACA3510  
 Equivalent Elastic Strain 2  
 Type: Equivalent Elastic Strain - Top/Bottom - Layer 0  
 Unit: mm/mm  
 Time: 1  
 10.02.2015 15:30

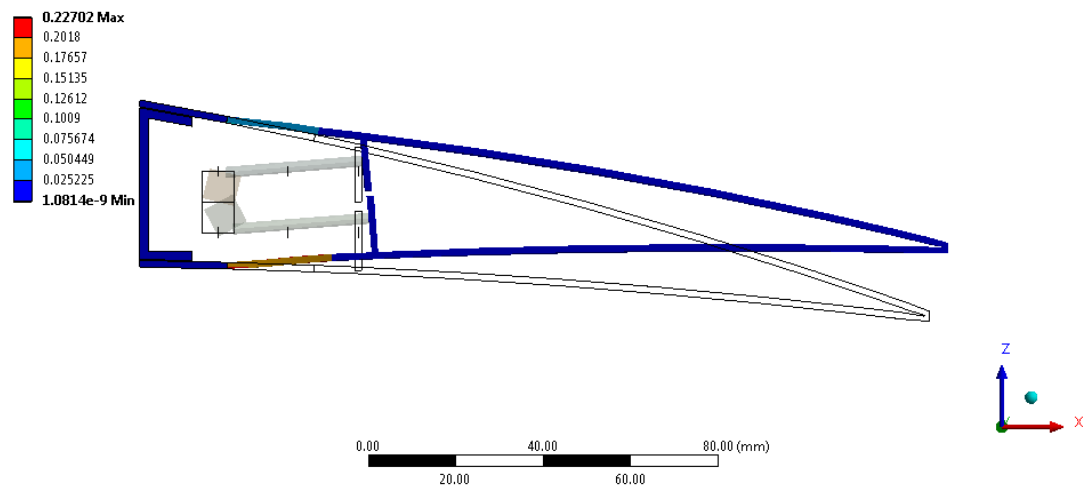


Figure 140: von-Mises Strain Distribution Contours for 15.2 [mm] Decamber of Open Cell Design Under Aerodynamic Loading – Skin Thicknesses are 1.5 [mm] – Maximum 0.227 [mm/mm]

Y: 1.5mm - Composite - 2+2 - Open Cell - NACA3510  
Maximum Combined Stress  
Type: Maximum Combined Stress - Top/Bottom - Layer 0  
Unit: MPa  
Time: 1  
10.02.2015 15:30

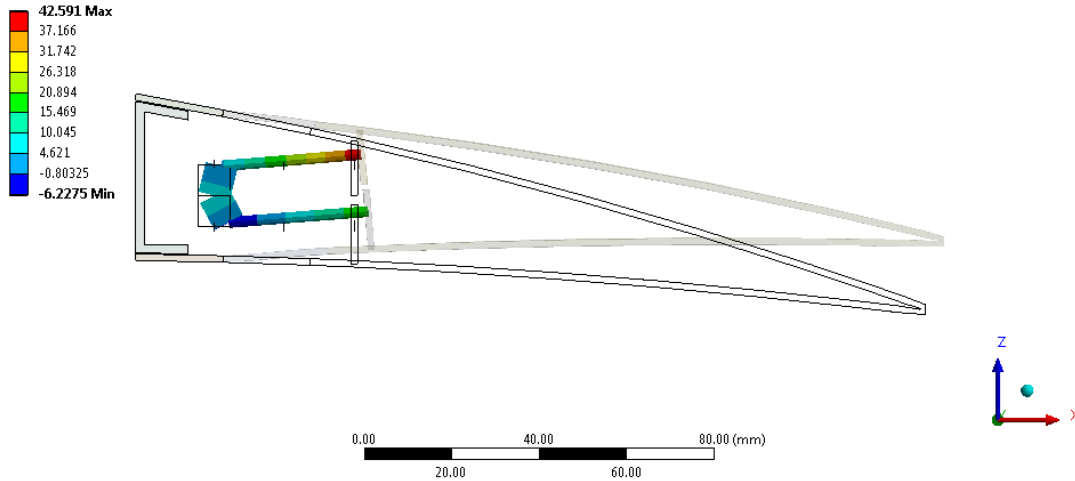


Figure 141: The Combined Beam Stresses for 15.2 [mm] Decamber of Open Cell Design Under Aerodynamic Loading – Skin Thicknesses are 1.5 [mm] – Maximum 42.591 [MPa]

The resulting reaction moments at moment arms are -120 [N-mm] for servo to actuate the upper portion of the transmission part, -195 [N-mm] for servo to actuate the lower portion of the transmission part. These values are below the maximum torque limit of selected servo actuator.

In order to hold the control surface for 20.2 [mm] decamber, rotation boundary conditions were applied as in in-vacuo cases. Therefore, 20 [deg] rotation about y axis was prescribed for moment arms of servo actuators to drive the upper portion of transmission parts, and -34.5 [deg] rotation about y axis was prescribed for moment arms of servo actuators to drive the lower portion of transmission parts as boundary conditions.

Transverse displacement contours are shown in Figure 142. von-Mises strain distribution contours are shown in Figure 143. The combined beam stresses are shown in Figure 144.



**Directional Deformation**  
 Type: Directional Deformation(Z Axis)  
 Unit: mm  
 Global Coordinate System  
 Time: 1  
 10.02.2015 15:31

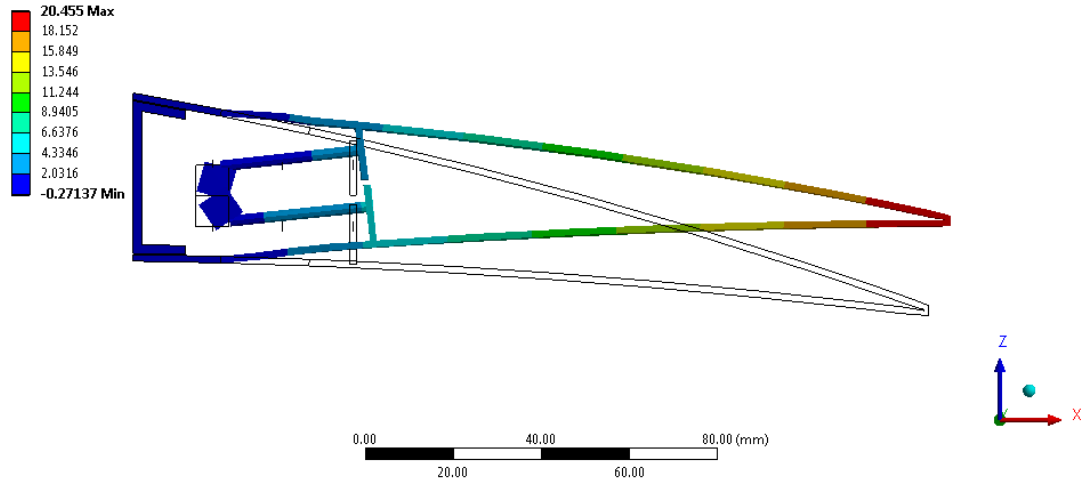


Figure 142: Transverse Displacement Contours for 20.2 [mm] Decamber of Open Cell Design Under Aerodynamic Loading – Skin Thicknesses are 1.5 [mm] – Maximum 20.455 [mm]

**Equivalent Elastic Strain 2**  
 Type: Equivalent Elastic Strain - Top/Bottom - Layer 0  
 Unit: mm/mm  
 Time: 1  
 10.02.2015 15:31

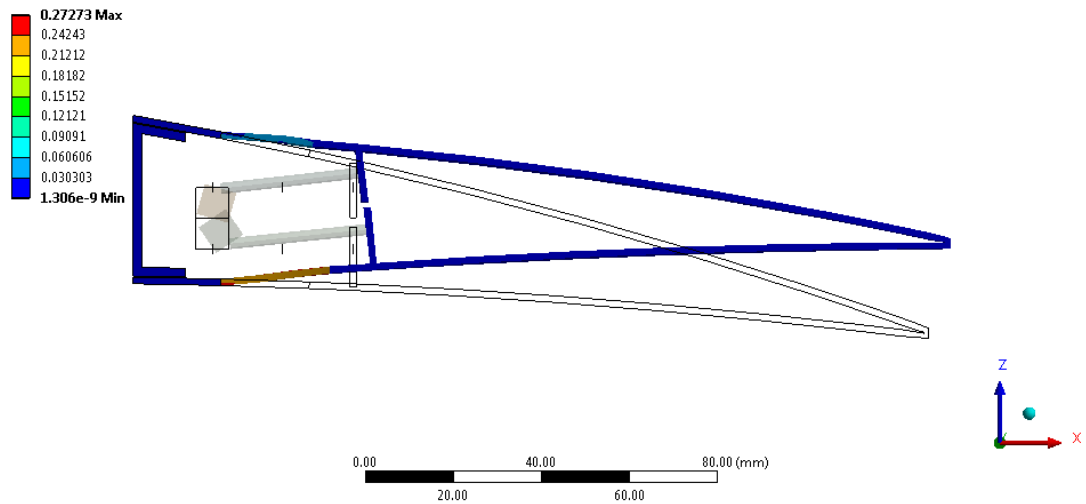


Figure 143: von-Mises Strain Distribution Contours for 20.2 [mm] Decamber of Open Cell Design Under Aerodynamic Loading – Skin Thicknesses are 1.5 [mm] – Maximum 0.273 [mm/mm]

**Maximum Combined Stress**  
 Type: Maximum Combined Stress - Top/Bottom - Layer 0  
 Unit: MPa  
 Time: 1  
 10.02.2015 15:31

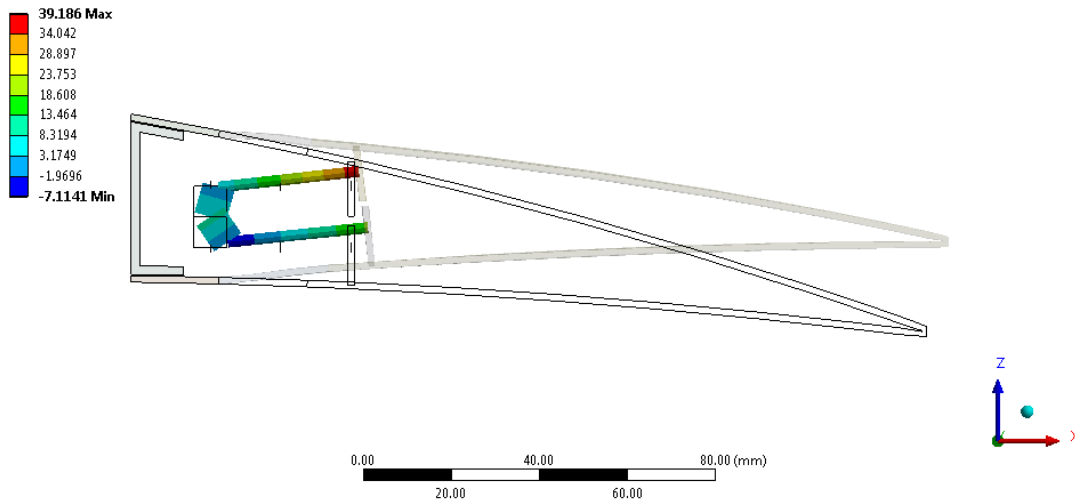


Figure 144: The Combined Beam Stresses for 20.2 [mm] Decamber of Open Cell Design Under Aerodynamic Loading – Skin Thicknesses are 1.5 [mm] – Maximum 39.186 [MPa]

The resulting reaction moments at moment arms are -132 [N-mm] for servo to actuate the upper portion of the transmission part, -212 [N-mm] for servo to actuate the lower portion of the transmission part. These values are below the maximum torque limit of selected servo actuator.

## 5.4 Finite Element Analysis of Closed Cell Design Under Aerodynamic Loading

### 5.4.1 Finite Element Modelling of Closed Cell Design

Finite Element Model of closed cell design is same as explained in Chapter 4. As in open cell case, additional boundary condition was due to the applied aerodynamic pressure to the skin parts. Applied boundary conditions are depicted in Figure 145.

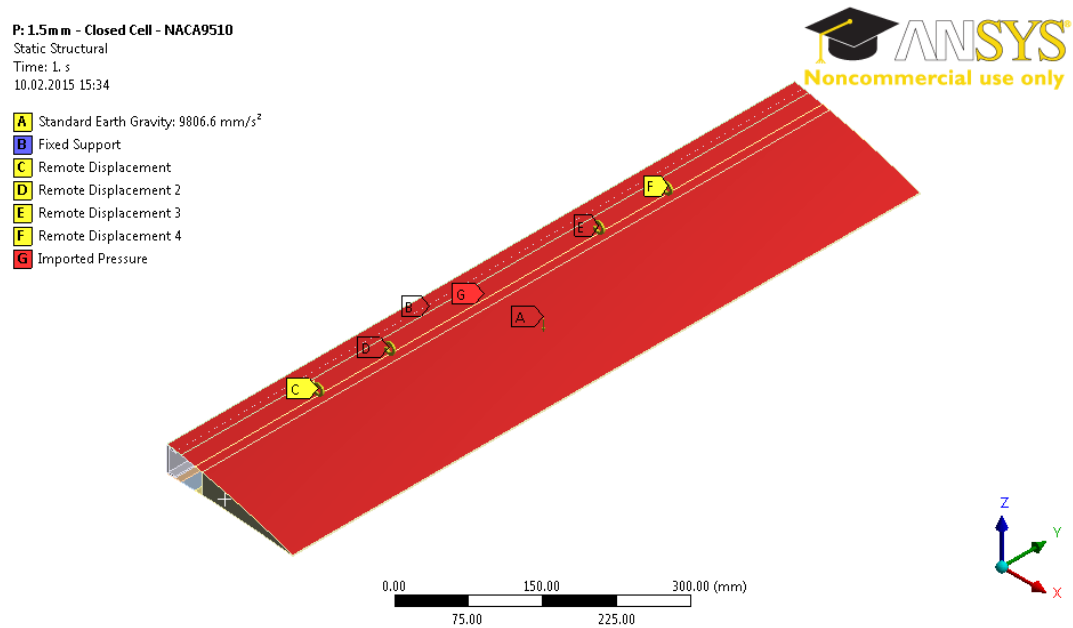


Figure 145: Applied Boundary Conditions to Closed Cell Design under Aerodynamic Loading

#### 5.4.2 Analysis of Camber and Decamber Variations of Closed Cell Design

It is shown in previous section that 1 [mm] skin thickness results in capping of the compliant skin. Therefore, analyses of camber and decamber variations of closed cell design under aerodynamic loading were conducted for 1.5 [mm] skin thickness case to eliminate capping as well.

In order to hold the control surface for 15.2 [mm] camber, rotation boundary conditions were applied as in in-vacuo cases. Therefore, 23 [deg] rotation about y axis was prescribed for moment arms of servo actuators to drive the upper portion of transmission parts, and -12 [deg] rotation about y axis was prescribed for moment arms of servo actuators to drive the lower portion of transmission parts as boundary conditions.

Transverse displacement contours are shown in Figure 146. von-Mises strain distribution contours are shown in Figure 147. The combined beam stresses are shown in Figure 148.

P: 1.5 mm - Closed Cell - NACA9510  
 Directional Deformation  
 Type: Directional Deformation(Z Axis)  
 Unit: mm  
 Global Coordinate System  
 Time: 1  
 10.02.2015 15:34

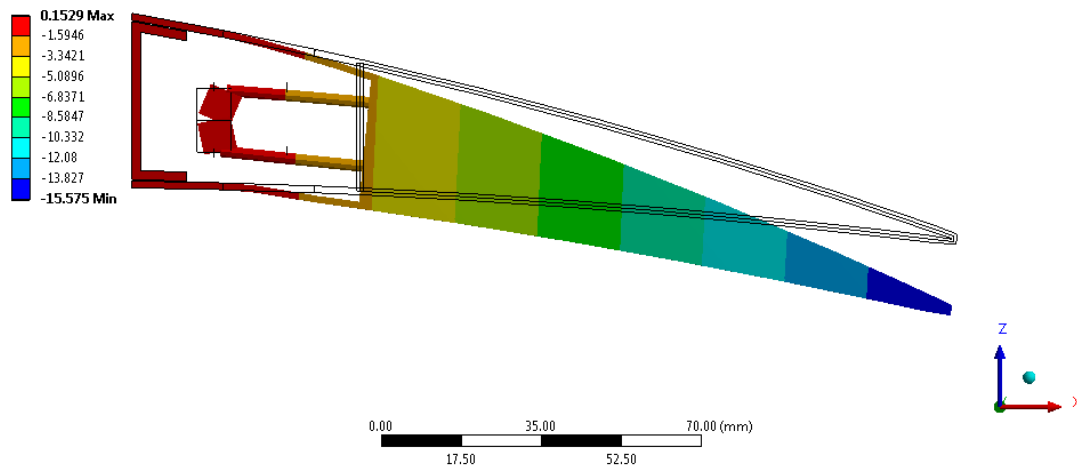


Figure 146: Transverse Displacement Contours for 15.2 [mm] Camber of Closed Cell Design Under Aerodynamic Loading – Maximum 15.575 [mm]

P: 1.5 mm - Closed Cell - NACA9510  
 Equivalent Elastic Strain 2  
 Type: Equivalent Elastic Strain - Top/Bottom - Layer 0  
 Unit: mm/mm  
 Time: 1  
 10.02.2015 15:35

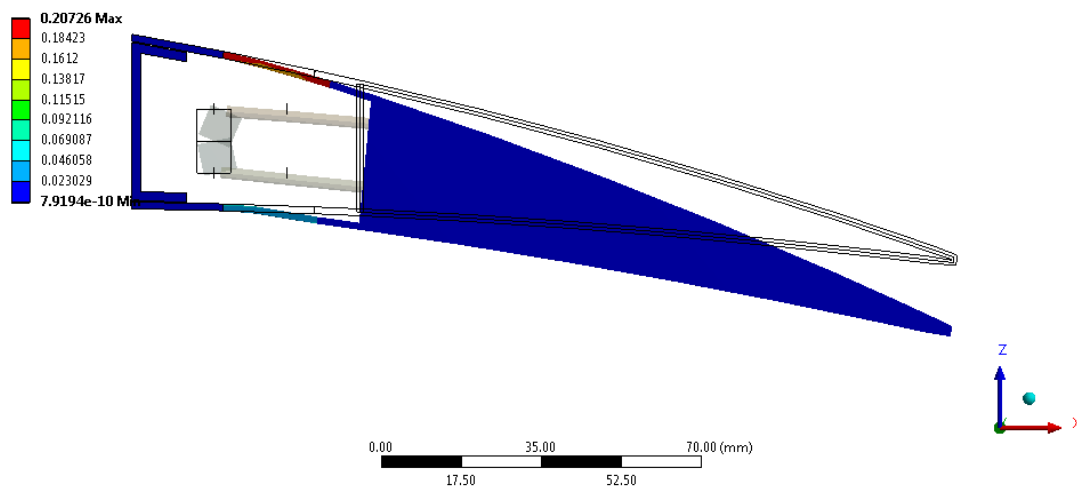


Figure 147: von-Mises Strain Distribution Contours for 15.2 [mm] Camber of Closed Cell Design Under Aerodynamic Loading – Maximum 0.207 [mm/mm]

P: 1.5mm - Closed Cell - NACA9510

Maximum Combined Stress

Type: Maximum Combined Stress - Top/Bottom - Layer 0

Unit: MPa

Time: 1

10.02.2015 15:35

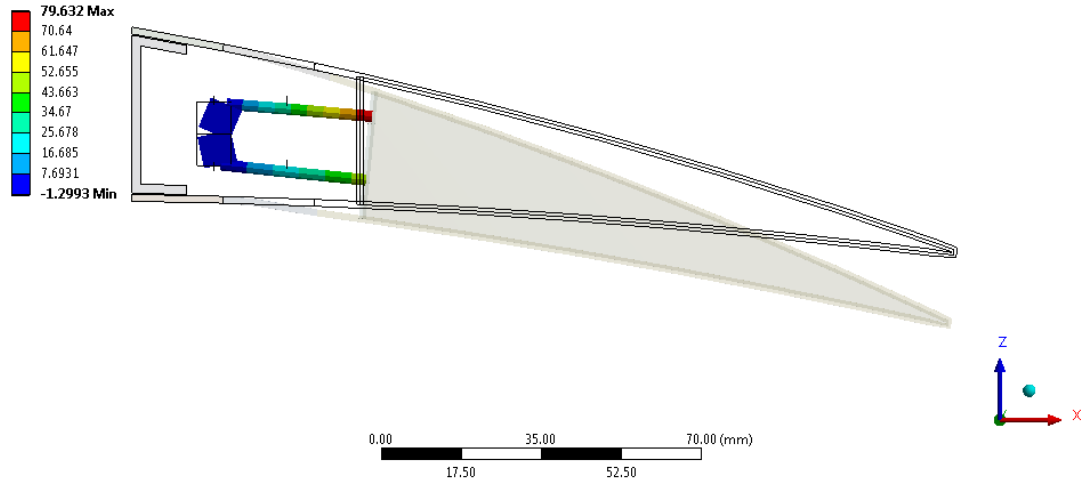


Figure 148: The Combined Beam Stresses for 15.2 [mm] Camber of Closed Cell Design Under Aerodynamic Loading – Maximum 79.632 [MPa]

The resulting reaction moments at moment arms are 44 [N-mm] for servo to actuate the upper portion of the transmission part, -49 [N-mm] for servo to actuate the lower portion of the transmission part. These values are below the maximum torque limit of selected servo actuator.

In order to hold the control surface for 15.2 [mm] decamber, rotation boundary conditions were applied as in in-vacuo cases. Therefore, 14 [deg] rotation about y axis was prescribed for moment arms of servo actuators to drive the upper portion of transmission parts, and -25 [deg] rotation about y axis was prescribed for moment arms of servo actuators to drive the lower portion of transmission parts as boundary conditions.

Transverse displacement contours are shown in Figure 149. von-Mises strain distribution contours are shown in Figure 150. The combined beam stresses are shown in Figure 151.

E: 1.5 mm - Closed Cell - NACA3510  
 Directional Deformation  
 Type: Directional Deformation(Z Axis)  
 Unit: mm  
 Global Coordinate System  
 Time: 1  
 10.02.2015 15:36

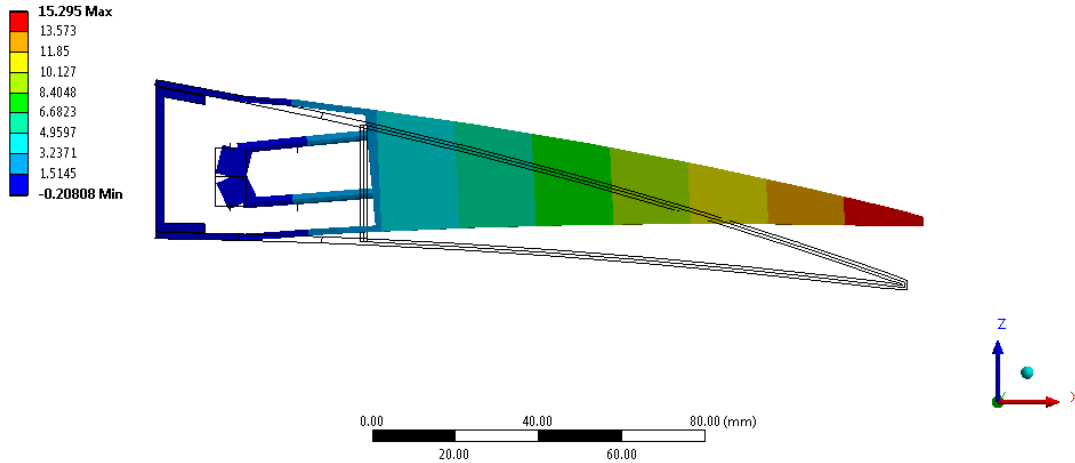


Figure 149: Transverse Displacement Contours for 15.2 [mm] Decamber of Closed Cell Design Under Aerodynamic Loading – Maximum 15.295 [mm]

E: 1.5 mm - Closed Cell - NACA3510  
 Equivalent Elastic Strain 2  
 Type: Equivalent Elastic Strain - Top/Bottom - Layer 0  
 Unit: mm/mm  
 Time: 1  
 10.02.2015 15:36

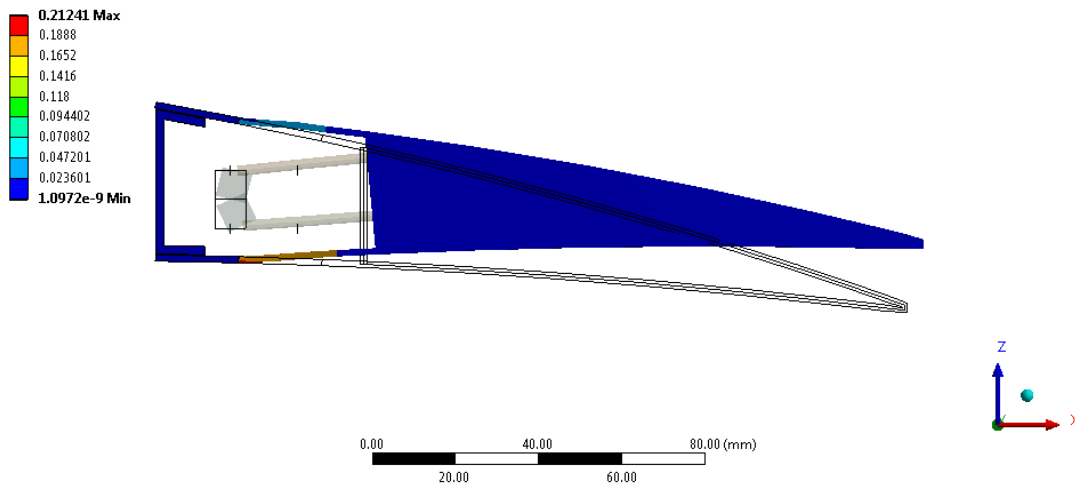


Figure 150: von-Mises Strain Distribution Contours for 15.2 [mm] Decamber of Closed Cell Design Under Aerodynamic Loading – Maximum 0.212 [mm/mm]

E: 1.5mm - Closed Cell - NACA3510

Maximum Combined Stress

Type: Maximum Combined Stress - Top/Bottom - Layer 0

Unit: MPa

Time: 1

10.02.2015 15:37

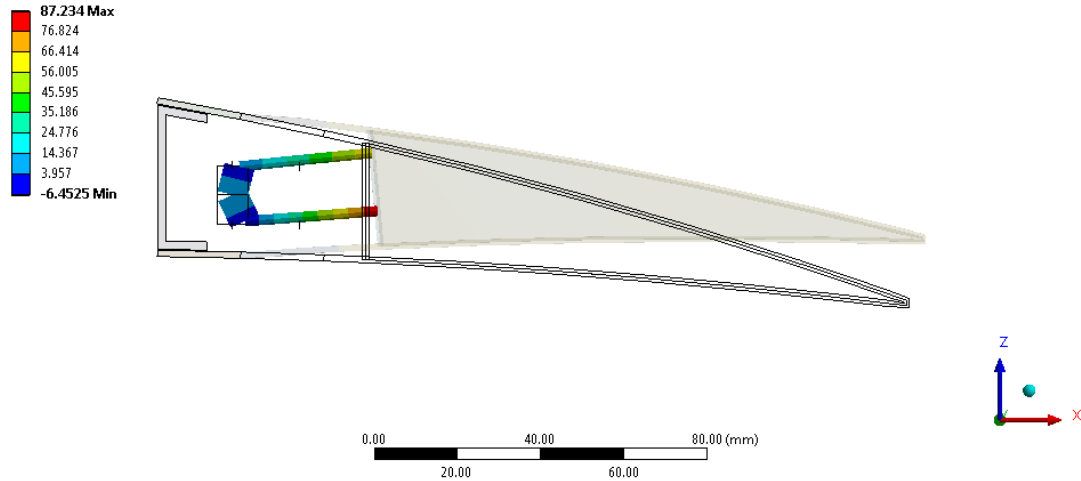


Figure 151: The Combined Beam Stresses for 15.2 [mm] Decamber of Closed Cell Design Under Aerodynamic Loading – Maximum 87.234 [MPa]

The resulting reaction moment at moment arms are -132 [N-mm] for servo to actuate the upper portion of the transmission part, -230 [N-mm] for servo to actuate the lower portion of the transmission part. These values are below the maximum torque limit of selected servo actuator.

In order to hold the control surface for 20.2 [mm] decamber, rotation boundary conditions were applied as in in-vacuo cases. Therefore, 20 [deg] rotation about y axis was prescribed for moment arms of servo actuators to drive the upper portion of transmission parts, and -34.5 [deg] rotation about y axis was prescribed for moment arms of servo actuators to drive the lower portion of transmission parts as boundary conditions.

Transverse displacement contours are shown in Figure 152. von-Mises strain distribution contours are shown in Figure 153. The combined beam stresses are shown in Figure 154.

L: 1.5mm - Closed Cell - NACA2510  
 Directional Deformation  
 Type: Directional Deformation(Z Axis)  
 Unit: mm  
 Global Coordinate System  
 Time: 1  
 10.02.2015 15:37

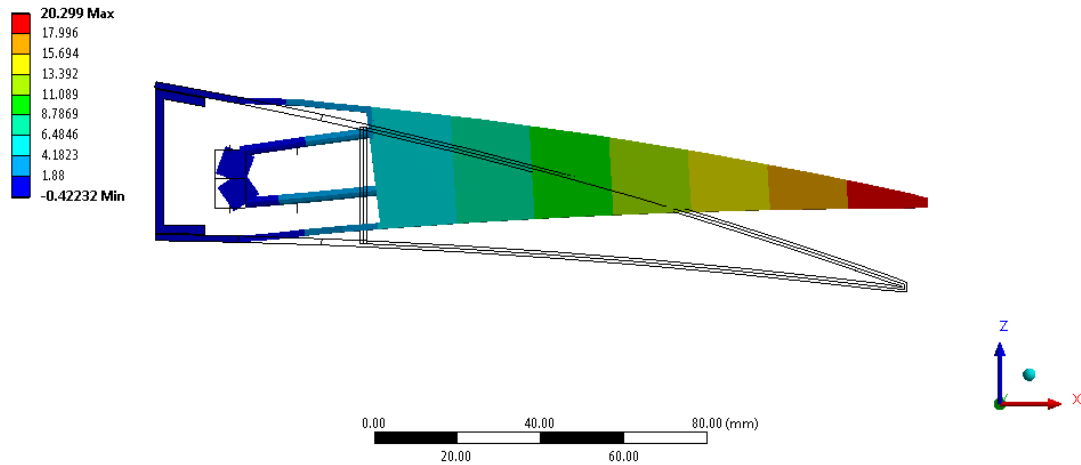


Figure 152: Transverse Displacement Contours for 20.2 [mm] Decamber of Closed Cell Design Under Aerodynamic Loading – Maximum 20.299 [mm]

L: 1.5mm - Closed Cell - NACA2510  
 Equivalent Elastic Strain 2  
 Type: Equivalent Elastic Strain - Top/Bottom - Layer 0  
 Unit: mm/mm  
 Time: 1  
 10.02.2015 15:37

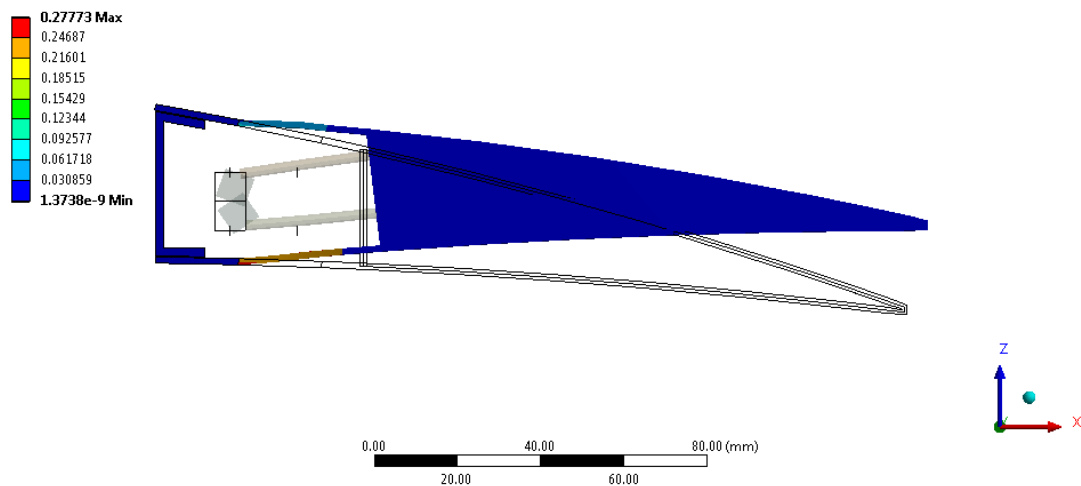


Figure 153: von-Mises Strain Distribution Contours for 20.2 [mm] Decamber of Closed Cell Design Under Aerodynamic Loading – Maximum 0.278 [mm/mm]



L: 1.5mm - Closed Cell - NACA2510

Maximum Combined Stress

Type: Maximum Combined Stress - Top/Bottom - Layer 0

Unit: MPa

Time: 1

10.02.2015 15:37

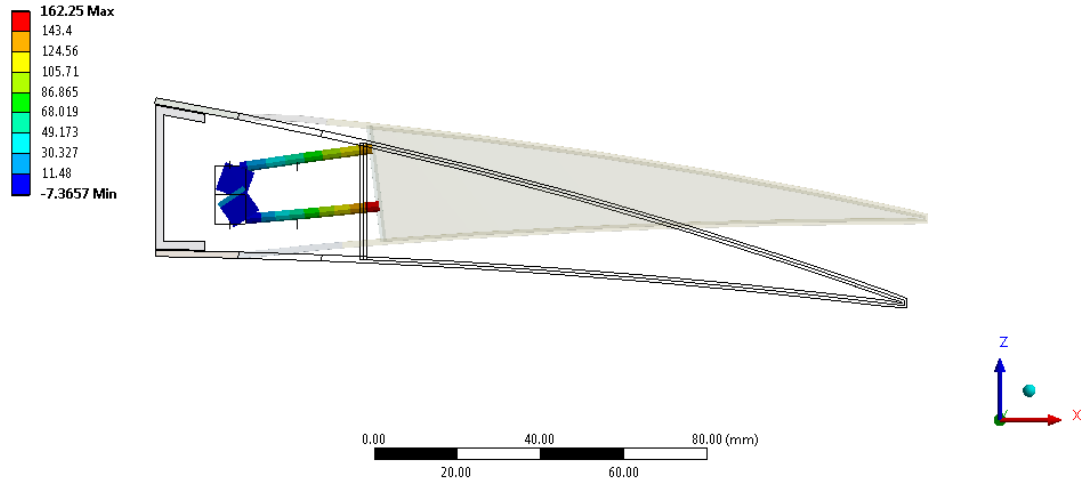


Figure 154: The Combined Beam Stresses for 20.2 [mm] Decamber of Closed Cell Design Under Aerodynamic Loading – Maximum 162.250 [MPa]

The resulting reaction moment at moments arms are -118 [N-mm] for servo to actuate the upper portion of the transmission part, -263 [N-mm] for servo to actuate the lower portion of the transmission part. These values are below the maximum torque limit of selected servo actuator.

## 5.5 Discussion and Conclusion

In this chapter, the structural analysis of the hybrid trailing edge control surface is conducted for open and closed cell design under aerodynamic loading.

Initial analysis of open cell design showed that although 1 [mm] skin thicknesses case works well in in-vacuo condition, it creates a capping problem at upper compliant skin under aerodynamic loading. Therefore, the skin thicknesses were increased to 1.5 [mm] and analysis were performed again. It was shown that the control surface was also capable of performing both camber and decamber under aerodynamic loading for open cell design.

The analyses of closed cell design were also conducted for 1.5 [mm] skin thickness case. The results showed that the control surface was also capable of performing both camber and decamber under aerodynamic loading for closed cell design.

It could be concluded from the results of the analysis that as skin thicknesses decreases, capping problem occurs in upper compliant skin. Therefore, increasing the skin thicknesses result in better performance of the hybrid trailing edge control surface under aerodynamic loading. However, increasing the skin thicknesses may result in much higher torque requirements. Therefore, it is a trade-off that must be carried out carefully.

The weight of the parts and the total weight of the analyzed design are presented in Table 18. The increase in skin thickness in order to eliminate the capping problem resulted in 0.341 [kg] weight increase in open cell design and 0.343 [kg] weight increase in closed cell design.

Table 18: Weight Comparison of Analyzed Designs under Aerodynamic Loading

	C Part [kg]	Compliant Part [kg]	Rigid Part [kg]	Servos and Equipment [kg]	Total Weight [kg]
Open Cell Design, Skin Thicknesses 1.5 [mm], Rigid Part is Composite	0.422	0.068	0.804	0.124	1.418
Open Cell Design, Skin Thicknesses 1.0 [mm], Rigid Part is Composite	0.372	0.045	0.536	0.124	1.077
Closed Cell Design, Skin Thicknesses 1.5 [mm], Rigid Part is Composite with Foam	0.422	0.068	0.902	0.124	1.516
Closed Cell Design, Skin Thicknesses 1.0 [mm], Rigid Part is Composite with Foam	0.372	0.045	0.632	0.124	1.173

The results of analyses are summarized in Table 19, Table 20, Table 21 and Table 22. These tables present the maximum von-Mises strains, maximum combined beam stresses and reaction moments of servo actuators in analyzed design configurations.

Table 19: Maximum von-Mises Strains in Analyzed Designs under Aerodynamic Loading

	15.2 [mm] Camber Case [mm/mm]	15.2 [mm] Decamber Case [mm/mm]	20.2 [mm] Decamber Case [mm/mm]
Open Cell Design, Skin Thicknesses 1.5 [mm], Rigid Part is Composite	0.200	0.227	0.273
Closed Cell Design, Skin Thicknesses 1.5 [mm], Rigid Part is Composite with Foam	0.207	0.212	0.278

Table 20: Maximum Combined Beam Stresses in Analyzed Designs under Aerodynamic Loading

	15.2 [mm] Camber Case [MPa]	15.2 [mm] Decamber Case [MPa]	20.2 [mm] Decamber Case [MPa]
Open Cell Design, Skin Thicknesses 1.5 [mm], Rigid Part is Composite	28.225	42.591	39.186
Closed Cell Design, Skin Thicknesses 1.5 [mm], Rigid Part is Composite with Foam	79.632	87.234	162.250

Table 21: Reaction Moments of Servo Actuators to Actuate the Lower Portion of the Transmission Parts in Analyzed Designs under Aerodynamic Loading

	15.2 [mm] Camber Case [N-mm]	15.2 [mm] Decamber Case [N-mm]	20.2 [mm] Decamber Case [N-mm]
Open Cell Design, Skin Thicknesses 1.5 [mm], Rigid Part is Composite	50.179	120.170	132.090
Closed Cell Design, Skin Thicknesses 1.5 [mm], Rigid Part is Composite with Foam	44.142	132.040	117.970

Table 22: Reaction Moments of Servo Actuators to Actuate the Upper Portion of the Transmission Parts in Analyzed Designs under Aerodynamic Loading

	15.2 [mm] Camber Case [N-mm]	15.2 [mm] Decamber Case [N-mm]	20.2 [mm] Decamber Case [N-mm]
Open Cell Design, Skin Thicknesses 1.5 [mm], Rigid Part is Composite	26.871	195.460	211.780
Closed Cell Design, Skin Thicknesses 1.5 [mm], Rigid Part is Composite with Foam	48.857	230.740	263.680



## CHAPTER 6

### CONCLUSION

#### 6.1 General Conclusions

In this thesis, the structural design and analysis of a hybrid trailing edge control surface were presented. The solid models of the structural design were created by CATIA V5-6R2012 package software. The structural analysis were performed by finite element method by using Static Structural module of ANSYS Workbench v14.0 package software.

Initially, the control surface was designed in in-vacuo condition by so-called "open cell design" and analyzed. It was shown that the design is capable of performing both camber and decamber morphing. Then, several trade-off studies including material, geometric and servo actuators variations were considered. The twist of the open cell design was also studied. After that, the design and the analysis of the control surface was conducted by so-called "closed cell design" again in in-vacuo condition and the characteristics of the control surface were assessed in terms of camber and decamber.

The control surface designs were also analyzed for the cases under the aerodynamic loading. It was shown that both designs are capable of performing both camber and decamber under aerodynamic loading as well.

The following general conclusions were drawn from the study:

- It was concluded that for intended camber increase, it is beneficial to use higher number of servo actuators for the actuation of the upper part of the control surface compared to the actuation of the lower part. Likewise, for intended camber decrease or decamber, it is beneficial to

use higher number of servo actuators for the actuation of the lower part of the control surface compared to the actuation of the upper part.

- It was concluded that as the skin thicknesses increase, the capping of the compliant part reduces.

## **6.2 Recommendations for Further Studies**

A formal optimization can be conducted to find the optimum location and number of servo actuators.

Different compliant materials, with different lengths and thicknesses, can be studied and behavior of the control surface under these conditions can be investigated.

In order to reduce the weight of the control surface, different types of composites can be used as the material of so-called "rigid part" of the control surface. Likewise, the connection part between the control surface and the wing, so-called "C part", can be redesigned with different materials to reduce the weight while still assuring that the part is sufficiently rigid.

The aerodynamic loadings can be calculated with higher load factors and then applied to the control surface. Therefore, the behavior of the control surface under higher load factors can be assessed.

Instead of placing servo actuators inside the control surface volume, the servo actuators can be located inside the torque box of the wing. Hence, a new design study can be conducted.

The control surface can be investigated for the case where control surface has a pre-twist along its span. The structural and aerodynamic characteristics of the wing can be assessed.

An aeroelastic study can be conducted by combining both structural and aerodynamic properties and a multi-disciplinary optimization of the control surface can also be conducted including the producibility factors.



## REFERENCES

- [1] Airbus S.A.S. Biomimicry. <http://www.airbus.com/innovation/eco-efficiency/design/biomimicry> [Last accessed on February 17, 2014]
- [2] V. Prisacariu, C. Cioaca, and M. Boşcoianu. The Concept of Morphing Adapted Structures to UAVS. Review of the Air Force Academy, 20(1):13, 2012
- [3] M. I. Friswell and D. J. Inman. Morphing Concepts for UAVs. In 21st International Unmanned Air Vehicle Systems Conference, Bristol, UK, 3-5 April 2006. paper 13
- [4] Merriam-Webster, 2012. <http://www.merriam-webster.com/dictionary/morphing> [Last accessed on February 17, 2014]
- [5] S. Özgen, Y. Yaman, M. Şahin, G. Seber, S. Körpe, E. Sakarya, L. Ünlüsoy, T. İnsuyu, G. Bayram, Y. Uludağ and A. Yılmaz. Morphing Air Vehicle Concepts. In UVW2010, International Unmanned Vehicle Workshop, Turkish Air Force Academy, Istanbul, Turkey, Paper ID: 5, 10-12 June 2010.
- [6] R. Ajaj, A. Keane, C. Beaverstock, M. Friswell, and D. Inman. Morphing Aircraft: The Need for a New Design Philosophy. In 7. Ankara International Aerospace Conference, METU, Ankara, Turkey, 11-13 September 2013. paper AIAC-2013-054
- [7] N. Gandhi, D. Ward, A. Jha, J. Monaco, T. Seigler, and D. Inman. Intelligent Control of a Morphing Aircraft. In Collection of Technical Papers - AIAA/ASME/ASCE/AHS/ASC Structures, Structural Dynamics and Materials Conference, volume 1, pages 166-182, 2007
- [8] T. M. Seigler. Dynamics and Control of Morphing Aircraft. PhD thesis, Virginia Polytechnic Institute and State University, Blacksburg, Virginia, 2 August 2005

- [9] T. A. Weisshaar. Morphing Aircraft Technology - New Shapes for Aircraft Design. In Multifunctional Structures / Integration of Sensors and Antennas, Neuilly-sur-Seine, France, 2006. Meeting Proceedings RTO-MPAVT-141
- [10] A. Bolonkin and G. B. Gilyard. Estimated Benefits of Variable-Geometry Wing Camber Control for Transport Aircraft. National Aeronautics and Space Administration, Dryden Flight Research Center, 1999
- [11] M. Kintscher, M. Wiedemann, H. Monner, O. Heintze, and T. Kühn. Design of a Smart Leading Edge Device for Low Speed Wind Tunnel Tests in the European Project SADE. *International Journal of Structural Integrity*, 2(4):383-405, 2011
- [12] M. D. Skillen and W. A. Crossley. Modeling and Optimization for Morphing Wing Concept Generation. NASA/CR-2007-214860, 2007
- [13] P. Gamboa, J. Vale, F. Lau, and A. Suleman. Optimization of a Morphing Wing Based on Coupled Aerodynamic and Structural Constraints. *AIAA Journal*, 47(9):2087-2104, 2009
- [14] S. Bagassi, D. Francia, and F. Persiani. Preliminary Study of a New UAV Concept: The Variable Geometry Vehicle. ICAS2010, 27th International Congress of the Aeronautical Sciences, Nice, France, 2010.
- [15] T. L. Grigorie, A. V. Popov, R. M. Botez, M. Mamou, and Y. Mebarki. On-off and Proportional-Integral Controller for a Morphing Wing. Part 1: Actuation Mechanism and Control Design. In *Proceedings of the Institution of Mechanical Engineers Part G – Journal of Aerospace Engineering*, February 2012, 226 G2, 131-145.
- [16] M. I. Friswell. The Prospects for Morphing Aircraft. *Smart Structures and Materials (SMART'09)*, IV ECCOMAS Thematic Conference, Porto, Portugal, 13-15 July 2009, 175-188.

- [17] T. A. Weisshaar. Morphing Aircraft Technology - New Shapes for Aircraft Design. In Multifunctional Structures / Integration of Sensors and Antennas, Neuilly-sur-Seine, France, 2006. Meeting Proceedings RTO-MPAVT-141
- [18] S. Barbarino, O. Bilgen, R. M. Ajaj, M. I. Friswell, and D. J. Inman. A Review of Morphing Aircraft. *Journal of Intelligent Material Systems and Structures*, 22(9):823-877, 2011
- [19] D. P. Raymer. *Aircraft Design: A Conceptual Approach*. AIAA Education Series, 4th Edition, 2006.
- [20] NOVEMOR Project, <http://www.novemor.eu> [Last accessed on December 5, 2014]
- [21] CHANGE FP7 Project, <http://change.tekever.com> [Last accessed on December 5, 2014]
- [22] R. Vos, Z. Gürdal, and M. Abdalla. A Novel Mechanism for Active Wing Warping. In *Proceedings of 49th AIAA/ASME/ASCE/AHS/ASC Structures, Structural Dynamics, and Materials Conference*, volume 7, pages 2008-1879, 2008
- [23] B. K. S. Woods, and M. I. Friswell. The Adaptive Aspect Ratio Morphing Wing: Design Concept and Low Fidelity Skin Optimization. In *Proceedings of the ASME 2014 Conference on Smart Materials, Adaptive Structures and Intelligent Systems, SMASIS2014*, Newport, Rhode Island, USA, September 8-10, 2014.
- [24] TUBITAK 107M103 Project. Aeroservoelastic Analysis of the Effects of Camber and Twist on Tactical Unmanned Aerial Vehicle Mission-Adaptive Wings, 2011, retrieved from [http://ae.metu.edu.tr/~yyaman/LabCapabilities/TUBITAK\\_107M103.pdf](http://ae.metu.edu.tr/~yyaman/LabCapabilities/TUBITAK_107M103.pdf) [Last accessed on December 5, 2014]

- [25] S. Ricci. Adaptive Camber Mechanism for Morphing Experiences at DIA DIA-PoliMI. In Advanced Course on Morphing Aircraft, Istituto Superior Tecnico, Lisboa, Portugal, 17-20 November 2008
- [26] G. Seber, E. Sakarya, E. T. İnsuyu, M. Şahin, S. Özgen, and Y. Yaman. Evaluation of a Camber Morphing Concept Based on Controlled Flexibility. IFASD2009, International Forum on Aeroelasticity and Structural Dynamics 2009, Seattle, Washington, USA, 21-25 June 2009
- [27] L. Ünlüsoy. Effects of Morphing on Aeroelastic Behavior of Unmanned Aerial Vehicle Wings. PhD thesis, Middle East Technical University, Ankara, 7 February 2014
- [28] D. S. Körpe. Aerodynamic Modelling and Optimization of Morphing Wings. PhD thesis, Middle East Technical University, Ankara, 9 September 2015
- [29] ANSYS Workbench v14.0, Material Library
- [30] Cambridge University Engineering Department, “Materials Data Book”, 2003, pp. 10, <http://www-mdp.eng.cam.ac.uk/web/library/enginfo/cueddatabooks/materials.pdf>, [Last accessed on February 24, 2014]
- [31] INVENT GmbH, <http://www.invent-gmbh.de/> [Last accessed on October 17, 2014]
- [32] Rohacell Rima Product Information, <http://www.rohacell.com/sites/dc/Downloadcenter/Evonik/Product/ROHACELL/product-information/ROHACELL%20RIMA%20Product%20Information.pdf> [Last accessed on October 17, 2014]
- [33] Volz Servos, <http://www.volz-servos.com/English/13mmClass/> [Last accessed on December 5, 2014]

[34] ANSYS Workbench v14.0, Help Documentation

[35] P. Arslan, U. Kalkan, H. Tıraş, İ. O. Tunçöz, Y. Yang, E. Gürses, M. Şahin, S. Özgen, Y. Yaman. Structural Analysis of an Unconventional Hybrid Control Surface of a Morphing Wing. ICAST2014: 25th International Conference on Adaptive Structures and Technologies, The Hauge, Netherlands, 06-08 October 2014.